Modes collectifs et hydrodynamique dans la croûte interne des étoiles à neutrons

Noël Martin

To cite this version:

Noël Martin. Modes collectifs et hydrodynamique dans la croûte interne des étoiles à neutrons. Astrophysique stellaire et solaire [astro-ph.SR]. Université Paris Saclay (COmUE), 2016. Français. NNT : 2016SACLS251 . tel-01377304

HAL Id: tel-01377304
https://tel.archives-ouvertes.fr/tel-01377304
Submitted on 6 Oct 2016

NNT : 2016 SACLS 251

THÈSE DE DOCTORAT
DE
L'UNIVERSITÉ PARIS-SACLAY
PRÉPARÉE À
L'INSTITUT DE PHYSIQUE NUCLÉAIRE

ÉCOLE DOCTORALE N° 579

Particules hadrons énergie et noyau : instrumentation, image, cosmos et simulation.

Spécialité : Astrophysique nucléaire et nucleosynthèse.

par

M. Martin Noël

Modes collectifs et hydrodynamique dans la croûte interne des étoiles à neutrons

Thèse présentée et soutenue à Orsay, le 9 septembre 2016.

Composition du Jury :

M. Khan Elias	Professeur, Université Paris-Saclay, IPN, *Orsay*	Président
M. Baldo Marcello	Professeur, INFN, *Catania, Italy*	Rapporteur
M. Sedrakian Armen	Professeur, J.W. Goethe University, *Frankfurt am Main, Germany*	Rapporteur
Mme. Fantina Anthea	Chargée de Recherche, GANIL, *Caen*	Examinatrice
M. Urban Michael	Chargé de Recherche, IPN, *Orsay*	Directeur de thèse

Remerciements

Voilà trois ans qui se terminent. Trois belles années que j'ai partagées avec nombre d'entre vous et qui auraient été bien plus fades sinon. C'est aussi trois ans qui marquent la fin de mes études, et le début de la *vie active* ; puisque jusque là, en fait, je n'ai rien fait. Alors, vous trouverez dans ces pages qui suivent en Français, tous les “mercis” que je vous dois.

Je voudrais commencer par remercier mon jury, Marcello Baldo, Anthea Fantina, Élias Khan et Armen Sedrakian. Je vous remercie pour votre présence lors de ma soutenance, ainsi que pour la lecture et les commentaires positifs de mon travail. Ce fut un plaisir de vous lire, mais aussi de vous accueillir à l'Institut de Physique Nucléaire.

Bien évidemment, un énorme merci à Michael, mon directeur de thèse. Tu as été formidable, jamais je ne me suis senti seul ou démuni face à ce long travail. C'était un plaisir de travailler avec toi pendant ces trois ans, et j'espère aussi qu'on aura bien d'autres occasions de se revoir ! J'espère ainsi que notre habitude de fêter les articles acceptés par un repas au restaurant aura l'occasion de se perpétuer. Plus personnellement, c'était très agréable de pouvoir partager tous les deux nos passions communes, des trains aux postes de radio (qu'il faut réparer d'ailleurs). Je te souhaite le meilleur pour les années à venir et j'espère que tu pourras donner à d'autres étudiants la chance de t'avoir comme directeur.

Je dois mon parcours dans la recherche à Dany, physicien et marathonien Lyonnais. Tu m'as fait découvrir le monde de la recherche à un moment où j'hésitais encore. Merci de m'avoir fait confiance toutes ces années, puis de m'avoir guidé jusqu'ici. J'imagine que si tu n'avais pas été là, je n'écrirais sans doute pas ces remerciements. À bientôt dans la belle ville de Lyon !

Un grand merci à mon super groupe de Physique Théorique ! Merci pour votre accueil et tous ces moments que nous avons passés ensemble depuis mars 2013. Quelques phrases pour le trio que nous formions Cédric, Paolo et moi dès le début. Nous avons eu l'occasion de partager tous les trois fous rires et séances de cinéma culturel sur des sujets aussi graves que la soupe et les extraterrestres. Vous avez été tous les deux des repères rassurants alors que j'arrivais déboussolé de Lyon. Merci Denis pour ton humour piquant qui me fait toujours autant rire, et aussi pour toutes ces discussions à propos du mystère non élucidé du "voleur de sucre". Un merci à Élias, car c'est grâce à toi que dès le premier jour à l'IPN j'ai rencontré la bande d'étudiants en thèse (je reviendrai sur tout ça un peu plus loin). Tu m'auras beaucoup aidé dans nombre de mes formalités parfois pénibles. Un mot pour Marcella, merci pour tes réponses à mes questions quand Michael n'était pas là. Tu as été une oreille bienveillante dans certains moments difficiles. Merci Paolo pour tout, nos expérimentations "caféïques", nos dessins, et discussions sur des sujets très variés : de la spinodale, en passant par la myopie, jusqu'aux *hypsters*. Bonne route à vous tous et j'espère pouvoir vous rendre visite régulièrement dans les années à venir.

À l'étage d'en dessous, j'ai découvert très tôt une *terra incognita*, qui est finalement devenue un groupe *d'adoption* NESTER. Je vous ai tous rencontré rapidement, et c'était si agréable que je venais manger avec vous un jour sur deux (précisément, sinon j'avais des remarques côté théorie). Merci aux étudiants de m'avoir accueilli à bras ouvert dès mon premier jour à l'IPN. Il en reste aujourd'hui des amitiés sincères. Mais aussi merci aux permanents du groupe pour nos discussions animées autour du café. Je vous remercie pour vos petits mots d'encouragement et votre présence lors de la soutenance. Un message en particulier aux aventuriers quotidiens du RER : David, Fadi, Fairouz et Marlène, avec qui j'ai partagé embuches, co-voiturages et rigolades entre Paris et Orsay.

Voilà le tour des meilleurs, les thésards de l'IPN ! Je commencerai par un mot pour ceux qui ont quitté le labo pour d'autres aventures. Merci Pierre pour cette année et demie que nous avons passée ensemble. Nous nous sommes croisés dès mon premier jour, puis assez souvent par la suite, et même lors d'un moment inoubliable ce week-end de février au bord de la Manche dans ta Bretagne natale. Merci à Aurélie et Benjamin, pour les deux ans que nous avons partagées. Un mot pour mes collègues de promo, Marie-Co et Maud, foncez, c'est la dernière ligne droite avant la thèse, tout va bien se passer pour vous deux. Je vous souhaite pour les années à venir une expérience fantastique sur les routes du monde. Je suis impressionné par ce projet que vous avez construit. J'espère que j'aurai la chance de suivre votre périple, vous m'enverrez des cartes postales, hein ? En tous cas, c'était super de vous rencontrer toutes les deux. Nous aurons quelques souvenirs comme D2I2, qu'on aura géré main dans la main avec Marie-Co. Et plein d'autres bons moments comme cette soupe de potimarron au Chalet, un soir d'hiver, ou des barbecues l'été. Venons en maintenant aux deux qui nous suivent (Marie-Co, Maud et moi) et qui rentrent en troisième année[1] : Louis et Claire. Profitez de cette dernière année comme il se doit dans le meilleur bureau de tout le labo pendant la canicule. Merci pour toutes ces discussions que nous avons eu entre le site web, Perspectives, et la vie politique. Je serai ravi de venir à votre soutenance dans un peu moins d'un an maintenant... Aux derniers arrivés, Anastasia, Clément, Florent, Jana, Petar, et Raphaël, c'était super de faire le chemin de la troisième année avec vous. Je garderai d'excellents souvenirs comme : les gimmicks récurrents de *Kaamelott* avec Florent et Raphaël ; les débats avec Anastasia, Jana et Petar au sujet du dernier épisode de *How I Met Your Mother* ; mais aussi la ressemblance fortuite de Petar et *Swarley* ; et bien sûr les barbecues avec Raoul et ses cafés inimitables ! Faites bonne route dans ce début de deuxième année, profitez-en, il me semble que c'était la meilleure. Pour finir, bienvenue à Anne qui commence tout juste.

Un mot pour un ami essentiel qui n'est passé que trop vite à l'IPN, je parle de toi Guillaume H. Tu es parti t'exiler à l'autre bout de l'Essonne, mais ne t'en fais pas, je crois que l'an prochain je passerai souvent te voir dans ton bureau. En tous cas nos discussions viticoles, tes conseils MPI et notre respect inconditionnel de Brita me manquent. Venez vite nous voir à Paris, ça sera un plaisir de vous accueillir tous les trois.

Un merci aussi à tout ceux qui m'ont aidé à faire tourner tous ces codes. En effet, même si la théorie s'écrit avec le bout d'un crayon, la mise en pratique est plus dure. Merci à Laure-Amélie pour son aide et ses backups nécessaires. Merci à Christophe qui aura su me conseiller pour mes calculs les plus lourds. Pour finir un merci reconnaissant à Rachid, pour ton aide précieuse et tes conseils sur la grille de Lyon.

Je les ai dilués dans les remerciements : les tracas du quotidien... Mis à part leur côté terriblement pénible, ils ont eu le mérite de favoriser le lien social. Vous avez été un point de convergence pour beaucoup d'entre nous. Ainsi souvenons nous, des fenêtres ouvertes et la pluie dans le bureau, du mystère du "voleur de sucre", des capsules Brita, du frigo malodorant, de l'incendie du four à micro-ondes, du RER et du CESFO. Ah, qu'est ce que vous nous avez fait râler !

Maintenant viennent les remerciement les plus importants à la famille et aux amis. Merci à vous mes amis de Paris : Mathieu et Guillaume L., on ne se voit pas assez souvent, il va falloir que l'on s'appelle plus régulièrement par erreur. Je vous souhaite Pauline et Félix un beau voyage vers la patrie de la feuille d'érable, après tous nos souvenirs entre Paris et la Normandie. Un grand merci aussi aux amis Lyonnais restés proches : Alexandre, Bruno,

---

[1] Je ne dis pas ça pour vous mettre la pression, ça serait mal me connaître.

Camille, Élodie, Merry, Morgane et Myriam (tu es Lyonnaise, maintenant, c'est indéniable). Même si les distances rendent plus dures nos rencontres, nous ne nous sommes jamais perdus de vue. Quant aux deux qui préparent une thèse, bonne chance ! Parlons de toi Merry, ami Ardéchois, pourvu que nos métiers ne nous éloigneront pas trop et que l'Ardèche restera le centre de notre monde. Merci aussi à ceux que je n'ai pas cité mais qui m'auront ouvert leurs portes et rassuré par leur bienveillance. Un remerciement essentiel pour toi Sophie, ma Bretonne. Merci pour tout ce que tu as fait pour moi, merci pour ton soutien dans certaines passes difficiles, mais aussi dans les moments les plus heureux. Tu ne m'as jamais laissé tombé, y compris lors de la soutenance où tu as géré l'organisation comme une cheffe. En tous cas cette thèse aurait été bien différente sans toi, sans doute moins heureuse. Puis un morceau pour ma famille aimante qui m'entoure. Merci Papa pour ton soutien, merci de m'avoir accompagné dans ce parcours universitaire et dans la vie en général. J'étais ému de pouvoir partager ce jour inoubliable avec toi. Merci Maman d'avoir cru en moi et de m'avoir donné la possibilité de partir à Lyon. J'aurais tant aimé te remercier pour tous les efforts que tu as fait, mais la vie en aura décidé autrement. Merci Titi, d'être là depuis vingt ans maintenant, mais aussi pour ta bonne humeur et nos discussions fleuves sur tout un tas de sujets. Merci à Agnès et Maria d'avoir traversé la France pour passer cette journée avec moi, je ne l'oublierai pas ! Merci à mes grands-parents, pour tous ces moments partagés. Un mot particulier pour Marcel et Renée, vous n'avez pas pu venir, mais j'étais très touché par notre appel le lendemain de ma thèse, merci. Je reviendrai vous voir très vite pour partager la traditionnelle omelette du samedi soir. Et bien évidemment merci à tout le reste de la famille que je n'ai pas cité, mais qui se reconnaîtra, oncles et tantes, cousins et cousines, la liste est si grande et c'est une chance ! Vous avez été géniaux et toujours présents, jusqu'au jour J avec tous vos messages de soutien, encore merci ! Un mot d'encouragement pour mes cousins et cousines qui s'approchent d'année en année de leurs rêves en gravissant leurs années d'études. Bon courage, même si le parcours est parfois un peu long et qu'on aimerait bien griller les étapes. Finalement, vous en garderez, j'en suis sûr, une belle expérience, et pleins d'excellents souvenirs que j'espère encore meilleurs que les miens. Bonne chance, travaillez bien, et faîtes la fête aussi !

Voilà, c'est ainsi que se termine ce long chemin des études, maintenant beaucoup reste encore à faire. J'espère faire ce nouveau voyage avec vous, alors si le cœur vous en dit, sautons dans ce train avant qu'il ne parte vers d'autres aventures !

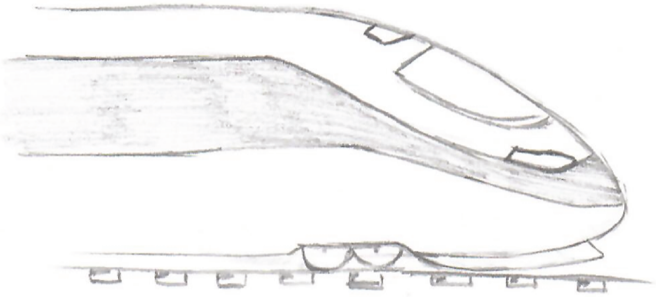

Contents

Motivation

Neutron stars have been extensively studied since Baade and Zwicky in 1934 proposed their existence [Baade and Zwicky, 1934]. Their description is at the interface of numerous domains of physics, e.g., X-ray astrophysics [Giacconi et al., 1962], pulsar signal observation [Hewish et al., 1968, ATNF, 2016], gravitational waves [Riles, 2013], solid state physics [Oyamatsu et al., 1984, Chamel, 2013], general relativity [Oppenheimer and Volkoff, 1939, Tolman, 1939] and nuclear physics [Glendenning, 1982, Ravenhall et al., 1983, Douchin and Haensel, 2000, Avancini et al., 2008].

In the present thesis we will concentrate on the nuclear physics description especially of the inner crust. Actually, neutron stars can be divided in three majors layers: the *outer crust*, the *inner crust* and the *core* [Chamel and Haensel, 2008]. The outer crust consists of nuclei coexisting with an electron gas to ensure charge neutrality. The Coulomb interaction between the nuclei leads to their lattice arrangement [Oyamatsu et al., 1984]. If one goes deeper into the crust, the ratio of neutrons with respect to the total nucleon number increases. This is requested to satisfy *β-equilibrium* and is driven by the increase of the density in the star. Eventually, the excess of neutrons in the nuclei gets so high that they drip out from the nuclei and create a dilute neutron gas. From now on, we will speak of *nuclear clusters* instead of nuclei [Ravenhall et al., 1983]. This phenomenon defines the limit between the outer crust and the inner crust. In consequence, to the mechanical equilibrium is added the chemical equilibrium between the clusters and the neutron gas. In a few words: the inner crust is inhomogeneous and presents two nuclear fluids in equilibrium. This complicated structure and composition is at the origin of many characteristic properties of neutron stars [Chamel and Haensel, 2008, Page and Reddy, 2012].

The dilute neutron gas in which clusters are immersed, is assumed to be superfluid. In fact the temperature of a neutron star $T \sim 10-100$ keV [Yakovlev et al., 2001], is much lower than the critical temperature of the superfluid neutron gas $T_c \sim 1-2$ MeV [Gezerlis and Carlson, 2010]. Under these conditions we expect the appearance of a Goldstone mode in the gas [Anderson, 1958]. This collective mode is responsible of another contribution to the heat capacity of the star and may affect its cooling. Actually, cooling calculations are done thanks to heat capacity and thermal conduction calculations. However, the contribution of the collective modes to heat capacity is in general neglected, because of the strong (exponential) suppression of the contribution calculated from BCS theory [Fortin et al., 2010]. Hence, in Part II we treat the contribution to the heat capacity of the superfluid neutron gas. We propose to compare two approaches: a microscopic (the so-called quasi-particle random phase approximation, *QRPA*) and a macroscopic one (hydrodynamics).

Concerning the nuclear clusters, they play a major role because of their impact on the equation of state of the crust of the star, and on thermodynamical and transport properties. One can approximate the inner crust as two fluids coexisting in chemical and mechanical equilibrium. Such approximations neglect the properties of the surface of the clusters and the Coulomb interaction. Nevertheless, these interactions play a major role as Ravenhall and Pethick pointed out in 1983 [Ravenhall et al., 1983]. The competition between these two energy contributions affects the shape of the clusters. The deformation of the clusters is expected to be important, up to exotic phases of rods or plates of bound nucleons. In addition, the clusters remain arranged in a lattice (as in the outer crust) [Oyamatsu et al., 1984]. The inhomogeneities affect the physical properties of the inner crust, such as the pressure (which may affect the mass-radius relation), and also the transport properties (neutrino scattering). Actually, since Oppenheimer, Volkoff and Tolman [Oppenheimer and Volkoff, 1939, Tolman, 1939], the inner crust description has been improved and has modified the neutron star descriptions [Avancini et al., 2008, Erler et al., 2013]. In Part III the inner crust structure and composition will be discussed within the extended Thomas-Fermi framework [Brack et al., 1985] and compared to other simple models.

The superfluidity of the neutron gas affects the dynamics of the inner crust collective modes [Magierski and Bulgac, 2004b, Chamel, 2013, Page and Reddy, 2012]. In fact, the nuclear clusters are made of neutrons and the surrounding gas too, so the dynamics of the clusters cannot be independent of that surrounding gas. This effect is called *entrainment* and leads to an modification [Chamel, 2013, Magierski and Bulgac, 2004b] of the effective number of nucleons moving with the cluster compared to the number of nucleons bound in the cluster. This effect modifies the ratio of superfluid neutrons, which are considered responsible for glitches [Anderson and Itoh, 1975, Pines and Alpar, 1985, Link et al., 1999, Shapiro and Teukolsky, 2004, Chamel and Carter, 2006]. Some of the pulsars (rotating neutron stars) present glitches, i.e., sudden changes of the rotation period. It is understood as a transfer of angular momentum from the superfluid part of the star (non-viscous fluid) and the normal fluid part. The hydrodynamics of the inner crust and its impacts on the astrophysical observations will be detailed in Part IV.

Let us begin in Part I by introducing the basics of neutron stars and of nuclear physics.

Part I

General aspects

Chapter 1

Neutron star generalities

1.1 History and discovery

The existence of the neutron stars was proposed by Baade and Zwicky in 1934 [Baade and Zwicky, 1934]. They supposed that the neutron stars are compact objects, i.e., they have a small size and a high mass. In addition, they early predicted that neutron stars could be formed in the supernova explosions.

The first calculations of the neutron star structure were done by Oppenheimer and Volkoff [Oppenheimer and Volkoff, 1939] and based on the calculations of Tolman [Tolman, 1939], both published in 1939. In order to calculated the Equation of State (EoS) of the neutron star matter, they assumed that the star is made of an ideal gas of free neutrons. Nowadays, the Tolman-Oppenheimer-Volkoff (TOV) equation is still used for non-rotating stars or slowly rotating, i.e., spinning less than ~ 200Hz (beyond this frequency the deformation cannot be neglected anymore). Nevertheless, since the work of Oppenheimer and Volkoff, the EoS have been improved by including the protons, the interactions (between nucleons), and the inhomogeneities within the crust, e.g., see Refs. [Avancini et al., 2008, Erler et al., 2013].

The interest in the neutron stars grew with new observations. In 1962, Giacconi *et al.* identified the first sources of cosmic X-rays outside the solar system [Giacconi et al., 1962]. Some of these sources where identified as neutron stars, while the X-ray signal received is a marker of their cooling. Few years later, in 1968, J. Bell and A. Hewish observed the first pulsar signal [Hewish et al., 1968]. However, when they did the observation, the nature of this radio source was not known, so they named it *Little Green Men 1* (LGM-1). Then, it turned out that the pulsed signal came from a rotating neutron star, which emits only from its magnetic poles. In a more simple scheme, the pulsar signal can be interpreted as the rotating light signal of a lighthouse.

Since these essential discoveries, the description of the neutron star have become more complete. The pulsar signal has been observed in X and Gamma rays. And concerning the neutron star cooling, it has been observed in the visible and in the infrared wave lengths. In parallel, theoretical studies of neutron stars have provided explanations of theses observations, and have predicted more precise characteristics, e.g., internal structure [Ravenhall et al., 1983], superfluidity [Pines and Alpar, 1985], mass-radius relations [Avancini et al., 2008], etc.

1.2 Formation

Remarkably, Baade and Zwicky [Baade and Zwicky, 1934] predicted already in 1934 the formation of neutron stars in the supernova explosions. Actually, this assumption was verified by the observation of neutron stars in nebulae formed after a supernova, e.g., the Crab nebula (Fig. 1.1). The supernova corresponds to the end of the stellar evolution of a massive star and causes its destruction. This explosion is extremely violent and bright enough to be visible even during daylight. Supernovae can be dived in two different explosion mechanisms: (i) the thermonuclear supernovae (kind Ia) and (ii) the gravitational core-collapse supernovae (kinds Ib, Ic and II). With respect to the mechanism of the explosion, only the core-collapse one produces a remnant body.

The core-collapse happens to massive stars $M \sim 10-20 M_{\odot}$, with $M_{\odot}$ the mass of the sun [Chamel and Haensel, 2008]. Theses stars are organized in layers of different chemical elements, which have been produced by the nuclear burning of the star (fusion reactions). The less dense layers are at the surface of the star, while the most dense are closer to the core. Because of the high temperature and the high pressure inside the massive star, the fusion reactions can reach the iron (^{56}Fe) production [Shapiro and Teukolsky, 2004] (the most stable element with respect to its binding energy per nucleon). In consequence, the core is made of iron, and is kept gravitationally stable because of the pressure of the degenerate electron gas [Shapiro and Teukolsky, 2004]. However, the nuclear burning is continuously producing more and more iron nuclei, which increase the density of the core. The density will be, at some point, sufficient to modify the β-equilibrium. It corresponds to the equilibrium between the neutron decay $n \to p\ e^-\ \bar{\nu}_e$, and the electronic capture $p\ e^- \to n\ \nu_e$. In terms of energy the β-equilibrium reads as: $\mu_n - \mu_p = \mu_e$, with μ_i the chemical potential of neutron,

Figure 1.1: The Crab nebula and its pulsar viewed in X-rays (Chandra, blue), optical wave length (Hubble, yellow and red) and in infrared (Spitzer, purple). The Crab pulsar is clearly visible as the bright dot in the center of the image. Surrounding the pulsar, the hot gas (in blue) emits in X-rays. The remnant cloud (mainly purple) is the Crab nebula, colder than the center, it emits in optical and infrared. This cloud is formed of the ejecta of the outer layers of the former massive star. *Credits: X-ray: NASA / CXC / SAO / F.Seward; Optical: NASA / ESA / ASU / J.Hester & A.Loll; Infrared: NASA / JPL-Caltech / Univ. Minn. / R.Gehrz.*

proton and electron, respectively. This displacement of the β-equilibrium is in favor of the electron capture. In fact, the Fermi level of the electrons grows faster with the density than the nucleon one, the electrons are relativistic. This displacement makes the neutron decay less favored than the electronic capture, and rarefies the number of electrons in the medium. The last effect is catastrophic for the stability of the core, strongly dependent of the electron pressure. Thus, the density of the core will reach an upper limit[1], above which the electron pressure is not enough sufficient to keep the core stable, and the core-collapse begins [Shapiro and Teukolsky, 2004].

The core of the massive star collapses in a few tenths of a second [Foglizzo et al., 2015], into a *Proto-Neutron-Star* (PNS). In these few mo-

---

[1] Typically, one speaks about the Chandrasekar mass.

ments the radius of the core contracts from about $1.5 \cdot 10^3$ km to $\sim$ 50 km. In contrast, the upper layers (H, He, C, Ne) did not collapse [Yakovlev et al., 2001], and start a supersonic free fall, until reaching the PNS just formed. Then, they bounce on the PNS, which creates a first shock wave, but not sufficient enough to trigger the supernova explosion [Bethe and Wilson, 1985]. However, the β-equilibrium yields a huge number of neutrinos[2]. Some of them escape from the supernova but, those which are trapped inside are heating the medium. This neutrino flare is extremely important for the supernova, indeed it generates a big convection in the collapsing star, and generates the *restart* of the explosion [Bethe and Wilson, 1985]. Consequently, this restart initiates the full supernova explosion.

The remnant object after the supernova explosion could be a either neutron star or a black hole (this depends of the mass of the massive star). Finally, the external layers are dispersed in the interstellar medium, and will form a nebula.

1.3 Characteristics

The neutron stars are produced by a sudden contraction of the core of a massive star. Typically, the mass of a neutron star is between $M_\odot$ and $2M_\odot$ [Demorest et al., 2010], for a radius of $\sim$ 10 km [Yakovlev et al., 2001]. This is an extremely compact object, in contrast to the radius of the sun is $7 \cdot 10^5$ km. Hence, the gravitational field surrounding a neutron star is extremely intense and gives rise to relativistic effects. In this case the compactness Ξ of the star, is close to 0.1. It is defined as ratio of the gravitational radius R_g (half of the Schwarzschild radius[3]) over the observed radius:

$$\Xi = \frac{R_g}{R} = \frac{GM}{Rc^2}, \tag{1.1}$$

with G the gravitational constant, M the mass and R the radius of the star. The order of magnitude of Ξ of a neutron star is ~ 0.1, while that of the sun

---

[2] In 1987, the supernova SN1987A, was the first one for which a neutrino signal was detected. Indeed the supernova was detected by three different neutrino detectors (Kamiokande, IMB, Baskan), about two hours before the light of the explosion arrived on Earth [Arnett et al., 1989]. Usually one considers that most of the gravitational energy gained during the contraction is released in the neutrino flare [Foglizzo et al., 2015]. Here, the graviational energy released is expected to be in the order of magnitude of 10^{46} Joules [Arnett et al., 1989]

[3] The Schwarzschild radius $R_s = 2GM/c^2$ is defined as the radius, for an object of mass M, at which the escape velocity is the equal to the speed of light c.

is ~ 10^{-6}. Therefore, the density inside the neutron star can reach up to 10^{15} g cm^{-3}.

1.3.1 Structure

The internal structure of a neutron star is not homogeneous, but presents three main layers [Chamel and Haensel, 2008] (Fig. 1.2):

(i) The *outer crust* ($0.3-0.5$ km) is first layer of the neutron star. It corresponds to a crystalline arrangement of nuclei immersed in a relativistic electron gas which ensures charge neutrality. With respect to the Coulomb energy, the most favorable arrangement is the Body Centered Cubic (BCC) lattice. At the surface of the outer crust one can find iron nuclei, but by descending inside the outer crust the medium density produces exotic neutron-rich nuclei. This last point is due to the β-equilibrium displacement driven by the increasing density.

(ii) The *inner crust* ($1-2$ km) starts when the neutron excess gets so strong that some neutrons are no longer bound to the nuclei. The bound nuclear structures (*clusters*) remain stable, and are surrounded by a neutron and electron gas. The system tends to reach the most favorable state. Remarkably, the surface and Coulomb energies play a relevant role in the energy minimization. The surface energy tends to increase the size of the clusters, while Coulomb energy tends to reduce it. This competition affects the geometry and give rise to exotic structures, the so-called *pasta phases*. They were introduced by [Ravenhall et al., 1983], and they predicted the following geometries:

  - The *crystalline phase*, is in the continuity of the outer crust. It corresponds to spherical clusters, arranged in a BCC lattice. They are immersed in a neutron and electrons gas.
  - The *spaghetti phase* is expected to be the result of the merging of the former spherical clusters into rods. By being cylindrical the clusters reduce their contribution to the surface energy.
  - Finally the *lasagna phase*, is the superposition of bound nucleons and neutron gas layers. It is obtained by merging the rods into plates, i.e., it consists of alternating dense and dilute layers. Similarly, this modification of the geometry decreases the surface energy.
  - The *inverse phases* are also expected. They correspond to the ones detailed previously, but with the geometries of higher and lower

density interchanged: tubes, holes ("Swiss cheese"). This point will be discussed in detail in the Part III.

(iii) The *core* of the star (~ 10 km) is defined as the uniform part of it. The inhomogeneities discussed (in the preceding points) disappeared, and matter becomes homogeneous. In the upper layers of the core we expect a coexistence of neutrons, protons and electrons. Nevertheless, in the deepest parts of the star the density is high and the emergence of hyperons or quark gluon plasma might be energetically favorable.

1.3.2 Cooling of the neutron star

When the PNS is formed after a very hot supernova explosion, its internal temperature is $T \sim 10^{11}$ K [Yakovlev et al., 2001]. About $10-20$ s after its formation, the star become transparent to neutrinos and starts to cool down [Chamel and Haensel, 2008]. Surprisingly, the cooling of the star is not uniform. In fact, during the first year, the core, the inner and the outer crust are cooling almost independently [Yakovlev et al., 2001]. Within less than a month the outer crust cools to 10^9 K and the core stars to cool down thanks to neutrino emission due to electron capture and β-decay. However, the inner crust temperature remains almost constant while the other layers are cooling. After ~ 10 years the inner crust suddenly cools down, the luminosity of the star drops by four orders of magnitude [Yakovlev et al., 2001]. This phenomenon is the named crust relaxation. Finally, ~ 50 years after the formation of the PNS, the star is considered to be isothermal [Yakovlev et al., 2001] and starts a slow cooling process driven by X-ray emission [Chamel and Haensel, 2008, Fortin et al., 2010]. Figure 1.3 provides some theoretical and observed cooling curves of the surface temperature.

Nevertheless, we remarked in the preceding paragraph that the inner crust plays a major role in explaining the cooling. It turns out that its heat capacity and conduction affect strongly the entire cooling of the star [Fortin et al., 2010]. The major contribution to the inner crust heat capacity comes from the electron contribution and phonons of the Coulomb lattice. However, the superfluidity of the inner crust plays also non-negligible role. Indeed, the dilute neutron gas is cold enough to be superfluid. The work by [Fortin et al., 2010] focused on the superfluidity effect on the cooling, by modifying its strength. Even so, only thermal neutron quasiparticle excitation were taken into account, whole collective excitations of the neutrons were neglected. In the next chapters, we will focus on the contribution of the

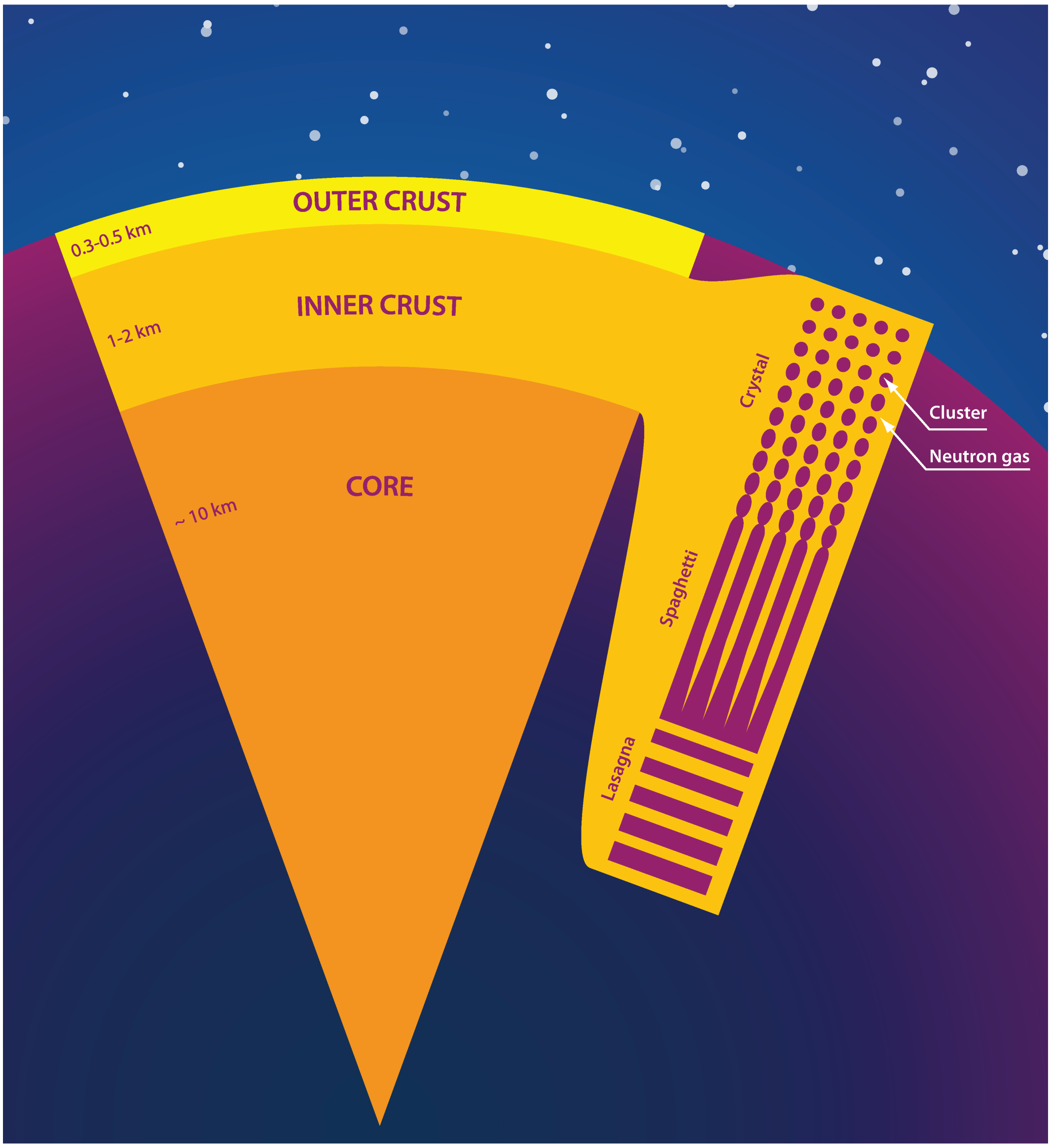

Figure 1.2: A schematic view of the neutron star internal structure. The zoom on the left of the inner crust, details its composition. Here, the inverse phases are not included according to the conclusions made in Part III.

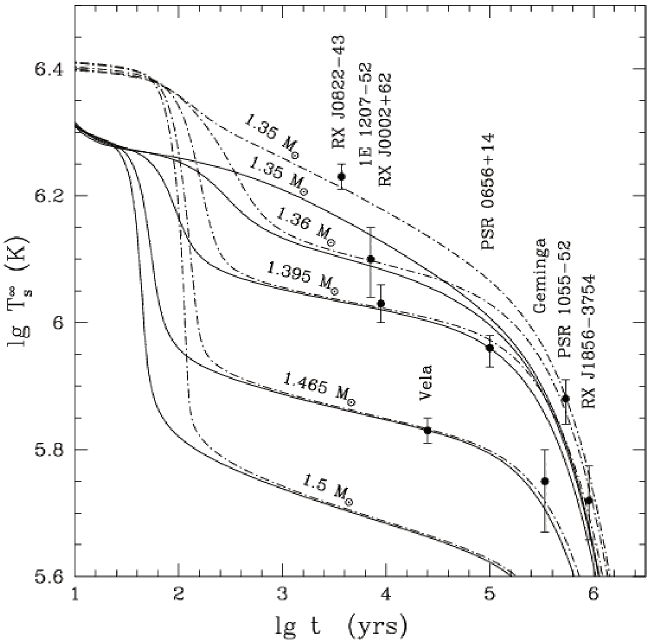

Figure 1.3: Temperature seen by an observer for different neutron star masses, as function of the age of the neutron star. Theoretical calculations are compared to observations (dots). The dashed lines include the proton superfluidity in the core, while the solid lines correspond to calculations with neutron superfluidity in the crust. *Credits: Yakovlev* et al. *[Yakovlev et al., 2001].*

collective excitations originating from the neutron superfluidity, because of the broken U(1) symmetry of the pairing field, see Part II.

1.3.3 Pulsar signal and glitches

Pulsars were discovered by J. Bell and A. Hewish [Hewish et al., 1968] in 1968, as a rapidly and regularly pulsating radio source, see Fig. 1.4. It turned out to be a rotating neutron star emitting from its magnetic poles. Since this essential discovery, many other pulsars have been observed, from rotation periods of few seconds to milliseconds (the full pulsar catalog is available on-line [ATNF, 2016]). This pulse periodicity is extremely regular, e.g., the frequency Ω of the Vela pulsar (J0835-4510) slows down with $\dot{\Omega} = -1.57 \cdot 10^{-11}$ s^{-2} [ATNF, 2016]. The loss of angular momentum is due to the emission of electromagnetic radiation by the rotating magnetic field. However, for some neutron stars one observes from time to time “glitches”:

suddenly the pulsar rotates faster [Shapiro and Teukolsky, 2004]. This gain of rotation velocity is explained by a transfer of angular momentum, from the superfluid neutrons to the rigid part that rotates at the observed rate. Thus, glitches are witnesses of the superfluidity [Anderson and Itoh, 1975, Pines and Alpar, 1985, Chamel and Haensel, 2008] inside the neutron star. In addition, not only the superfluidity, but also the structure of the inner crust affects the glitches [Chamel, 2013], refer to Chapter 9.

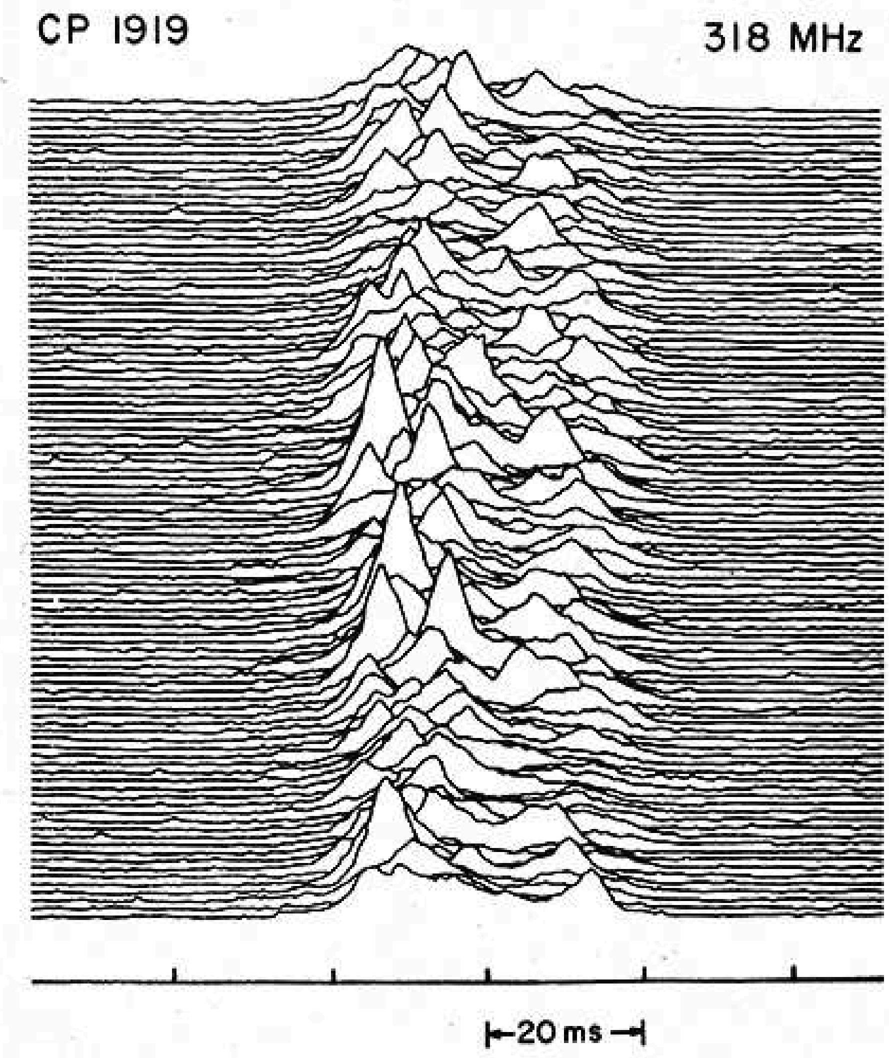

Fig. 2. – 100 consecutive pulses from the pulsar CP 1919. Time increases from bottom to top. Pulsar period is 1.34 seconds.

Figure 1.4: The pulsar signal from LGM-1 (PSR B1919+21 or CP 1919), the first pulsar to be observed by Jocelyn Bell in 1968 [Hewish et al., 1968]. *Credits: The figure is extracted from the PhD thesis of Harold D. Craft [Craft Jr., 1970].*

Chapter 2

Interactions between nucleons

2.1 The nuclear many-body problem

The nuclear many-body problem is hard to solve because of experimental and theoretical limitations [Ring and Schuck, 1980]. Actually, the form of the nuclear interaction is not precisely known. Also, one knows that the interaction contains higher interaction terms between nucleons, such as 3-body or 4-body interactions. It leads to a very complicated solution of the system. In addition, the direct measurement of higher interaction terms is practically impossible. Nowadays, only two-nucleon scatterings can be performed. Let us introduce a typical expression of an Hamiltonian of a nucleus which contains A nucleons:

$$\hat{H} = \sum_{i=1}^{A} \frac{\hat{\mathbf{k}}_i^2}{2m} + \sum_{i<j}^{A} \hat{v}_{i,j} + \sum_{i<j<k}^{A} \hat{v}_{i,j,k} + \cdots , \tag{2.1}$$

with $\hat{v}_{i,j}$ and $\hat{v}_{i,j,k}$ the 2 and 3-body interaction terms, respectively. In this example, the higher terms of the interaction between nucleons are not explicitly written only for simplicity. In practice, the exact solution of the system is given by the Schrödinger equation

$$\hat{H} \left|\psi\right\rangle = E \left|\psi\right\rangle , \tag{2.2}$$

with $\left|\psi\right\rangle$ the wave function. Nevertheless, the analytical solution of the preceding equation does not exist if $A > 2$. (Note that the conclusion is similar for the time dependent Schrödinger equation.)

Thus, three main approaches were developed to solve the nuclear many-body problem:

(i) The *ab-initio* method tries to solve the Schrödinger equation exactly. The framework uses the most general form of the wave function for a "realistic" NN interaction. However, the ab-initio method is limited to light nuclei because of numerical computing limitations (processor power and memory).

(ii) The *shell model* describes the excitations of a nucleus, by assuming that it is made of *valence* nucleons moving in a mean-field potential created by the *core* nucleons [Ring and Schuck, 1980]. The number of valence nucleons is a parameter of the calculation and has to be chosen as big as necessary to describe the excited configurations. The valence nucleons interact via an effective residual interaction, which depends on the number of levels one uses for the valence nucleons. The model is limited by the number of valence nucleons, which increases the number of configurations, so that the complexity of the calculations.

(iii) The *mean field* approach treats the nucleons as independent particles in an effective mean field [Ring and Schuck, 1980]. The mean field is the averaged field created by all nucleons in the system and felt by one of them. Thus we have to proceed iteratively until convergence. In contrast to the shell model, the mean field approximation does not give directly excited states. This approach turned out to be most successful for big nuclei ($A \gtrsim 20$), while it is less precise for light nuclei. In the next sections and chapters, we will only focus on the mean field approach.

2.2 Hartree-Fock approximation

The mean field approach is based on the assumption that nucleons are independent particles moving in a mean field potential. This leads to the Hartree-Fock (HF) approximation. In this case, the HF wave function Ψ_{HF} is expressed as a Slater determinant of the single-particle wave functions $\{\psi_i\}$ [Fetter and Walecka, 1971]:

$$\Psi_{HF} = \frac{1}{\sqrt{A!}} \det|\psi_1 \cdots \psi_A| . \tag{2.3}$$

The single-particle wave function are determined by minimizing the total energy of the nucleus

$$E_{HF} = \frac{\langle \Psi_{HF}|\hat{H}|\Psi_{HF}\rangle}{\langle \Psi_{HF}|\Psi_{HF}\rangle} . \tag{2.4}$$

The energy minimization is performed with the help of the variational principle [Ring and Schuck, 1980].

It turns out that the optimal single-particle wave functions satisfy the Schrödinger equation, which contains of the HF mean field. The mean field is fully determined by all the single-particle wave functions $\boldsymbol{\psi} = \{\psi_i\}$, so the system is self-consistent. Hence, the Schrödinger equation is expressed as follows

$$\left\{-\frac{\nabla^2}{2m} + U_{HF}\left[\boldsymbol{\psi}\right]\right\}\psi_i = \epsilon_i \psi_i \,. \tag{2.5}$$

In conclusion, the solution is obtained after numerical iterations, when the HF energy converged.

2.3 Nuclear interaction

So far, we introduced a general Hamiltonian (2.1) made of a NN interaction. However, if one wants to use HF approximations, an effective interaction is required, which accounts in some way for the correlations neglected in the HF wave function. Within the framework of the nuclear many-body problem, numerous effective interactions have been built, such as Skyrme, Gogny or relativistic mean-field (RMF). In the next subsections, we will detail the form and the properties of the Skyrme forces.

2.3.1 Skyrme energy-density functional

Let us start by briefly summarizing the description of neutron matter using the Skyrme energy-density functional (EDF). The Skyrme functionals [Vautherin and Brink, 1972] have been fitted to a large variety of nuclear data. In addition, in order to be more predictive for neutron-rich nuclei, they have also been fitted to the equation of state of neutron matter [Chabanat et al., 1997, Chabanat et al., 1998]. The functional can be written as a sum of many contributions [Chabanat et al., 1998]:

$$\begin{aligned}
\mathscr{E}_{\text{Skyrme}} = & \frac{1}{2m}(\tau_n + \tau_p) \quad \text{kinetic energy} \\
& + \frac{1}{4} t_0 \left[(2 + x_0)\rho^2 - (2x_0 + 1)(\rho_n^2 + \rho_p^2)\right] \quad \text{central term} \\
& + \frac{1}{24} t_3 \rho^\sigma \left[(2 + x_3)\rho^2 - (2x_3 + 1)(\rho_n^2 + \rho_p^2)\right] \quad \text{density dependent} \\
& + \frac{1}{8}\left[t_1(2 + x_1) + t_2(2 + x_2)\right]\rho\tau \quad \text{effective mass} \\
& + \frac{1}{8}\left[t_2(2x_2 + 1) - t_1(2x_1 + 1)\right](\rho_n\tau_n + \rho_p\tau_p) \quad \textit{idem}
\end{aligned}$$

$$\begin{aligned}
&+\frac{1}{32}\left[3t_1(2+x_1)-t_2(2+x_2)\right](\nabla\rho)^2 \quad \text{finite range}\\
&-\frac{1}{32}\left[3t_1(2x_1+1)+t_2(2x_2+1)\right]\left[(\nabla\rho_n)^2+(\nabla\rho_p)^2\right] \quad \textit{idem}\\
&+\frac{1}{2}W_0\left[\mathbf{J}\cdot\nabla\rho+\mathbf{J}_n\cdot\nabla\rho_n+\mathbf{J}_p\cdot\nabla\rho_p\right] \quad \text{spin-orbit}\\
&-\frac{1}{16}(t_1x_1+t_2x_2)\mathbf{J}^2+\frac{1}{16}(t_1-t_2)\left[\mathbf{J}_n^2+\mathbf{J}_p^2\right], \quad \text{tensor} \qquad (2.6)
\end{aligned}$$

with the parameters $t_{0,\dots,3}$ and $x_{0,\dots,3}$ defined for each Skyrme parametrization, e.g., see Refs. [Negele and Vautherin, 1973, Chabanat et al., 1998, Goriely et al., 2013]. The densities of the functional $\rho=\rho_n+\rho_p$, $\tau=\tau_n+\tau_p$ and $\mathbf{J}=\mathbf{J}_n+\mathbf{J}_p$ are expressed as:

$$\rho_q(\mathbf{r})=\sum_{i,\sigma}\left|\psi_i^q(\mathbf{r},\sigma)\right|^2, \qquad (2.7a)$$

$$\tau_q(\mathbf{r})=\sum_{i,\sigma}\left|\nabla\psi_i^q(\mathbf{r},\sigma)\right|^2, \qquad (2.7b)$$

$$\mathbf{J}_q(\mathbf{r})=\sum_{i,\sigma,\sigma'}\psi_i^{q*}(\mathbf{r},\sigma')\nabla\psi_i^q(\mathbf{r},\sigma)\times\langle\sigma'|\underline{\boldsymbol{\sigma}}|\sigma\rangle, \qquad (2.7c)$$

with $\psi_i^q(\mathbf{r},\sigma)$ the single-particle wave function. The quantum numbers i, σ and q denote the orbital, the spin and the isospin, respectively. The sums in Eqs. (2.7a)–(2.7c) run over the occupied states only. The isospin is defined $q=(n,p)$ for *neutrons* and *protons*, respectively.

In addition, because of the velocity-dependent terms of the functional (2.6), one can define an effective mass:

$$\begin{aligned}
\frac{1}{2m_q^*}=\frac{1}{2m}&+\frac{1}{8}\left[t_1(2+x_1)+t_2(2+x_2)\right]\rho\\
&+\frac{1}{8}\left[t_2(1+2x_2)-t_1(1+2x_1)\right]\rho_q. \qquad (2.8)
\end{aligned}$$

2.3.2 Pure neutron matter

Focusing on the Pure Neutron Matter (PNM), the energy density functional (2.6) can be written as

$$\mathscr{E}_{\text{Skyrme}}=\frac{1}{2m}\tau+\frac{s_0}{4}\rho^2+\frac{s_3}{24}\rho^{\alpha+2}+\frac{s_1+3s_2}{8}(\rho\tau-\mathbf{j}^2)+3\frac{s_1-s_2}{16}(\nabla\rho)^2, \qquad (2.9)$$

with parameters $s_{0,\dots,3}$ and α which are defined in Appendix A. In Eq. (2.9), ρ denotes the number density of neutrons ($\rho=\rho_n$), τ is the kinetic energy density (multiplied by $2m$, where m is the neutron mass), and $\mathbf{j}$ is the current. In the limit of neutron matter, the density can be expressed in terms of the density matrix

$$\rho_{\mathbf{k},\mathbf{k}'} = \langle a^\dagger_{\mathbf{k}'\uparrow} a_{\mathbf{k}\uparrow} \rangle \,, \tag{2.10}$$

where a and $a^\dagger$ denote, respectively, neutron annihilation and creation operators. The densities of Eq. (2.9) are defined as

$$\rho(\mathbf{r}) = 2 \sum_{\mathbf{k},\mathbf{k}'} \rho_{\mathbf{k},\mathbf{k}'} e^{i(\mathbf{k}-\mathbf{k}')\cdot\mathbf{r}} \,, \tag{2.11a}$$

$$\tau(\mathbf{r}) = 2 \sum_{\mathbf{k},\mathbf{k}'} \mathbf{k}\cdot\mathbf{k}' \rho_{\mathbf{k},\mathbf{k}'} e^{i(\mathbf{k}-\mathbf{k}')\cdot\mathbf{r}} \,, \tag{2.11b}$$

$$\mathbf{j}(\mathbf{r}) = \sum_{\mathbf{k},\mathbf{k}'} (\mathbf{k}+\mathbf{k}') \rho_{\mathbf{k},\mathbf{k}'} e^{i(\mathbf{k}-\mathbf{k}')\cdot\mathbf{r}} \,. \tag{2.11c}$$

Here we have assumed that the density matrices for both spin projections $(\uparrow,\downarrow)$ are equal. The term proportional to $\mathbf{j}^2$ in Eq. (2.9) is necessary to ensure Galilean invariance [Engel et al., 1975]. Note that we did not write the spin-orbit interaction since it is absent in spin-unpolarized matter.

In uniform matter, the functional (2.9) gives rise to a constant Hartree-Fock (HF) potential U_{HF} and an effective mass m^*. The former is the first derivative of Eq. (2.9) with respect to ρ, while the effective mass is due to the τ dependence of the Skyrme functional [Chabanat et al., 1998]:

$$U_{\mathrm{HF}} = \frac{s_0}{2}\rho + \frac{\alpha+2}{24} s_3 \rho^{\alpha+1} + \frac{s_1+3s_2}{8}\tau \,, \tag{2.12a}$$

$$\frac{1}{2m^*} = \frac{1}{2m} + \frac{s_1+3s_2}{8}\rho \,. \tag{2.12b}$$

We absorb U_{HF} in an effective chemical potential $\mu^* = \mu - U_{\mathrm{HF}}$, so that the single-particle spectrum can be written as

$$\xi_{\mathbf{k}} = \epsilon_{\mathbf{k}} - \mu = \frac{k^2}{2m^*} - \mu^* \,. \tag{2.13}$$

To study collective excitations within the RPA (or QRPA), one needs the residual interaction between quasiparticles. The corresponding matrix elements in the *particle-hole* (*ph*) channel are obtained from the Skyrme functional as follows [García-Recio et al., 1992]:

$$V^{\mathrm{ph}}_{\mathbf{k}_1,\mathbf{k}_2,\mathbf{k}_4,\mathbf{k}_3} = \frac{\delta^2 E_{\mathrm{Skyrme}}}{\delta\rho_{\mathbf{k}_1,\mathbf{k}_2}\,\delta\rho_{\mathbf{k}_4,\mathbf{k}_3}} \,, \tag{2.14}$$

where $E_{\mathrm{Skyrme}} = \int d^3r\,\mathscr{E}_{\mathrm{Skyrme}}$ is the energy. The conservation of the total momentum $\mathbf{q}$ of the ph pair implies that V^{ph} is proportional to $\delta_{\mathbf{k}_1-\mathbf{k}_2,\mathbf{k}_3-\mathbf{k}_4}$.

After transformation to relative and total momenta of the ph pairs, the matrix element can conveniently be written in the form [Navarro et al., 1999]

$$V^{\mathrm{ph}}_{\mathbf{k}+\frac{\mathbf{q}}{2},\mathbf{k}-\frac{\mathbf{q}}{2},\mathbf{k}'-\frac{\mathbf{q}'}{2},\mathbf{k}'+\frac{\mathbf{q}'}{2}} = [W_1(q) + W_2(\mathbf{k}-\mathbf{k}')^2]\delta_{\mathbf{q},\mathbf{q}'} . \tag{2.15}$$

The explicit expressions for $W_1(q)$ and W_2 in terms of the parameters of the Skyrme functional are given in the Appendix A.

2.4 Pairing correlations

2.4.1 Bardeen-Cooper-Schrieffer theory

In order to account for the superfluidity of the neutron gas, we have to include pairing. We do this in the framework of the Bardeen-Cooper-Schrieffer (BCS) theory [Bardeen et al., 1957], which treats the ground state with a variational wave function:

$$|\Psi_0\rangle = \prod_{\mathbf{k}}(u_k + v_k\, a^\dagger_{\mathbf{k}\uparrow} a^\dagger_{-\mathbf{k}\downarrow})|0\rangle\,, \tag{2.16}$$

where u_k and v_k are the variational parameters. By convention, spins *up* are associated to particles of momentum $\mathbf{k}$, and spins *down* to $-\mathbf{k}$. The ansatz (2.16) for the ground state implies a superposition of states and does not conserve the number of particles in the system. This could be problematic in a system with a small number of particles, e.g., a nucleus. Here, in contrast, the neutron matter is assumed to be uniform and infinite. The variational parameters are normalized as [Fetter and Walecka, 1971]:

$$|u_k|^2 + |v_k|^2 = 1\,. \tag{2.17}$$

We introduce a Lagrange multiplier μ to obtain the correct average number of particles in the system. The Hamiltonian is thus modified:

$$H' = H - \mu N\,, \tag{2.18}$$

with $N = \sum_{\mathbf{k},\sigma} a^\dagger_{\mathbf{k},\sigma} a_{\mathbf{k},\sigma}$ the total number of particles. Because of the preceding transformation, one can define the Hamiltonian as follows [Fetter and Walecka, 1971]:

$$\begin{aligned} H' &= \sum_{\mathbf{k},\sigma}(\epsilon_k - \mu)\, a^\dagger_{\mathbf{k},\sigma} a_{\mathbf{k},\sigma} \\ &+ \frac{1}{2} \sum_{\mathbf{k}_1,\sigma_1,\ldots,\mathbf{k}_4,\sigma_4} \langle \mathbf{k}_1,\sigma_1,\mathbf{k}_2,\sigma_2 | V^{\mathrm{pp}} | \mathbf{k}_4,\sigma_4,\mathbf{k}_3,\sigma_4\rangle\, a^\dagger_{\mathbf{k}_1,\sigma_1} a^\dagger_{\mathbf{k}_2,\sigma_2} a_{\mathbf{k}_4,\sigma_4} a_{\mathbf{k}_3,\sigma_3} \\ &\qquad \times \delta_{\mathbf{k}_1+\mathbf{k}_2,\mathbf{k}_3+\mathbf{k}_4}\,, \end{aligned} \tag{2.19}$$

with the *particle-particle* (*pp*) potential V^{pp} negative (attractive interaction).

In contrast to the previous section, here we neglect the HF mean-field. Furthermore, we consider only pairing in the $^1S_0$ channel, i.e., of neutrons with opposite spins, and disregard the $^3P_2$ channel, which becomes dominant at higher densities [Tamagaki, 1970]. So, the Hamiltonian (2.19) simplifies to:

$$H' = \sum_{\mathbf{k},\sigma} \xi_k \, a^\dagger_{\mathbf{k},\sigma} a_{\mathbf{k},\sigma} + \sum_{\mathbf{k}_1,\ldots,\mathbf{k}_4} V^{\mathrm{pp}}_{\mathbf{k}_1,\mathbf{k}_2,\mathbf{k}_4,\mathbf{k}_3} a^\dagger_{\mathbf{k}_1\uparrow} a^\dagger_{-\mathbf{k}_2\downarrow} a_{-\mathbf{k}_4\downarrow} a_{\mathbf{k}_3\uparrow} \times \delta_{\mathbf{k}_1-\mathbf{k}_2,\mathbf{k}_3-\mathbf{k}_4}\,, \tag{2.20}$$

with $V^{\mathrm{pp}}_{\mathbf{k}_1,\mathbf{k}_2,\mathbf{k}_4,\mathbf{k}_3} = \langle \mathbf{k}_1 \uparrow, -\mathbf{k}_2 \downarrow | V^{\mathrm{pp}} | -\mathbf{k}_4 \downarrow, \mathbf{k}_3 \uparrow \rangle$ the matrix element of the pairing interaction (for outgoing particles $\mathbf{k}_1 \uparrow$ and $-\mathbf{k}_2 \downarrow$, and incoming particles $\mathbf{k}_3 \uparrow$ and $-\mathbf{k}_4 \downarrow$).

2.4.2 Gap equation

Inside the Hamiltonian (2.20), one can identify the pairing gap Δ defined by the gap equation

$$\Delta_{\mathbf{k}_1,\mathbf{k}_2} = -\sum_{\mathbf{k}_3,\mathbf{k}_4} V^{\mathrm{pp}}_{\mathbf{k}_1,\mathbf{k}_2,\mathbf{k}_4,\mathbf{k}_3} \kappa_{\mathbf{k}_3,\mathbf{k}_4}\,, \tag{2.21}$$

and the anomalous density

$$\kappa_{\mathbf{k},\mathbf{k}'} = \langle a_{\mathbf{k}\uparrow} a_{-\mathbf{k}'\downarrow} \rangle\,. \tag{2.22}$$

The BCS wave function (2.16) can be rewritten as:

$$|\Psi_0\rangle = \prod_{\mathbf{k}} \frac{1}{v_k} \alpha_{\mathbf{k}} \beta_{-\mathbf{k}} |0\rangle\,. \tag{2.23}$$

where $\alpha_{\mathbf{k}}$ and $\beta_{\mathbf{k}}$ are *Bogoliubov operators* [Bogoliubov et al., 1959]. The motivation of Bogoliubov is to treat the ground state of a system as a quasiparticle vacuum, while the so-called quasiparticles are its low-lying excitations [Ring and Schuck, 1980]. Hence, the canonical Bogoliubov transformation in the BCS framework is written in the form [Fetter and Walecka, 1971]

$$\alpha_{\mathbf{k}} = u_k a_{\mathbf{k}\uparrow} - v_k a^\dagger_{-\mathbf{k}\downarrow} \quad \text{and} \quad \beta_{-\mathbf{k}} = u_k a_{-\mathbf{k}\downarrow} + v_k a^\dagger_{\mathbf{k}\uparrow}\,, \tag{2.24}$$

and the quasiparticle operators act on the ground state as follows

$$\alpha_{\mathbf{k}} |\Psi_0\rangle = \beta_{\mathbf{k}} |\Psi_0\rangle = 0\,. \tag{2.25}$$

With help of Eq. (2.17) one can show that the operators $\alpha_{\mathbf{k}}$ and $\beta_{\mathbf{k}}$ are quantized by the following anti-commutators:

$$\{\alpha_{\mathbf{k}}, \alpha^{\dagger}_{\mathbf{k}'}\} = \{\beta_{-\mathbf{k}}, \beta^{\dagger}_{-\mathbf{k}'}\} = \delta_{\mathbf{k},\mathbf{k}'}\,, \tag{2.26}$$

while all other combinations are zero.

Thanks to the Bogoliubov transformations, one can calculate the average values of creation and annihilation operator products, as function of the variational parameters (for more detail see Apx. C.1)

$$\langle\Psi_0|\, a_{-\mathbf{k}\downarrow} a_{\mathbf{k}\uparrow}\, |\Psi_0\rangle = \langle\Psi_0|\, a^{\dagger}_{\mathbf{k}\uparrow} a^{\dagger}_{-\mathbf{k}\downarrow}\, |\Psi_0\rangle = u_k v_k\,. \tag{2.27}$$

Hence, the expectation value of Eq. (2.20) is entirely determined by variational parameters:

$$\langle\Psi_0|H'|\Psi_0\rangle = \sum_{\mathbf{k}} \left(4\xi_{\mathbf{k}} v_k^2 - 2\Delta_{\mathbf{k}} u_k v_k\right), \tag{2.28}$$

where $\Delta_{\mathbf{k}}$ denotes the diagonal elements of $\Delta_{\mathbf{k},\mathbf{k}'}$. (In the ground state κ is diagonal, so that Δ is diagonal too.)

Because of the variational principle, the BCS ground state energy has to minimized by the variational parameters, and the variation of $\langle\Psi_0|H'|\Psi_0\rangle$ has to be zero [Ring and Schuck, 1980]. The preceding properties read as:

$$\left(\frac{\delta}{\delta u_k} + \frac{dv_k}{du_k}\frac{\delta}{\delta v_k}\right)\langle\Psi_0|H'|\Psi_0\rangle = 0\,, \tag{2.29}$$

and one finds after derivation

$$2\xi_k u_k v_k + \Delta_k(v_k^2 - u_k^2) = 0\,, \tag{2.30}$$

The result for u_k^2 and v_k^2 are obtained by combining the preceding result and Eq. (2.17):

$$u_k^2 = \frac{1}{2}\left(1 \pm \frac{\xi_k}{\sqrt{\xi_k + \Delta_k}}\right), \tag{2.31}$$

$$v_k^2 = \frac{1}{2}\left(1 \mp \frac{\xi_k}{\sqrt{\xi_k + \Delta_k}}\right). \tag{2.32}$$

$$\tag{2.33}$$

By convention we choose "+" for u_k and "−" for v_k, because in the limit of zero paring $\Delta_k = 0$, we expect $v_k = 1$ and $u_k = 0$ within the Fermi sea. Then the gap equation reads

$$\Delta_{\mathbf{k}} = -\sum_{\mathbf{k}'} V^{pp}_{\mathbf{k},\mathbf{k},\mathbf{k}',\mathbf{k}'} \frac{\Delta_{\mathbf{k}'}}{2E_{\mathbf{k}'}}\,, \tag{2.34}$$

with the usual quasiparticle energy

$$E_{\mathbf{k}} = \sqrt{\xi_{\mathbf{k}}^2 + \Delta_{\mathbf{k}}^2}\,. \tag{2.35}$$

2.4.3 Pairing interaction

So far we derived the ph interaction from Skyrme functional. We notice that the interactions we use for the pairing (pp channel) and for the mean-field (ph channel) are different. In principle, we have to use a realistic NN interaction for the description of the pairing. Since short-range correlations are included when we computed the gap equation. This is different from the effective interactions to be used in Hartree-Fock mean field, where the correlation effects are accounted for in an effective way via the density dependence of Skyrme EDF. Usually, in nuclear structure calculations with Skyrme, a contact interaction with (possibly) density dependent coupling constant is employed as pairing interaction (see e.g. [Khan et al., 2002]). However, the gap equation diverges if one uses such interactions. In order to solve this problem a cut-off is included (by hand) into the gap equation. In contrast to the latter pairing interaction, we use a simple separable approximation to a low-momentum interaction ($V_{\text{low-}k}$) derived from a realistic nucleon-nucleon force [Bogner et al., 2007]. Here, the calculation of the gap equation is equivalent to a T-matrix calculation and converges naturally. In addition, this interaction gives a reasonable density dependence of the superfluid critical temperature in low-density neutron matter [Ramanan and Urban, 2013]. Hence, for the pairing the approximation we use is

$$V^{\text{pp}}_{\mathbf{k}_1,\mathbf{k}_2,\mathbf{k}_4,\mathbf{k}_3} = -gF(\tfrac{1}{2}|\mathbf{k}_1+\mathbf{k}_2|)F(\tfrac{1}{2}|\mathbf{k}_3+\mathbf{k}_4|)\delta_{\mathbf{k}_1-\mathbf{k}_2,\mathbf{k}_3-\mathbf{k}_4}\,, \tag{2.36}$$

where g is the strength of the interaction and F is a Gaussian form factor

$$F(k) = e^{-k^2/k_0^2}\,. \tag{2.37}$$

The separable form of the pairing interaction simplifies a lot the solution of the gap equation: it is evident that $\Delta_{\mathbf{k}}$ is of the form $\Delta_{\mathbf{k}} = \Delta_0 F(k)$, and instead of an integral equation for the function $\Delta_{\mathbf{k}}$ one has to solve only an equation for the number Δ_0.

2.4.4 Uncertainties

The pairing interaction in nuclear or neutron matter presents some uncertainties related to in-medium effects and the bare interaction. Actually solving the BCS gap equation (2.34) is the most simple way of calculating the pairing gap energy. Beyond BCS, screening effects may appear and reduce the maximum of the gap energy [Cao et al., 2006], as displayed in Fig. 2.1 denoted with the label *Cao 06*. For low density, there are “exact” quantum

Monte-Carlo (QMC) calculations [Gezerlis and Carlson, 2010], see Fig. 2.1 labeled *QMC AV4*. This calculations give a gap about one half times smaller than the one calculated in BCS.

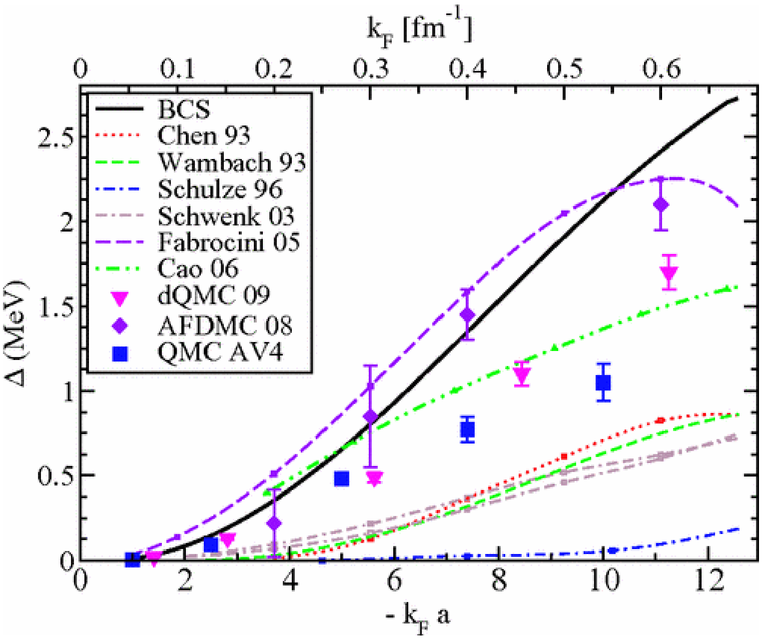

Figure 2.1: Comparison of different $^1S_0$ pairing gaps versus the Fermi momentum. The figure includes the QMC calculations performed by the authors. *Credits: A. Gezerlis and J. Carlson [Gezerlis and Carlson, 2010].*

Part II

Collective modes in uniform neutron matter

Chapter 3

Collective modes formalisms

3.1 Time Dependent Hartree-Fock-Bogoliubov

3.1.1 Motivations

In the preceding sections we exposed theories treating respectively particles or quasiparticles moving independently in a potential. The Hartree-Fock-Bogoliubov (HFB) theory is a generalization of the Hartree-Fock method to the pairing correlations between particles [Ring and Schuck, 1980]. We have to account for the superfluidity because of the observed temperature of the neutron star crust [Chamel and Haensel, 2008], which is far below from critical temperature of the superfluid neutron gas [Pines and Alpar, 1985]. In the HFB framework we consider quasiparticles in two potentials: (i) h the self-consistent mean-field potential, already introduced within the Hartree-Fock method, and (ii) Δ the pairing field treated in the BCS theory. The HFB only considers quasiparticles in a static picture, while the collective mode description requires a time-dependent approach. Hence, let us introduce the Time-Dependent HFB (TDHFB), the extension of the HFB theory to dynamical processes, including variations of large amplitude [Ring and Schuck, 1980].

3.1.2 Formalism

The starting point of the TDHFB is to build the equation of motion for the generalized density matrix quantities defined in the Hamiltonian. Generally, the equation of motion for an expectation value $\langle A \rangle$ is expressed in terms of the Hamiltonian H as:

$$i\langle \dot{A} \rangle = \langle [A,H] \rangle\,, \tag{3.1}$$

with $\langle \dot{A} \rangle$ the time derivative of $\langle A \rangle$.

As mentioned before, the TDHFB treats both ph correlations and pairing correlations, in second quantization the one-body mean-field Hamiltonian read as:

$$H = \sum_{\mathbf{k},\mathbf{k}'} \left(h_{\mathbf{k},\mathbf{k}'} \sum_{\sigma} a^{\dagger}_{\mathbf{k},\sigma} a_{\mathbf{k}',\sigma} - \Delta_{\mathbf{k},\mathbf{k}'} a^{\dagger}_{\mathbf{k}\uparrow} a^{\dagger}_{-\mathbf{k}'\downarrow} - \Delta^{\dagger}_{\mathbf{k},\mathbf{k}'} a_{-\mathbf{k}\downarrow} a_{\mathbf{k}'\uparrow} \right) . \tag{3.2}$$

Let us now write the equation of motion (EOM) of the normal and anomalous density matrices ρ and κ introduced in Eqs. (2.10) and (2.22), and also their complementary quantities:

$$\bar{\rho}_{\mathbf{k},\mathbf{k}'} = \langle a^{\dagger}_{-\mathbf{k}\downarrow} a_{-\mathbf{k}'\downarrow} \rangle , \qquad \kappa^{\dagger}_{\mathbf{k},\mathbf{k}'} = \langle a^{\dagger}_{\mathbf{k}'\uparrow} a^{\dagger}_{-\mathbf{k}\downarrow} \rangle , \tag{3.3}$$

where $\bar{\rho}_{\mathbf{k},\mathbf{k}'} = \rho_{-\mathbf{k},-\mathbf{k}'}$ denotes the time reversed.

The commutation rules of a and $a^{\dagger}$ required in the definition of the EOM of ρ and κ, are easily evaluated if they are expressed in terms of anti-commutators:

$$[AB, CD] = A\{B, C\}D - AC\{B, D\} + \{A, C\}DB - C\{A, D\}B , \tag{3.4}$$

where $A, \ldots, D$, stand for arbitrary operators.

By injecting Eqs. (2.10), (2.22) and (3.3) in Eq. (3.1), we can derive the equations of motion for κ, $\kappa^{\dagger}$, ρ and $\bar{\rho}$:

$$-i\,\dot{\kappa}_{\mathbf{k},\mathbf{k}'} = -(\kappa\bar{h})_{\mathbf{k},\mathbf{k}'} - (h\kappa)_{\mathbf{k},\mathbf{k}'} - (\rho\Delta)_{\mathbf{k},\mathbf{k}'} + \left[\Delta(\mathbb{1} - \bar{\rho})\right]_{\mathbf{k},\mathbf{k}'} , \tag{3.5}$$

$$-i\,(\dot{\kappa}^{\dagger})_{\mathbf{k},\mathbf{k}'} = (\bar{h}\kappa^{\dagger})_{\mathbf{k},\mathbf{k}'} + (\kappa^{\dagger}h)_{\mathbf{k},\mathbf{k}'} + (\Delta^{\dagger}\rho)_{\mathbf{k},\mathbf{k}'} - \left[(\mathbb{1} - \bar{\rho})\Delta^{\dagger}\right]_{\mathbf{k},\mathbf{k}'} , \tag{3.6}$$

$$i\,\dot{\rho}_{\mathbf{k},\mathbf{k}'} = (h\rho)_{\mathbf{k},\mathbf{k}'} - (\rho h)_{\mathbf{k},\mathbf{k}'} - (\Delta\kappa^{\dagger})_{\mathbf{k},\mathbf{k}'} + (\kappa\Delta^{\dagger})_{\mathbf{k},\mathbf{k}'} , \tag{3.7}$$

$$-i\,\dot{\bar{\rho}}_{\mathbf{k},\mathbf{k}'} = (\bar{h}\bar{\rho})_{\mathbf{k},\mathbf{k}'} - (\bar{\rho}\bar{h})_{\mathbf{k},\mathbf{k}'} - (\Delta^{\dagger}\kappa)_{\mathbf{k},\mathbf{k}'} + (\kappa^{\dagger}\Delta)_{\mathbf{k},\mathbf{k}'} . \tag{3.8}$$

The former equations of motion (3.5)–(3.8) describe the variations of the HFB ground state with respect to time. These equations build the general TDHFB equation of motion, and can be expressed in a short-hand form:

$$i\,\dot{\mathscr{R}} = [\mathscr{H}, \mathscr{R}] , \tag{3.9}$$

where $\mathscr{H}$ and $\mathscr{R}$ are the matrices defined below:

$$\mathscr{H} = \begin{pmatrix} h & \Delta \\ \Delta^{\dagger} & -\bar{h} \end{pmatrix} , \tag{3.10}$$

$$\mathscr{R} = \begin{pmatrix} \rho & -\kappa \\ -\kappa^{\dagger} & 1 - \bar{\rho} \end{pmatrix} . \tag{3.11}$$

Here, it is important to mention that the TDHFB equation of motion (3.9) has an opposite sign compared to Eq. (3.1).

3.2 Quasiparticle Random Phase Approximation

The QRPA treats small oscillations around the Hartree-Fock-Bogoliubov (HFB) ground state (which, in the case of uniform matter, is obtained by combining the HF and BCS frameworks discussed in the preceding sections) [Ring and Schuck, 1980]. It can be derived by linearising the time dependent HFB (TDHFB) equations, see, e.g., Ref. [Khan et al., 2002], or, equivalently, by using the formalism of normal and anomalous Green's functions, see, e.g., Refs. [Sedrakian and Keller, 2010, Baldo and Ducoin, 2011]. Here we use the TDHFB formalism.

As mentioned before, the QRPA is the linearization of the TDHFB equations for small oscillations around the ground state. We therefore split the matrices $\mathscr{R}$ and $\mathscr{H}$ into their ground-state values $\mathscr{R}^{(0)}$ and $\mathscr{H}^{(0)}$ and small deviations $\mathscr{R}^{(1)}$ and $\mathscr{H}^{(1)}$:

$$\mathscr{H} = \mathscr{H}^{(0)} + \mathscr{H}^{(1)}, \tag{3.12}$$

$$\mathscr{R} = \mathscr{R}^{(0)} + \mathscr{R}^{(1)}. \tag{3.13}$$

Let us first look at the ground state, which of course has to satisfy Eq. (3.9) with $\dot{\mathscr{R}}^{(0)} = 0$. This is the case because $\mathscr{H}^{(0)}$ and $\mathscr{R}^{(0)}$ can be simultaneously diagonalized. In the ground state, we have $h^{(0)}_{\mathbf{k},\mathbf{k}'} = \bar{h}^{(0)}_{\mathbf{k},\mathbf{k}'} = \xi_{\mathbf{k}}\delta_{\mathbf{k},\mathbf{k}'}$ and $\Delta^{(0)}_{\mathbf{k},\mathbf{k}'} = \Delta^{\dagger(0)}_{\mathbf{k},\mathbf{k}'} = \Delta_{\mathbf{k}}\delta_{\mathbf{k},\mathbf{k}'}$. So, the matrix $\mathscr{H}^{(0)}$ reads as:

$$\mathscr{H}^{(0)} = \begin{pmatrix} \xi & \Delta \\ \Delta & \xi \end{pmatrix}. \tag{3.14}$$

The matrix $\mathscr{H}^{(0)}$ is diagonalized by the transformation

$$\widetilde{\mathscr{H}}^{(0)} = \mathscr{W}^T \mathscr{H}^{(0)} \mathscr{W} = \begin{pmatrix} E & 0 \\ 0 & -E \end{pmatrix}, \tag{3.15}$$

with the eigenvalues $E_{\mathbf{k},\mathbf{k}'} = E_{\mathbf{k}}\,\delta_{\mathbf{k},\mathbf{k}'}$ and the transformation matrix

$$\mathscr{W} = \begin{pmatrix} u & -v \\ v & u \end{pmatrix}, \tag{3.16}$$

where u and v are the usual factors appearing in BCS theory

$$u_{\mathbf{k}} = \sqrt{\frac{1}{2} + \frac{\xi_{\mathbf{k}}}{2E_{\mathbf{k}}}}, \qquad v_{\mathbf{k}} = \sqrt{\frac{1}{2} - \frac{\xi_{\mathbf{k}}}{2E_{\mathbf{k}}}}. \tag{3.17}$$

The normal and anomalous density matrices in the ground state are given by $\rho^{(0)}_{\mathbf{k},\mathbf{k}'} = \bar{\rho}^{(0)}_{\mathbf{k},\mathbf{k}'} = v^2_{\mathbf{k}}\delta_{\mathbf{k},\mathbf{k}'}$ and $\kappa^{(0)}_{\mathbf{k},\mathbf{k}'} = \kappa^{\dagger(0)}_{\mathbf{k},\mathbf{k}'} = u_{\mathbf{k}}v_{\mathbf{k}}\delta_{\mathbf{k},\mathbf{k}'}$, so that the same transformation diagonalizes $\mathscr{R}^{(0)}$, too:

$$\widetilde{\mathscr{R}}^{(0)} = \mathscr{W}^T\mathscr{R}^{(0)}\mathscr{W} = \begin{pmatrix} 0 & 0 \\ 0 & 1 \end{pmatrix}. \tag{3.18}$$

Let us now consider a small perturbation of the system. By keeping in Eq. (3.9) only the first order in the deviations, we obtain the linearized equation of motion

$$i\dot{\mathscr{R}}^{(1)} = [\mathscr{H}^{(0)},\mathscr{R}^{(1)}] + [\mathscr{H}^{(1)},\mathscr{R}^{(0)}]. \tag{3.19}$$

The equation can be simplified by applying again the transformation that diagonalizes $\mathscr{H}^{(0)}$ and $\mathscr{R}^{(0)}$. After a Fourier transform with respect to time one obtains the following equation:

$$\omega\widetilde{\mathscr{R}}^{(1)} = \begin{pmatrix} [E,\widetilde{\mathscr{R}}^{(1)}_{11}] & \{E,\widetilde{\mathscr{R}}^{(1)}_{12}\} + \widetilde{\mathscr{H}}^{(1)}_{12} \\ -\{E,\widetilde{\mathscr{R}}^{(1)}_{21}\} - \widetilde{\mathscr{H}}^{(1)}_{21} & -[E,\widetilde{\mathscr{R}}^{(1)}_{22}] \end{pmatrix}. \tag{3.20}$$

From the former matrix one can easily determine the non-vanishing elements:

$$(\omega - E_{\mathbf{k}} + E_{\mathbf{k}'})\widetilde{\mathscr{R}}^{(1)}_{11,\mathbf{k}\mathbf{k}'} = 0, \tag{3.21}$$

$$(\omega - E_{\mathbf{k}} - E_{\mathbf{k}'})\widetilde{\mathscr{R}}^{(1)}_{12,\mathbf{k}\mathbf{k}'} = -\widetilde{\mathscr{H}}^{(1)}_{12,\mathbf{k}\mathbf{k}'}, \tag{3.22}$$

$$(\omega - E_{\mathbf{k}} + E_{\mathbf{k}'})\widetilde{\mathscr{R}}^{(1)}_{21,\mathbf{k}\mathbf{k}'} = \widetilde{\mathscr{H}}^{(1)}_{21,\mathbf{k}\mathbf{k}'}, \tag{3.23}$$

$$(\omega - E_{\mathbf{k}} - E_{\mathbf{k}'})\widetilde{\mathscr{R}}^{(1)}_{22,\mathbf{k}\mathbf{k}'} = 0. \tag{3.24}$$

The matrix $\mathscr{R}^{(1)}$ is then obtained by transforming $\widetilde{\mathscr{R}}^{(1)}$ back. The resulting expressions are lengthy, but they can be simplified by using the following linear combinations:

$$\rho^{\pm} = \rho \pm \bar{\rho}, \qquad \kappa^{\pm} = \kappa \pm \kappa^{\dagger}, \tag{3.25}$$

$$h^{\pm} = h \pm \bar{h}, \qquad \Delta^{\pm} = \Delta \pm \Delta^{\dagger}. \tag{3.26}$$

In the case of spin-independent excitations studied here, ρ^+ is responsible for density oscillations, while ρ^- describes the corresponding current. (In the case of spin modes, the situation would be reversed.) The quantities κ^+ and Δ^+ are related to oscillations of the amplitude of Δ, while κ^- and Δ^- describe phase oscillations which are extremely important in the context of the low-energy collective mode (Goldstone mode). The solution for $\rho^{\pm(1)}$ and $\kappa^{\pm(1)}$ can be written in the form

$$\begin{pmatrix} \rho^{+(1)}_{\mathbf{k}_1,\mathbf{k}_2} \\ \rho^{-(1)}_{\mathbf{k}_1,\mathbf{k}_2} \\ \kappa^{+(1)}_{\mathbf{k}_1,\mathbf{k}_2} \\ \kappa^{-(1)}_{\mathbf{k}_1,\mathbf{k}_2} \end{pmatrix} = \Pi^{(0)}_{\mathbf{k}_1,\mathbf{k}_2}(\omega) \begin{pmatrix} h^{+(1)}_{\mathbf{k}_1,\mathbf{k}_2} \\ h^{-(1)}_{\mathbf{k}_1,\mathbf{k}_2} \\ \Delta^{+(1)}_{\mathbf{k}_1,\mathbf{k}_2} \\ \Delta^{-(1)}_{\mathbf{k}_1,\mathbf{k}_2} \end{pmatrix} \tag{3.27}$$

where $\Pi^{(0)}_{\mathbf{k}_1,\mathbf{k}_2}(\omega)$ is a 4×4 matrix whose components denoted by $\Pi^{\rho^+,h^+}_{\mathbf{k}_1,\mathbf{k}_2}, \ldots, \Pi^{\kappa^-,\Delta^-}_{\mathbf{k}_1,\mathbf{k}_2}$ are given in Appendix B.

So far, we have not specified the perturbation of the hamiltonian, $h^{(1)}$. There are two contributions of different origin. First, to probe the system, we apply an external perturbation at $t = 0$ of the form of a plane wave, i.e., $V_{\text{ex}} e^{i\mathbf{q}\cdot\mathbf{r}}\delta(t)$, which after Fourier transformation becomes $V_{\text{ex}}\delta_{\mathbf{k}_1-\mathbf{k}_2,\mathbf{q}}$. The second contribution to $h^{(1)}$ comes from the oscillations of the mean field due to the density oscillations :

$$h^{(1)}_{\mathbf{k}_1,\mathbf{k}_2} = V_{\text{ex}}\delta_{\mathbf{k}_1-\mathbf{k}_2,\mathbf{q}} + \sum_{\mathbf{k}_3,\mathbf{k}_4} V^{\text{ph}}_{\mathbf{k}_1,\mathbf{k}_2,\mathbf{k}_4,\mathbf{k}_3}\,\rho^{(1)}_{\mathbf{k}_3,\mathbf{k}_4}\,. \tag{3.28}$$

Analogously, the oscillation of the gap, $\Delta^{(1)}$, is related to the oscillation of the anomalous density,

$$\Delta^{(1)}_{\mathbf{k}_1,\mathbf{k}_2} = -\sum_{\mathbf{k}_3,\mathbf{k}_4} V^{\text{pp}}_{\mathbf{k}_1,\mathbf{k}_2,\mathbf{k}_4,\mathbf{k}_3}\,\kappa^{(1)}_{\mathbf{k}_3,\mathbf{k}_4}\,. \tag{3.29}$$

Looking at Eq. (3.27) and taking into account the momentum conservation in the interactions V^{ph} and V^{pp}, one sees that an external perturbation proportional to $\delta_{\mathbf{k}_1-\mathbf{k}_2,\mathbf{q}}$ leads to non-vanishing elements of $\rho_{\mathbf{k}_1,\mathbf{k}_2}$ and $\kappa_{\mathbf{k}_1,\mathbf{k}_2}$ only for $\mathbf{k}_1 - \mathbf{k}_2 = \mathbf{q}$. This could have been anticipated, since in a uniform system a perturbation having the form of a plane wave can only excite oscillations which are also plane waves with the same wave vector as the perturbation. We therefore introduce the short-hand notation $\mathbf{k}_\pm = \mathbf{k} \pm \frac{\mathbf{q}}{2}$ and denote the non-vanishing matrix elements by $\rho_{\mathbf{k}_+,\mathbf{k}_-}$, etc.

The advantage of the Skyrme functional is that $h^{(1)}$ depends only on local quantities. With the notation of Eq. (2.15), we have

$$h^{+(1)}_{\mathbf{k}_+,\mathbf{k}_-} = W_1(q)\,\rho^{+(1)}_{\mathbf{q}} + W_2 k^2\,\rho^{+(1)}_{\mathbf{q}} + W_2\,\tau^{+(1)}_{\mathbf{q}} + 2V_{\text{ex}}\,, \tag{3.30a}$$

$$h^{-(1)}_{\mathbf{k}_+,\mathbf{k}_-} = 2W_2 k\cos\theta\, j^{-(1)}_{\mathbf{q}}\,, \tag{3.30b}$$

where θ is the angle between $\mathbf{k}$ and $\mathbf{q}$ and

$$\rho^{+(1)}_{\mathbf{q}} = \sum_{\mathbf{k}} \rho^{+(1)}_{\mathbf{k}_+,\mathbf{k}_-}\,, \tag{3.31a}$$

$$\tau_{\mathbf{q}}^{+(1)} = \sum_{\mathbf{k}} k^2 \rho_{\mathbf{k}_+,\mathbf{k}_-}^{+(1)}, \tag{3.31b}$$

$$j_{\mathbf{q}}^{-(1)} = \sum_{\mathbf{k}} k \cos\theta \, \rho_{\mathbf{k}_+,\mathbf{k}_-}^{-(1)}. \tag{3.31c}$$

Similarly, in the pp channel, the calculation is simplified by the fact that our pairing interaction (2.36) is separable:

$$\Delta_{\mathbf{k}_+,\mathbf{k}_-}^{\pm(1)} = gF(k)\kappa_{\mathbf{q}}^{\pm(1)} \tag{3.32}$$

with

$$\kappa_{\mathbf{q}}^{\pm(1)} = \sum_{\mathbf{k}} F(k)\kappa_{\mathbf{k}_+,\mathbf{k}_-}^{\pm(1)} \tag{3.33}$$

Now we are able to calculate the linear response by inserting Eqs. (3.27), (3.30) and (3.32) into Eqs. (3.31) and (3.33). In this way we obtain

$$\begin{pmatrix} \rho_{\mathbf{q}}^{+(1)} \\ \tau_{\mathbf{q}}^{+(1)} \\ j_{\mathbf{q}}^{-(1)} \\ \kappa_{\mathbf{q}}^{+(1)} \\ \kappa_{\mathbf{q}}^{-(1)} \end{pmatrix} = \left(\mathbb{1} - \langle\langle \Pi_{\mathbf{q}}^{(0)} V \rangle\rangle\right)^{-1} \begin{pmatrix} \langle\langle \Pi_{\mathbf{k}_+,\mathbf{k}_-}^{\rho+,h+} \rangle\rangle \\ \langle\langle k^2 \, \Pi_{\mathbf{k}_+,\mathbf{k}_-}^{\rho^+,h^+} \rangle\rangle \\ \langle\langle k \cos\theta \, \Pi_{\mathbf{k}_+,\mathbf{k}_-}^{\rho^-,h^+} \rangle\rangle \\ \langle\langle F(k) \Pi_{\mathbf{k}_+,\mathbf{k}_-}^{\kappa^+,h^+} \rangle\rangle \\ \langle\langle F(k) \Pi_{\mathbf{k}_+,\mathbf{k}_-}^{\kappa^-,h^+} \rangle\rangle \end{pmatrix} 2V_{\mathrm{ex}}, \tag{3.34}$$

where the short-hand notation $\langle\langle f(\mathbf{k}) \rangle\rangle$ denotes the sum of $f(\mathbf{k})$ over $\mathbf{k}$,

$$\langle\langle f(\mathbf{k}) \rangle\rangle = \sum_{\mathbf{k}} f(\mathbf{k}), \tag{3.35}$$

and the matrix $\langle\langle \Pi_{\mathbf{q}}^{(0)} V \rangle\rangle$ is given in Appendix B.

It is well known that superfluidity leads to the existence of the so-called Bogoliubov-Anderson sound [Bogoliubov et al., 1959, Anderson, 1958], a collective mode with linear dispersion relation $\omega \propto q$ (for small q) which can be interpreted as a Goldstone boson corresponding to the broken U(1) symmetry [Weinberg, 2005]. This implies that the QRPA response function has a pole at low energy. The energy ω of this collective mode can be found by searching for a given q the root of the determinant of the matrix appearing in Eq. (3.34):

$$\left| \mathbb{1} - \langle\langle \Pi_{\mathbf{q}}^{(0)} V \rangle\rangle \right| = 0. \tag{3.36}$$

This collective mode exists only at low momentum q, as long as its energy ω lies below the pair-breaking threshold $\sim 2\Delta_{k_F}$, where k_F denotes the Fermi momentum. At higher values of q, the collective mode enters the two-quasiparticle continuum and gets a width (finite lifetime).

3.3 Landau approximation

In some recent work [Baldo and Ducoin, 2011, Keller and Sedrakian, 2013], the QRPA response was calculated within the Landau approximation [Nozières, 1964]. In this approximation, one exploits the fact that for small q the change of the density matrix $\rho_{\mathbf{k},\mathbf{k}'}$ is concentrated at the Fermi surface, $|\mathbf{k}| \approx |\mathbf{k}'| \approx k_F$. Keeping only the Landau parameter F_0 amounts to replacing Eq. (3.30) by

$$h^{+(1)}_{\mathbf{k}_+,\mathbf{k}_-} = (W_1(0) + 2W_2 k_F^2)\rho^{+(1)}_{\mathbf{q}} \tag{3.37}$$

and neglecting $h^{-(1)}_{\mathbf{k}_+,\mathbf{k}_-}$. However, because of the effective mass $m^* \neq m$, this approximation violates Galilean invariance [Nozières, 1964] and one should also include the parameter F_1. In this case one has

$$h^{-(1)}_{\mathbf{k}_+,\mathbf{k}_-} = 2W_2 k_F \cos\theta \, j^{-(1)}_{\mathbf{q}} , \tag{3.38}$$

where the current $j^{-(1)}_{\mathbf{q}}$ (3.31c) is simplified to

$$j^{-(1)}_{\mathbf{q}} = k_F \sum_{\mathbf{k}} \cos\theta \, \rho^{-(1)}_{\mathbf{k}_+,\mathbf{k}_-} . \tag{3.39}$$

As a consequence, the 5 × 5 matrix in Eq. (3.34) reduces to a 3 × 3 or 4 × 4 one if one keeps only F_0 or F_0 and F_1, respectively.

3.4 Long wavelength limit

3.4.1 Derivation from QRPA

The broken symmetry U(1) of the pairing field Δ yields a collective mode of zero-energy (Goldstone mechanism). Considering the QRPA equations within the limit of excitations of small momentum $\mathbf{q}$ and energy ω, one expects to find the Bogoliubov-Anderson mode. As in Bogoliubov [Bogoliubov et al., 1959] and Anderson [Anderson, 1958] we start by considering an ideal Fermi-gas. In this limit one neglects V^{ph} in the perturbed Hamiltonian, so that $h^{+(1)}_{\mathbf{k},\mathbf{k}'}$ reads as:

$$h^{+(1)}_{\mathbf{k},\mathbf{k}'} = V_{\mathrm{ex}} \delta_{\mathbf{k}+\mathbf{q},\mathbf{k}'} . \tag{3.40}$$

In the gap equation (2.21), the anomalous density κ can be expressed as a function of the QRPA response functions (3.34). Thus, one has for the gap equation:

$$\Delta^{-(1)}_{\mathbf{k},\mathbf{k}'} = F(\tfrac{1}{2}|\mathbf{k}+\mathbf{k}'|) \sum_{\mathbf{k}_1,\mathbf{k}_2} gF(\tfrac{1}{2}|\mathbf{k}_1+\mathbf{k}_2|) \left[\Pi^{\kappa_-,\Delta_-}_{\mathbf{k}_1,\mathbf{k}_2} \Delta^{-(1)}_{\mathbf{k}_1,\mathbf{k}_2} + \Pi^{\kappa_-,h_+}_{\mathbf{k}_1,\mathbf{k}_2} h^{+(1)}_{\mathbf{k}_1,\mathbf{k}_2}\right] \times \delta_{\mathbf{k}_2-\mathbf{k}_1,\mathbf{k}'-\mathbf{k}} . \quad (3.41)$$

The former expression of $\Delta^{-(1)}_{\mathbf{k},\mathbf{k}'}$ can be reduced because of the momentum conservation. In addition, by making use of Eq. (3.40) and performing the summation over $\mathbf{k}_1$, the perturbation of the gap reads as:

$$\Delta^{-(1)}_{\mathbf{k},\mathbf{k}'} = F(\tfrac{1}{2}|2\mathbf{k}-\mathbf{q}|)\,\tilde{\Delta}^{-(1)}_{\mathbf{q}}\delta_{\mathbf{k}'-\mathbf{k},\mathbf{q}} . \quad (3.42)$$

The term $\tilde{\Delta}^{-(1)}_{\mathbf{q}}$ is defined self-consistently and satisfies:

$$\tilde{\Delta}^{-(1)}_{\mathbf{q}} \left[1 - \sum_{\mathbf{k}} gF^2(\tfrac{1}{2}|2\mathbf{k}-\mathbf{q}|)\Pi^{\kappa_-,\Delta_-}_{\mathbf{k}-\mathbf{q},\mathbf{k}}\right] = \sum_{\mathbf{k}} gF(\tfrac{1}{2}|2\mathbf{k}-\mathbf{q}|)\Pi^{\kappa_-,h_+}_{\mathbf{k}-\mathbf{q},\mathbf{k}} V_{\text{ex}} . \quad (3.43)$$

The collective mode of the neutron gas is described by the pole of $\Delta^{-(1)}_{\mathbf{k}\mathbf{k}'}$. However, one sees clearly that the pole of the gap equation is fully contained in the expression of $\tilde{\Delta}^{-(1)}_{\mathbf{q}}$. The analytical solution of the collective mode can be obtained thanks to the expansion of the response function $\Pi^{\kappa_-,\Delta_-}_{\mathbf{k}-\mathbf{q},\mathbf{k}}$ for small $\mathbf{q}$ and ω, thus one has:

$$1 - \sum_{\mathbf{k}} gF^2(k)\frac{1}{2E_{\mathbf{k}}} - \sum_{\mathbf{k}} gF^2(k)\left[\frac{1}{8E^3_{\mathbf{k}}}\omega^2 + \frac{1}{8E^3_{\mathbf{k}}}\left(1-3\frac{\Delta^2_{\mathbf{k}}}{E^2_{\mathbf{k}}}\right)(\mathbf{v}_{\mathbf{k}}\cdot\mathbf{q})^2 + \frac{\xi_{\mathbf{k}}}{E^3_{\mathbf{k}}}\frac{q^2}{m}\right] = 0 \quad (3.44)$$

where $\mathbf{v}_{\mathbf{k}} = \mathbf{k}/m$ is the velocity associated with the momentum $\mathbf{k}$. The summation can be simplified if one exploits that the major contribution of the form factor and the gap energy are located at the Fermi surface, because the factors $1/E_{\mathbf{k}}$ and $1/E^3_{\mathbf{k}}$ are strongly peaked at $|\mathbf{k}| = k_F$. Hence we replace $F(k)$ and $\Delta_{\mathbf{k}}$ by $F(k_F)$ and $\Delta_{\mathbf{k}_F} \equiv \Delta$, respectively. On the first line of Eq. (3.44) a major simplification can be performed by identifying it with the gap equation (2.34).

In the limit of low momentum excitations ($\mathbf{q} \to 0$), it becomes more convenient to integrate Eq. (3.44) over $\xi = \mathbf{k}^2/2m - \mu$. Hence, Eq. (3.44) reduces to:

$$N(0)\omega^2\frac{gF^2(k_F)}{8}\int d\xi\,\frac{1}{E^3} + N(0)\frac{gF^2(k_F)}{8}\frac{\mathbf{v}_F^2\mathbf{q}^2}{3}\int d\xi\,\frac{1}{E^3}\left(1-3\frac{\Delta^2}{E^2}\right) = 0 , \quad (3.45)$$

where density of states has been replaced by its value at the Fermi surface

$$N(0) = \int \frac{d^3k}{(2\pi)^3}\,\delta(\xi_{\mathbf{k}}) = \frac{mk_F}{2\pi^2}\,. \tag{3.46}$$

In Eq. (3.45), the isotropy of the Fermi velocity $\mathbf{v}_F$ is responsible for the factor one-third. A further approximation consists in replacing the lower integration limit $-\mu$ by $-\infty$. Actually, the contribution is concentrated at the Fermi surface ($\xi \approx 0$). By performing the integration over ξ, the (odd) term ξ/E cancels.

The integral of Δ^2/E^3 is non-trivial, so that a hint is to express it in terms of ξ derivatives

$$\frac{\mathrm{d}}{\mathrm{d}\xi}\left(\frac{\xi}{E^3}\right) = -\frac{2}{E^3} + 3\frac{\Delta^2}{E^5}\,. \tag{3.47}$$

Finally, by inserting the preceding results into Eq. (3.45), one has

$$\omega^2 \int \mathrm{d}\xi\,\frac{1}{E^3} - \frac{\mathbf{v}_F^2\mathbf{q}^2}{3}\int \mathrm{d}\xi\,\frac{1}{E^3} = 0\,. \tag{3.48}$$

From the previous expression, one sees immediately the dispersion relation of the Bogoliubov-Anderson sound [Bogoliubov et al., 1959, Anderson, 1958]:

$$\omega = \frac{v_F\,q}{\sqrt{3}}\,. \tag{3.49}$$

This result is valid in an ideal Fermi gas, and was generalized by Leggett [Leggett, 1966] to an interacting Fermi gas in the framework of Landau's Fermi-liquid theory.

3.4.2 Derivation from superfluid hydrodynamics

In the limit of zero temperature, the superfluid hydrodynamics equations describe the superfluid flow. (Otherwise the normal component has to be included, two-fluids hydrodynamics [Leggett, 1966]). Thanks to this major simplification we expect to find the dispersion relation of the Bogoliubov-Anderson [Bogoliubov et al., 1959, Anderson, 1958] sound. First, we consider the standard equations for an ideal (inviscid) flow

$$\frac{\partial\rho}{\partial t} + \nabla(\rho\mathbf{v}) = 0\,, \tag{3.50}$$

$$m\frac{\partial\mathbf{v}}{\partial t} + \nabla\cdot\left(\frac{1}{2}m\mathbf{v}^2 + \mu\right) = 0\,, \tag{3.51}$$

with the continuity and the Euler equation, respectively. The density of the fluid is denoted by $\rho = k_F^3/(3\pi^2)$ and its velocity by $\mathbf{v}$. The Bogoliubov-Anderson mode corresponds to a small amplitude excitation. Therefore, the chemical potential of the superfluid μ can be linearized around its equilibrium ($\rho = \rho_0$):

$$\mu(\rho) = \mu(\rho_0) + \left.\frac{\partial \mu}{\partial \rho}\right|_{\rho=\rho_0} (\rho - \rho_0) . \tag{3.52}$$

By injecting the linearized expression of μ into the Euler equation one finds:

$$m\frac{\partial \mathbf{v}}{\partial t} + \frac{\partial \mu}{\partial \rho} \nabla \rho = 0 , \tag{3.53}$$

Now, we focus on the continuity equation (3.50). We only keep the dominant term $\rho \nabla \cdot \mathbf{v}$ provided by the gradient $\nabla(\rho \mathbf{v})$. Hence, thanks to the simplifications detailed above, one can find the sound propagation equation. This is done by injecting the simplified Euler equation (3.53) in the continuity equation (3.50) derived with respect to the time, which leads to wave equation

$$\frac{\partial^2 \rho}{\partial t^2} - \frac{\rho}{m}\frac{\partial \mu}{\partial \rho} \nabla^2 \rho = 0 , \tag{3.54}$$

with the sound velocity u given by:

$$u^2 = \frac{\rho}{m}\frac{\partial \mu}{\partial \rho} . \tag{3.55}$$

We consider that the pairing does not affect the density of the system, so that the chemical potential is close to $\mu \simeq \epsilon_F$ the Fermi energy. In this approximation, the gradient of the chemical potential simply reads as:

$$\frac{\partial \mu}{\partial \rho} = \frac{2}{3}\frac{\rho}{\mu} . \tag{3.56}$$

Finally we recover the result of the previous section:

$$\omega^2 = \frac{k_F^2}{3m^2} q^2 = \left(\frac{\mathbf{v}_F}{\sqrt{3}} q\right)^2 , \tag{3.57}$$

if one knows that $u = \omega/q$ with the collective mode energy ω as a function of q the excitation momentum.

At a first glance, it is surprising that hydrodynamics is applicable here. In a normal fluid, hydrodynamics requires collisions that restore local equilibrium. Otherwise, in the collisionless regime, the local Fermi sphere gets deformed during the oscillation, which gives rise to the so-called zero-sound modes [Nozières, 1964]. The situation is completely different in a superfluid at $T = 0$: although there are no collisions, the local Fermi sphere stays spherical during the oscillation because of pairing. This "superfluid hydrodynamics" was also used to describe collective modes in trapped (i.e., non-uniform) Fermi gases [Menotti et al., 2002], and in Ref. [Grasso et al., 2005] it was demonstrated that also in that case hydrodynamic and QRPA results for $T = 0$ agree if pairing is strong enough.

In order to calculate the hydrodynamic speed of sound of the interacting system, we use in Eq. (3.52) the chemical potential obtained with the Skyrme functional (with pairing). Let us remind that $dP = \rho\, d\mu$, with P the pressure, so that Eq. (3.55) reads as:

$$u^2 = \frac{1}{m}\frac{\partial P}{\partial \rho}. \tag{3.58}$$

3.5 Numerical computation

In Appendix B we give the equations needed to determine the QRPA response function. In practice, the summations over $\mathbf{k}$ are integrals. In our numerical calculations we start by evaluating numerically the imaginary parts of the matrix $\langle\langle \Pi^{(0)}_{\mathbf{q}} V\rangle\rangle$. According to Eqs. (B.1) and (B.3), each element of this matrix can be written in the form

$$\langle\langle \Pi^{(0)}_{\mathbf{q}}(\omega) V\rangle\rangle_{\alpha\beta} = \int \frac{d^3k}{(2\pi)^3} f_{\alpha\beta}(k,q,z) G^{\pm}_{\mathbf{k},\mathbf{q}}(\omega). \tag{3.59}$$

Then the the imaginary part is given by :

$$\mathrm{Im}\langle\langle \Pi^{(0)}_{\mathbf{q}}(\omega) V\rangle\rangle = \frac{1}{2\pi^2}\int_0^{z_{\max}} dz \sum_i \frac{k_i^2 f(k_i,q,z)}{\left|\frac{\partial \Omega_{\mathbf{k},\mathbf{q}}}{\partial k}\right|_{k_i}}, \tag{3.60}$$

where $\{k_i\}$ is the set of solutions of the equation $\Omega_{\mathbf{k},\mathbf{q}} = \omega$ for a given angle z, and $z_{\max}$ is either 1 or the angle beyond which the equation $\Omega_{\mathbf{k},\mathbf{q}} = \omega$ does not have a solution any more. The form of the function $\Omega_{\mathbf{k},\mathbf{q}}$ is illustrated in Figure 3.1 for a fixed density and different values of z. It is important to notice that the minimum of $\Omega_{\mathbf{k},\mathbf{q}}$ is not located exactly at $k = k_F$, with the Fermi momentum $k_F = (3\pi^2\rho)^{1/3}$. The minimum is shifted because of a strong pairing gap, which affects the relation between ρ and the chemical potential μ^*, in consequence $k_F \neq \sqrt{2m^*\mu^*}$.

After the calculation of the imaginary part, we compute the real part with the help of a dispersion relation,

$$\mathrm{Re}\langle\langle \Pi^{(0)}_{\mathbf{q}}(\omega) V\rangle\rangle = -\frac{1}{\pi}\,\mathrm{P}\int_0^{\infty} d\omega'\, \mathrm{Im}\langle\langle \Pi^{(0)}_{\mathbf{q}}(\omega') V\rangle\rangle \left(\frac{1}{\omega-\omega'} \pm \frac{1}{\omega+\omega'}\right), \tag{3.61}$$

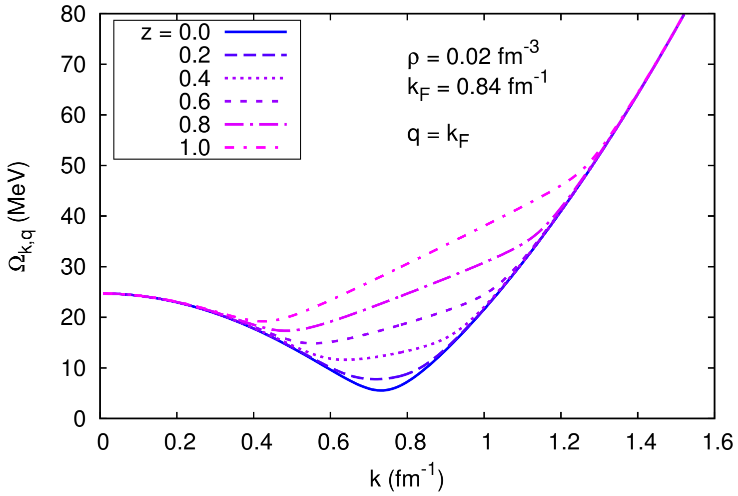

Figure 3.1: The form of $\Omega_{\mathbf{k},\mathbf{q}} = E_{\mathbf{k}+} + E_{\mathbf{k}-}$ for a fixed neutron gas density of $\rho = 0.02$ fm^{-3}. The figure displays the evolution of $\Omega_{\mathbf{k},\mathbf{q}}$ for different values of $z = \cos\theta$, with θ the angle between $\mathbf{k}$ and $\mathbf{q}$.

where the sign ± is chosen according to the sign in $G^{\pm}$ in Eq. (3.59). In the last integral we note that it presents a pole for $\omega - \omega' = 0$. In order to evaluate the principal value numerically, the real part of the integral can be expressed as:

$$\mathrm{Re}\langle\langle\Pi^{(0)}_{\mathbf{q}}(\omega)V\rangle\rangle = -\frac{1}{\pi}\left[\int_0^{\infty} \mathrm{d}\omega' \frac{\mathrm{Im}\langle\langle\Pi^{(0)}_{\mathbf{q}}(\omega')V\rangle\rangle - \mathrm{Im}\langle\langle\Pi^{(0)}_{\mathbf{q}}(\omega)V\rangle\rangle}{\omega-\omega'} + \int_0^{\infty} \mathrm{d}\omega' \frac{\mathrm{Im}\langle\langle\Pi^{(0)}_{\mathbf{q}}(\omega)V\rangle\rangle}{\omega-\omega'}\right], \quad (3.62)$$

with the first term being well behaved for $\omega = \omega'$ and the second one analytically solvable. The integration does not run up to infinity, we suppose a cut-off Λ above which the imaginary part is not supposed to contribute anymore. Thus one has to evaluate numerically the following integral:

$$\mathrm{Re}\langle\langle\Pi^{(0)}_{\mathbf{q}}(\omega)V\rangle\rangle = -\frac{1}{\pi}\left[\int_0^{\Lambda} \mathrm{d}\omega' \frac{\mathrm{Im}\langle\langle\Pi^{(0)}_{\mathbf{q}}(\omega')V\rangle\rangle - \mathrm{Im}\langle\langle\Pi^{(0)}_{\mathbf{q}}(\omega)V\rangle\rangle}{\omega-\omega'} \pm \int_0^{\Lambda} \mathrm{d}\omega' \frac{\mathrm{Im}\langle\langle\Pi^{(0)}_{\mathbf{q}}(\omega')V\rangle\rangle}{\omega+\omega'} + \mathrm{Im}\langle\langle\Pi^{(0)}_{\mathbf{q}}(\omega)V\rangle\rangle \ln\left|\frac{\omega}{\omega-\Lambda}\right|\right], \quad (3.63)$$

with ± chosen according to the sign of the Green's functions $G^{\pm}$.

Chapter 4

Results uniform neutron matter

In this chapter we focus on the collective modes in the uniform neutron matter. These calculation are made thanks to the formalisms developed in the preceding Chapters 2 and 3. This chapter is essentially based on Ref. [Martin and Urban, 2014].

4.1 Ground state

Before we turn to the linear response, let us briefly discuss the ground state properties. For the mean field, we use the SLy4 parametrization of the Skyrme force, whose parameters are given in Ref. [Chabanat et al., 1998]. This interaction was not only fitted to nuclei, but also to the Equation of State (EOS) of neutron matter. Since pairing has only a marginal effect on the EOS, our EOS agrees with that shown, e.g., in Ref. [Douchin and Haensel, 2000].

To determine the two parameters g and k_0 of our pairing interaction, Eqs. (2.36) and (2.37), we first solve the gap equation (2.34) with the (non-separable) $V_{\text{low-}k}$ interaction[1]. The resulting gap at the Fermi surface, Δ_{k_F}, as a function of $k_F = (3\pi^2\rho)^{1/3}$, is displayed in Fig. 4.1 (dashes). Then we fit g and k_0 to reproduce this result with the separable interaction. The result of this fit is also shown in Fig. 4.1 (solid line), and the corresponding parameter values are listed in Table 4.1. We see that with this pairing interaction, the maximum of the gap, $\Delta_{k_F} \sim 2.7$ MeV, is reached at $k_F \sim 0.8$ fm^{-1}, corresponding to a density of $\rho \sim 0.017$ fm^{-3}. At low density, the gap increases with density because of the increasing level density at the Fermi surface. The decrease of the gap at high density is due to the form factor, Eq. (2.37),

---

[1] The matrix elements used here are those obtained in Ref. [Bogner et al., 2007] with a Fermi-Dirac regulator with $\Lambda = 2$ fm^{-1} and $\epsilon = 0.5$ fm^{-1}.

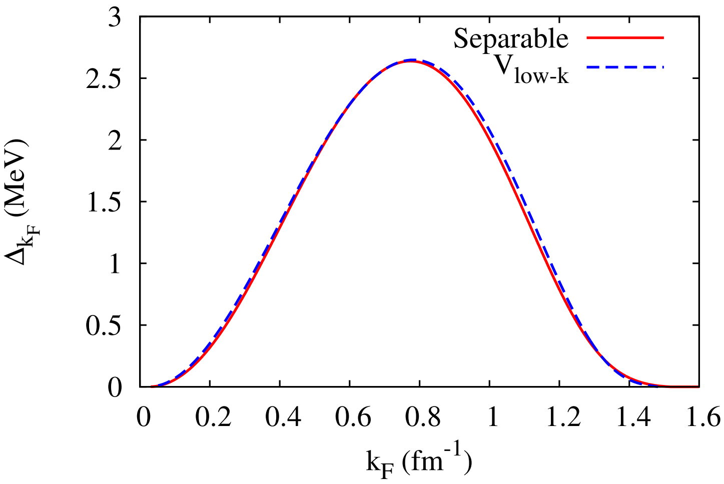

Figure 4.1: Value of the gap at the Fermi surface, Δ_{k_F}, as function of the Fermi momentum k_F, obtained with the separable interaction (solid line) and with the $V_{\text{low-}k}$ interaction of [Bogner et al., 2007] (dashes).

Table 4.1: Parameters of the pairing interaction, Eqs. (2.36) and (2.37).

g (MeV fm^3)	853
k_0 (fm^{-1})	2.73

and not due to an explicit density dependence of the pairing interaction as it is often used in HFB and QRPA calculations with Skyrme forces (see, e.g., Ref. [Khan et al., 2002]). The fact that our maximum gap is reduced by $\sim 10\%$ compared to typical BCS results obtained with the free nucleon mass [Hebeler et al., 2007] is a consequence of the reduction of the density of states due to the effective mass $m^* < m$.

However, it should be pointed out that there is no consensus in the literature about the correct density dependence of the gap [Dean and Hjorth-Jensen, 2003, Chamel and Haensel, 2008], mainly because of screening effects beyond BCS theory (analogous to the Gorkov–Melik-Barkhudarov correction [Gor'kov and Melik-Barkhudarov, 1961]), which could lead to a dramatic suppression of the gap. At low density, recent Quantum-Monte-Carlo calculations [Gezerlis and Carlson, 2008, Gezerlis and Carlson, 2010] seem to be reliable and show a suppression of the gap between 30 and 50% compared to the BCS result (discussed and illustrated in the preceding Chapter 3).

4.2 QRPA response function and collective mode

We will now study the QRPA response function in neutron matter for different densities and compare it with the RPA one. In the present work we consider the density response, which is defined by $\Pi(\omega, q) = \rho_{\mathbf{q}}^{+(1)}/(2V_{\text{ex}})$. Since its real and imaginary parts are related to each other via dispersion relations, it is enough to discuss the imaginary part, the so-called strength function.

We choose densities between 0.016 and 0.04 fm^{-3}, corresponding to typical densities of the neutron gas surrounding the clusters in the inner crust of a neutron star [Negele and Vautherin, 1973]. At higher densities, as they are realized in the neutron star core, our approach is not valid because there the neutrons are paired in the $^3P_2$ channel [Tamagaki, 1970]. As we have seen in the preceding subsection, the $^1S_0$ gap decreases with increasing density. We therefore expect that at high density, our QRPA response approaches the RPA one. The latter is the response calculated without pairing, i.e., by setting $\Delta_{\mathbf{k}} = 0$ and keeping only the upper left 3×3 part of the matrix in Eq. (3.34), and we checked that it coincides with the RPA response functions that can be found in the literature [García-Recio et al., 1992]. As one can see in Fig. 4.2, where the strength function is shown for $\rho = 0.04$ fm^{-3}, the RPA (dashes) and QRPA (solid lines) responses are indeed similar and

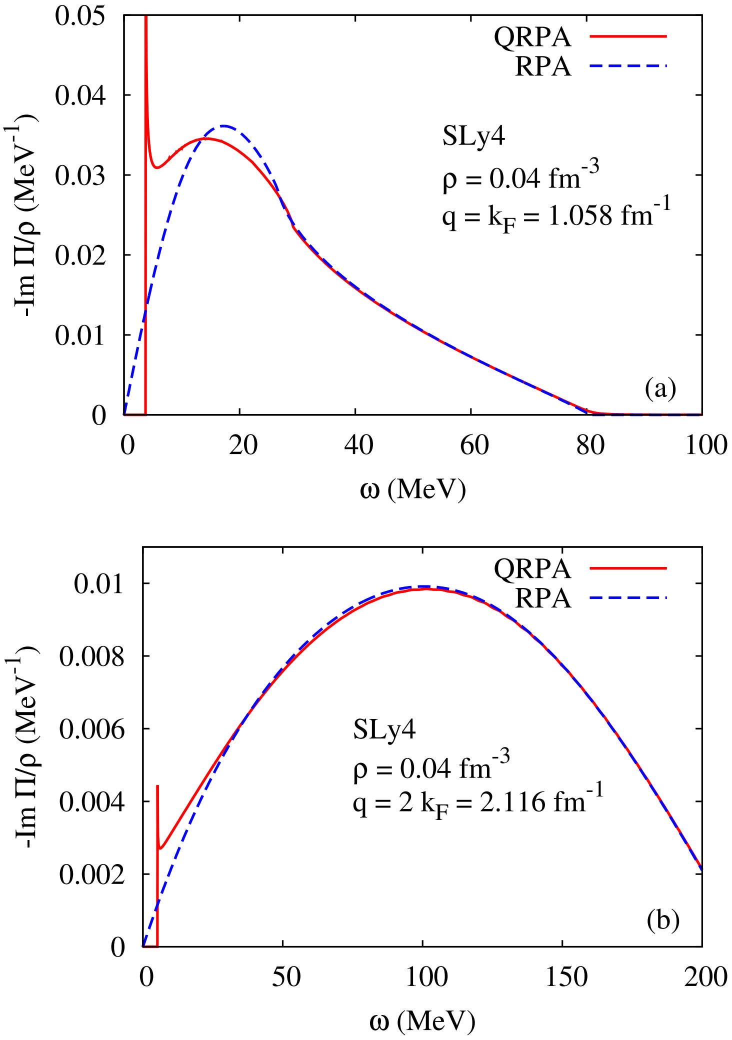

Figure 4.2: QRPA (solid lines) and RPA (dashes) response functions at density $\rho = 0.04$ fm^{-3}, as functions of the excitation energy ω for two different momentum transfers $q = k_F$ (a) and $2k_F$ (b).

approach each other with increasing excitation energy ω and momentum transfer q. For $q = k_F$ (upper panel) and $2k_F$ (lower panel), the RPA strength function has a broad continuum. The effect of pairing is to shift the threshold of the continuum from zero to the pair-breaking threshold $\sim 2\Delta_{k_F}$. At excitation energies much larger than $2\Delta_{k_F}$, the response is practically not affected by pairing. At energies around the threshold, however, the response is strongly modified by pairing. The peak visible at the threshold corresponds to a collective mode which is damped since it lies in the continuum, i.e., it can decay into two quasiparticles. In RPA, one does not see any collective mode, since the ph interaction is attractive and a collective zero-sound mode, as it can be described by RPA, exists only for repulsive ph interaction [Nozières, 1964].

In the preceding examples the collective mode was damped because we considered a high momentum q and relatively weak pairing. In order to see more clearly the collective mode, let us now choose a lower density $\rho = 0.016$ fm^{-3} and smaller momenta. In the upper panel of Fig. 4.3, we see the imaginary part of the response function for momenta between $q = 0.5\,k_F$ and $1.3\,k_F$. Now there is a pole in the real part of the response function below the continuum threshold, corresponding to an undamped collective mode. In principle, the imaginary part has a δ-function peak at this energy, which is represented as an arrow in Fig. 4.3. The height of each arrow indicates the strength contained in the peak, which is proportional to the derivative $d(\Pi^{-1})/d\omega$ calculated at the pole of Π. We can see that the strength is highest for small q and decreases as the mode approaches the continuum threshold. At momenta higher than ~ 1.5 fm^{-1} (see lower panel of Fig. 4.3), the collective mode enters again into the continuum, as in Fig. 4.2.

Let us study in more detail the dispersion relation $\omega_\mathbf{q}$ of the collective mode. In Fig. 4.4, the solid lines represent the dispersion relations of the undamped collective mode at densities $\rho = 0.016$ (upper panel) and 0.04 fm^{-3} (lower panel). We see that at small q, the dispersion relation is practically linear. The fact that $\omega \to 0$ for $q \to 0$, as required by the Goldstone theorem, is in practice a very good test of our numerics, since $\omega_{\mathbf{q}=0}$ is extremely sensitive to small numerical errors in the matrix $\langle\langle \Pi^{(0)}_\mathbf{q} V \rangle\rangle$. Another test is the slope $d\omega/dq$ at $q = 0$, which agrees perfectly with the hydrodynamic speed of sound calculated from Eq. (3.58) (dash-dotted lines). We see that $\omega_\mathbf{q}$ stays more or less linear as long as $\omega \ll 2\Delta_{k_F}$. Since in the case $\rho = 0.04$ fm^{-3} the gap Δ_{k_F} is smaller and the speed of sound u is higher, the range of applicability of the hydrodynamic approximation is smaller than in the case $\rho = 0.016$ fm^{-3}. At larger q, the mode frequency starts to bend and approaches the pair-breaking threshold, which is represented by the dots (approaching

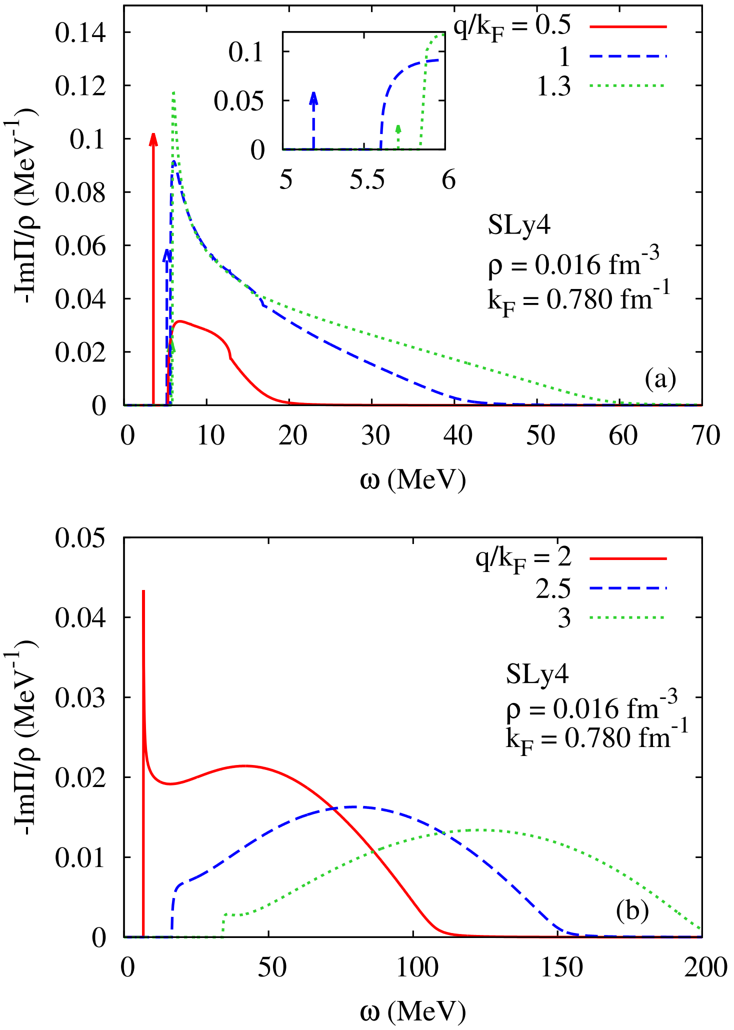

Figure 4.3: QRPA response functions for $q/k_F = 0.5, 1, 1.3$ (a) and $2, 2.5, 3$ (b) at $\rho = 0.016$ fm^{-3} as functions of the excitation energy ω. The arrows in the upper panel represent δ-function peaks corresponding to the undamped collective modes. Their height is proportional to their strength which corresponds to 71.3% ($q = 0.5k_F$), 25.2% ($q = k_F$), and 9.5% ($q = 1.3k_F$) of the total strength of the response function. In the lower panel (b), the collective mode lies above the continuum threshold.

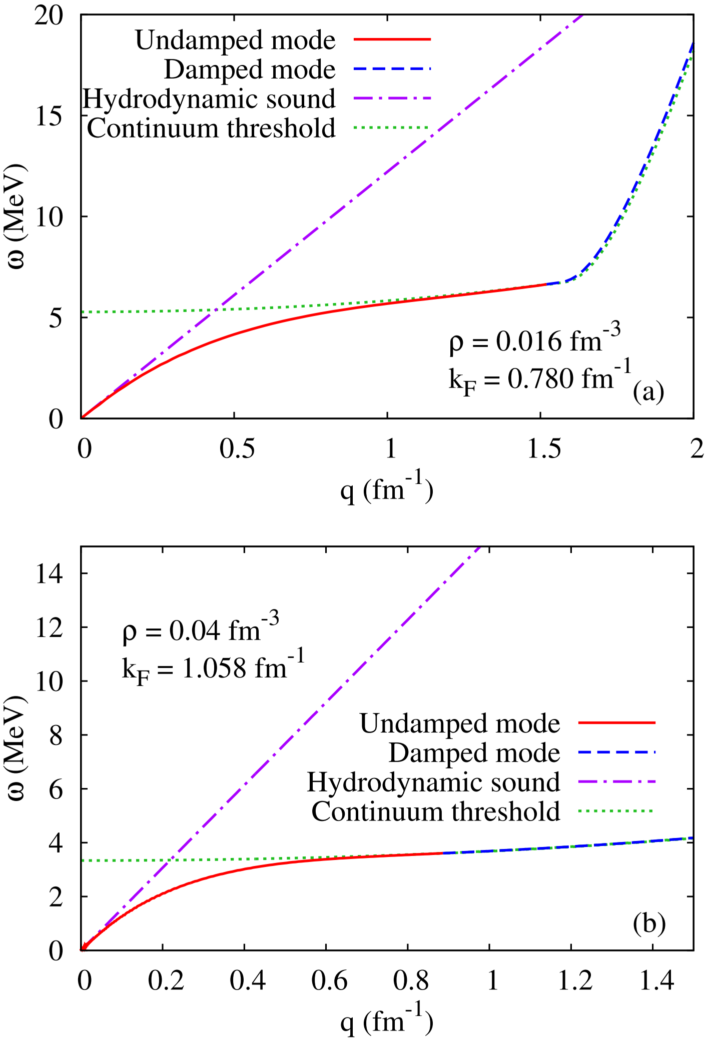

Figure 4.4: Dispersion relation $\omega_{\mathbf{q}}$ of the undamped (solid line) and damped (dashes) collective mode at $\rho = 0.016$ (a) and 0.04 fm^{-3} (b). At small q, it agrees with the linear dispersion relation $\omega = uq$ of hydrodynamic sound (dash-dotted line). At higher q, it approaches and finally crosses the pair-breaking threshold (dotted line).

$2\Delta_{k_F}$ and $q(q/2-k_F)/m^*$, respectively, in the limits of very small and very large q/k_F). Above a certain q, (e.g., ~ 1.5 fm^{-1} for $\rho = 0.016$ fm^{-3} and ~ 0.9 fm^{-1} for $\rho = 0.04$ fm^{-3}) the mode enters into the continuum (dashes) but it stays practically at the threshold (cf. also lower panel of Fig. 4.3). This behavior of the collective mode is qualitatively different from the one shown in Ref. [Keller and Sedrakian, 2013] but similar to the one obtained in Ref. [Baldo and Ducoin, 2011]. Also in the context of ultracold atoms, results similar to ours have been found, see Ref. [Combescot et al., 2006] for a QRPA calculation and Ref. [Forbes and Sharma, 2014] where the collective mode was studied as small-amplitude oscillation in a time-dependent density-functional theory implementation (similar to TDHFB).

4.3 Comparison with the Landau approximation

Now we discuss the results obtained within the Landau approximation as explained in Sec. 3.3. This approximation has recently been used in Refs. [Baldo and Ducoin, 2011, Keller and Sedrakian, 2013]. In Fig. 4.5 we display response functions for two different densities ($\rho = 0.016$ and 0.04 fm^{-3}) and momenta ($q = 0.3$ and 1.5 fm^{-1}) within the Landau approximation keeping only F_0 (dotted lines), and within the Landau approximation keeping F_0 and F_1 as required by Galilean invariance (dashes), and compare them with the full QRPA results (solid lines). In the case of small momentum transfer ($q = 0.3$ fm^{-1}, left panels of Fig. 4.5), the three calculations give very similar results. As in Fig. 4.3, the arrows indicate the energy and strength of the undamped collective mode. We see that the Landau approximation (with F_0 and F_1, and even with F_0 only) works very well for the energy of the collective mode, only the strength (height of the arrow) is slightly different from that obtained in the full QRPA [2]. At excitation energies above ~ 10 MeV one starts to see a difference between the two Landau approximations. As expected, the result obtained with F_0 and F_1 is in better agreement with the full QRPA than that obtained with F_0 only, as one can see in the upper left panel of Fig. 4.5.

The situation is completely different at higher momentum transfer. In

---

[2] It is well known that the sound velocity is given by $u^2 = k_F^2/(3m^{*2})(1+F_0)(1+F_1/3)$ [Leggett, 1966]. However, the last term depending on F_1 does not originate from the residual interaction, but from the effective mass m^*, which is related to F_1 by Galilean invariance: $u^2 = k_F^2/(3mm^*)(1+F_0)$ [Nozières, 1964]. Therefore, if one calculates the response function with the effective mass m^*, one already obtains the correct sound velocity by including only F_0 in the residual interaction.

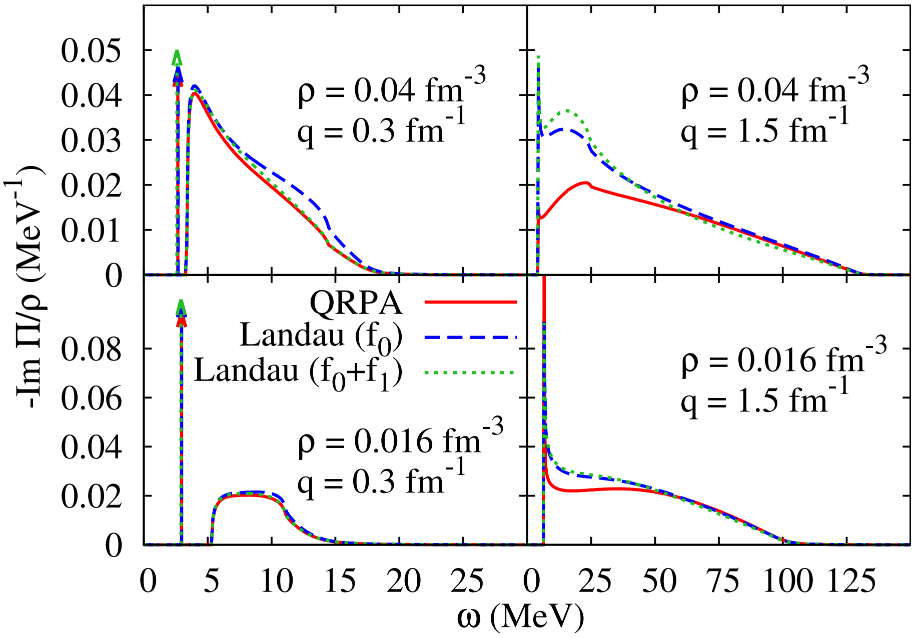

Figure 4.5: Response functions obtained within the full QRPA (solid lines) and within the Landau approximation including only F_0 (dotted lines) or F_0 and F_1 (dashes) as functions of the excitation energy ω for neutron densities $\rho = 0.016$ fm^{-3} (lower panels) and 0.04 fm^{-3} (upper panels) and momenta $q = 0.3$ fm^{-1} (left panels) and 1.5 fm^{-1} (right panels). The arrows in the left panels indicate positions and strengths of the collective modes. In QRPA, the strengths of the collective modes correspond to 82% ($\rho = 0.016$ fm^{-3}) and 52% ($\rho = 0.04$ fm^{-3}) of the total strength of the response functions.

the right panels of Fig. 4.5, we show results for $q = 1.5\ \mathrm{fm}^{-1}$. In this case, the collective mode has disappeared in the continuum. Now the responses obtained within the Landau approximation and within the full QRPA are clearly different. This is not surprising, since the basic assumption underlying the Landau approximation, namely that the excited quasiparticles are close to the Fermi surface, is no longer fulfilled, and also the q dependence of the residual ph interaction [term $W_1(q)$] is no longer negligible. We note that the inclusion of the F_1 Landau parameter does not improve the agreement of the Landau approximation with the full QRPA in this case.

To conclude, the Landau approximation seems to be sufficient to establish the dispersion curve of the collective mode of the neutron gas. However, it may strongly affect calculations that need the entire response function, e.g. the neutrino mean free path in neutron stars [Margueron et al., 2003].

4.4 Heat capacity

In Ref. [Fortin et al., 2010] it was pointed out that neutron pairing results in a strong suppression of the heat capacity at low temperature, which might have observable effects on the neutron star cooling. The relevant temperature range is $T \lesssim 10^9$ K ~ 100 keV, which is much smaller than Δ_{k_F} in the region we are interested in. The quasiparticle contribution to the specific heat at temperature T can be obtained from

$$c_{v,\mathrm{qp}} = T\left.\frac{\partial s_{\mathrm{qp}}}{\partial T}\right|_{\rho}, \tag{4.1}$$

where s_{qp} denotes the entropy density of thermally excited quasiparticles [Tinkham, 1975]

$$s_{\mathrm{qp}} = -2\sum_{\mathbf{p}}\left[\left(1-f(E_{\mathbf{p}})\right)\ln\left(1-f(E_{\mathbf{p}})\right)+f(E_{\mathbf{p}})\ln\left(f(E_{\mathbf{p}})\right)\right] \tag{4.2}$$

with $f(E) = 1/(e^{E/T}+1)$. Indeed, $c_{v,\mathrm{qp}}$ is suppressed by a factor of $e^{-\Delta_{k_F}/T}$ at low temperature, as it is the case in superconducting metals [Fetter and Walecka, 1971]. Note that in a superconductor, the Bogoliubov-Anderson mode is shifted upwards to the plasma frequency by the Coulomb interaction [Nambu, 1960] and therefore its contribution to the specific heat is negligible. However, in a superfluid such as the neutron gas the situation is different because here the Bogoliubov-Anderson mode is the dominant contribution to the specific heat at low temperature, and not the quasiparticles.

At $T \ll \Delta_{k_F}$, we can neglect the temperature dependence of the collective mode itself, i.e., we can calculate its contribution to the specific heat by using its dispersion relation $\omega_{\mathbf{q}}$ obtained at $T = 0$:

$$c_{v,\mathrm{coll}} = \frac{1}{T^2} \sum_{\mathbf{q}} \frac{\omega_{\mathbf{q}}^2 e^{\omega_{\mathbf{q}}/T}}{(e^{\omega_{\mathbf{q}}/T} - 1)^2} . \tag{4.3}$$

At low temperatures, this reduces to

$$c_{v,\mathrm{coll}} = \frac{2\pi^2 T^3}{15u^3} , \tag{4.4}$$

where u is the sound velocity of the collective mode. The T^3 behavior is analogous to the specific heat of phonons in a solid [Debye, 1912, Ashcroft and Mermin, 1976]. So, we see that at low temperatures the contribution of the neutron gas to the specific heat is reduced as compared to the specific heat of unpaired neutrons, which would be linear in T. But the reduction is not as drastic as the exponential suppression of $c_{v,\mathrm{qp}}$. This is illustrated in Fig. 4.6, where the specific heats of the quasiparticles, Eq. (4.1) (dashed lines), and of the collective mode, Eq. (4.3) (solid lines), are displayed as functions of temperature. As densities of the neutron gas we take $\rho = 0.003$ (upper panel) and 0.0184 fm^{-3} (lower panel), which appear in the neutron-star crust at total baryon densities of $\rho_B \approx 0.00373$ and 0.0204 fm^{-3}, respectively [Negele and Vautherin, 1973].

In addition to the QRPA results, we also show approximate results for the contribution of the collective mode obtained with the hydrodynamic sound velocity and Eq. (4.4) (dashed-dotted lines). At low temperatures, Eq. (4.4) is in perfect agreement with the QRPA result. This is a reassuring result since in many studies [Di Gallo et al., 2011, Aguilera et al., 2009, Chamel et al., 2010, Cirigliano et al., 2011, Chamel et al., 2013a, Kobyakov and Pethick, 2013] the contribution of the collective mode was calculated assuming the validity of the hydrodynamic approximation (long-wavelength limit). At higher temperatures, where the QRPA result starts to deviate considerably from Eq. (4.4), also our approximation to neglect temperature effects in the QRPA itself becomes questionable, as one can see from the increasing contribution of thermal quasiparticles.

Let also mention that at very low densities (such as $\rho = 0.003$ fm^{-3}), the sound velocity is close to that of an ideal Fermi gas, $u \approx k_F/(\sqrt{3}m)$, so that Eq. (4.4) is well approximated by $c_{v,\mathrm{coll}} \approx 2\sqrt{3}m^3T^3/(15\rho)$. While the discrepancy between this simple formula and Eq. (4.4) is less than 10 % in the case of $\rho = 0.003$ fm^{-3}, it is a factor of 3 in the case of $\rho = 0.0184$ fm^{-3}

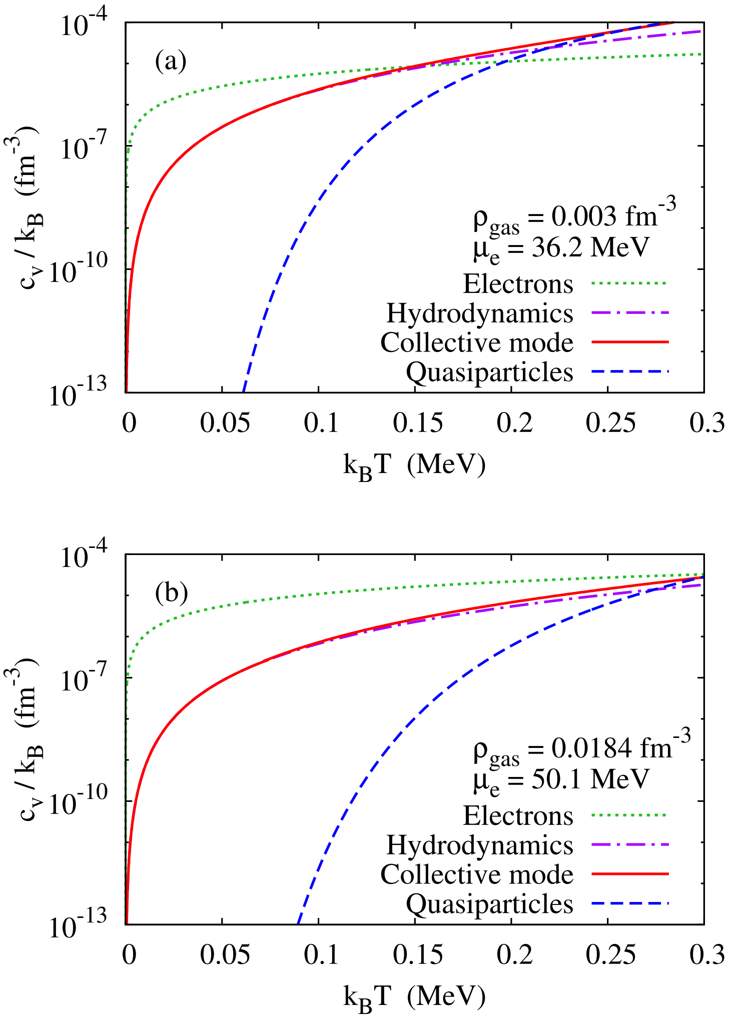

Figure 4.6: Heat capacity of a neutron gas with density $\rho = 0.003$ (a) and 0.0184 fm^{-3} (b), corresponding to total baryon densities in the neutron-star crust of $\rho_B \approx 0.00373$ and 0.0204 fm^{-3}, respectively: neutron quasiparticle contribution (dashes), contribution of the collective mode calculated within QRPA (solid lines) and within the hydrodynamic approximation (dashed-dotted lines). For comparison, we also display the electron contribution (dotted lines) under the assumption of $\mu_e = 36.2$ (a) and 50.1 MeV (b), corresponding to electron densities $\rho_e = 2.1 \cdot 10^{-4}$ and $5.5 \cdot 10^{-4}$ fm^{-3}.

where the sound velocity is considerably reduced by the attractive neutron-neutron interaction.

To assess the importance of the contribution of the collective mode to the specific heat of the inner crust, we show in Fig. 4.6 also the electron contribution (dotted lines), which is linear in temperature,

$$c_{v,e} = \frac{\mu_e^2 T}{3}\,. \tag{4.5}$$

The values of the electron chemical potentials $\mu_e = 36.2$ and 50.1 MeV used in the upper and lower panel of Fig. 4.6, respectively, were obtained from the neutron and proton chemical potentials given in Ref. [Negele and Vautherin, 1973] and the relation $\mu_e = \mu_n - \mu_p$ of β-equilibrium. One sees that, at not too low temperatures, the contribution of the collective mode is comparable to that of the electrons. In the case $\rho = 0.003$ fm^{-3}, the contribution of the collective-mode even exceeds that of the electrons at $T \gtrsim 150$ keV.

4.5 Conclusion

In this chapter we used the QRPA to study collective excitations in a uniform superfluid neutron gas. We focused on low densities such as they are predicted in the inner crust of neutron stars. At these densities, the neutron pairing in the s wave is relatively strong. For the interaction, we used a Skyrme force in the ph channel and a separable interaction with a Gaussian form factor in the pp channel. We derived the QRPA density response by taking the small-amplitude limit of the TDHFB equations.

Since the HFB ground state breaks the global $U(1)$ symmetry, a Goldstone mode, corresponding to phase oscillations of the superfluid gap, must exist. This Bogoliubov-Anderson sound is actually a simple density wave, in other channels (e.g., spin modes) there are no ungapped modes. Since we treat the ph and pp residual interactions consistently with the HFB ground state, our QRPA density response automatically exhibits the Bogoliubov-Anderson sound with a linear dispersion relation $\omega = uq$ at low momentum q. The speed of sound u coincides with the hydrodynamic one. However, as ω approaches the pair-breaking threshold at $\sim 2\Delta_{k_F}$, substantial deviations from the linear dispersion relation are found: instead of crossing the threshold near $q = 2\Delta_{k_F}/u$, the dispersion relation of the collective mode bends, slowly approaches the threshold, and closely follows it, before it finally crosses it at a much higher q and enters into the two-quasiparticle continuum.

We also checked the quality of the Landau approximation to the residual interaction. We found that at low momenta ($q \lesssim 1$ fm^{-1}) the Landau approximation is sufficient to describe the collective mode. In this range of momenta, also the continuum of the response function is well described if one includes in addition to the $l = 0$ Landau parameter F_0 also the $l = 1$ parameter F_1, as required to satisfy Galilean invariance in the case of an effective mass $m^* \neq m$. At higher momenta ($q \gtrsim 1$ fm^{-1}), the QRPA response function is not well reproduced by the Landau approximation. In this case, the inclusion of the parameter F_1 in addition to F_0 does not significantly improve the result. However, we note that in the case of a Skyrme interaction, the computation of the full QRPA response is almost as simple as the calculation within the Landau approximation, so that there is no good reason not to do the full calculation.

The existence of an ungapped collective mode has a strong effect on the heat capacity of the neutron gas. While quasiparticle excitations are exponentially suppressed at low temperature $T \ll \Delta_{k_F}$ because of the gap, the collective mode can be excited at arbitrarily low temperatures and leads to a specific heat which is proportional to T^3 at low T, inceasing the neutron-gas contribution to the specific heat by several orders of magnitude in the temperature range relevant for neutron stars. Depending on density and temperature, the contribution of the collective mode to the specific heat of the inner neutron-star crust can be comparable to or even larger than that of the electrons.

As we have seen, in a uniform gas the QRPA response at low energies is well reproduced by simple hydrodynamics. However, in reality the neutron gas in the inner crust is not uniform, but it contains clusters having a higher density and consisting of neutrons and protons. These clusters form a Coulomb crystal. The clusters can also take the shape of cylinders or plates, in this case one speaks of “pasta phases”. The coupling between the collective mode of the neutron gas and the lattice phonons of the clusters is very important [Cirigliano et al., 2011, Chamel et al., 2013a]. As long as the coherence length of the Cooper pairs is less than the size of these structures, the hydrodynamic approach should remain a reasonable approximation. Work in this direction has been done in Ref. [Di Gallo et al., 2011] for the so-called “lasagne” phase and we performed calculations for crystal and “spaghetti” phase, as detailed in the following Part III. For an extension of the present study to the response of uniform matter with higher density, as it exists in the neutron star core, one has to include also the proton component and treat neutron pairing in the p wave.

For a complete description of cooling of neutron stars [Page and Reddy, 2013], the collective modes do not only play a role in the specific heat, but also in the heat conductivity. A discussion of these aspects, based on the long-wavelength approximation for the collective modes [Cirigliano et al., 2011], can be found in Ref. [Page and Reddy, 2012]. Again, the coupling between the collective mode of the superfluid and the lattice phonons seems to be very important. Therefore, a unified description of the Bogoliubov-Anderson mode and the lattice phonons from a more microscopic perspective would be desirable.

Part III

Nuclear matter in the inner crust

Chapter 5

Neutron star matter

5.1 Introduction

The usual picture of the neutron-star crust [Chamel and Haensel, 2008] is that one starts from a Coulomb crystal of nuclei in the outer crust. As one goes deeper into the star, the nuclei become more and more neutron rich (as a consequence of the increasing electron chemical potential and β-equilibrium) until the neutron drip line is reached. This defines the transition to the inner crust, where the nuclei ("clusters") are embedded in a dilute gas of unbound neutrons. The inhomogeneous phases in the inner crust can also be interpreted in another way [Avancini et al., 2008], which is quite common in the study of supernova matter (i.e., matter at finite temperature and out of β-equilibrium) [Pais et al., 2015, Aymard et al., 2014], namely as a consequence of the first-order liquid-gas instability of nuclear matter. One aim of the present chapter is to see to what extent the simple picture of phase coexistence can explain certain properties of the inhomogeneous phases of the inner crust of neutron stars. However, within the most simple phase-coexistence picture, surface- and Coulomb energies are neglected. An approximate way to include them is to use a more microscopic approach, namely to parameterize the density profile and determine its parameters by minimizing the thermodynamic potential.

5.2 Thermodynamical approaches

5.2.1 Uniform matter

The most simple model of stellar matter consists in assuming uniform matter under β-equilibrium. Obviously this approach neglects the inhomogeneities of the inner crust. However, it could be a satisfying approximation for the outer core, i.e., where the density is uniform and of the order of saturation density of nuclear matter. (Beyond a few times the saturation density, one expects hyperons or quark-gluon plasma [Chamel and Haensel, 2008].) The chemical composition of the uniform matter is driven by the β-equilibrium:

$$\mu_e = \mu_n - \mu_p \,, \tag{5.1}$$

with μ_e the electron chemical potential and μ_q the chemical potential for $q = (n, p)$ neutron and proton, respectively. For practical purpose, the electron mass can usually be neglected so that $\mu_e = (3\pi\rho_e^2)^{1/3}\hbar c$, with ρ_e the electron number density. Furthermore, neutron star matter has to satisfy electric charge neutrality, i.e., the electron density respects $\rho_e = \rho_p$, with ρ_p the proton density. Thus, we can rewrite the β-equilibrium as:

$$\hbar c(3\pi^2\rho_p)^{1/3} = \mu_n - \mu_p \,. \tag{5.2}$$

We use a Skyrme energy-density functional (EDF) [Chabanat et al., 1997] to calculate the energy density ϵ_{Sk} as a function of ρ_n and ρ_p. In fact, by choosing the Skyrme functional, the expression of μ_q is analytical and is strictly function of ρ_n and ρ_p:

$$\mu_q = \frac{\partial \mathscr{E}_{\text{Sk}}}{\partial \rho_q} \,, \tag{5.3}$$

and the pressure

$$P = -\mathscr{E}_{\text{Sk}} + \mu_n\rho_n + \mu_p\rho_p \,, \tag{5.4}$$

appearing in Eqs. (5.5) and (5.6). We use different Skyrme parametrizations, all fitted to the neutron-matter equation of state: the Saclay-Lyon forces SLy4 and SLy7 [Chabanat et al., 1998] and the Brussels-Montreal forces BSk20 and BSk22 [Goriely et al., 2013].

5.2.2 Phase coexistence

As a first approximation, the inhomogeneous inner crust could be described as a phase coexistence of liquid drops (corresponding to the nuclear clusters) with volume V^{liq} and a gas (the dilute neutron gas) with volume V^{gas} (see Fig. 5.1), which satisfies mechanical and chemical equilibrium, i.e.,

$$P^{\text{gas}} = P^{\text{liq}} \,, \tag{5.5}$$

$$\mu_q^{\text{gas}} = \mu_q^{\text{liq}} \,, \tag{5.6}$$

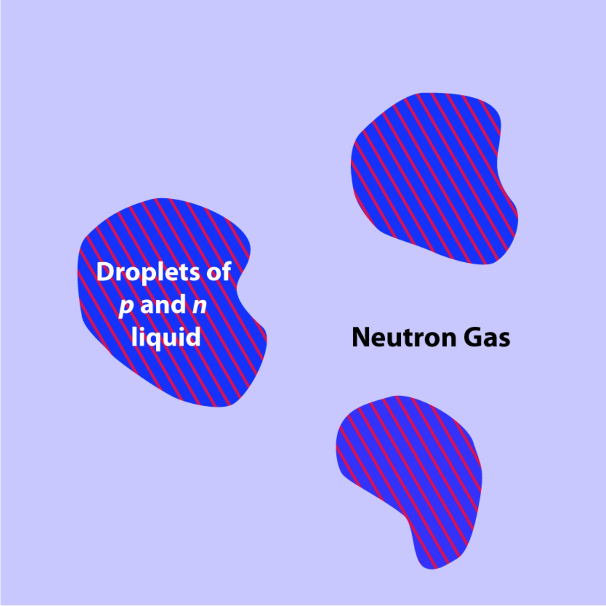

Figure 5.1: A schematic view of the phase coexistence. This framework neglects the surface energy, which is illustrated by an arbitrary and irregular surface of the droplets.

with P^i the pressure, and μ_q^i the chemical potential in the phase i.

In addition to the neutrons and protons, we consider again a uniform electron gas to ensure charge neutrality, i.e.,

$$V\rho_e = V^{\text{liq}}\rho_p^{\text{liq}} + V^{\text{gas}}\rho_p^{\text{gas}}, \tag{5.7}$$

where $V = V^{\text{liq}} + V^{\text{gas}}$ is the total volume and ρ_p^i is the proton density in phase i (ρ_p^{gas} is not always zero). Instead of working with the volumes, it is more convenient to introduce the volume fraction u filled by the liquid, which satisfies

$$u = \frac{V^{\text{liq}}}{V} = \frac{\rho_e - \rho_p^{\text{gas}}}{\rho_p^{\text{liq}} - \rho_p^{\text{gas}}}. \tag{5.8}$$

Furthermore, in neutron stars, matter is in β-equilibrium (5.1). Similarly to uniform matter (see Sec. 5.2.1), the electron mass can be neglected. Thus we obtain for the volume fraction

$$u = \frac{1}{\rho_p^{\text{liq}} - \rho_p^{\text{gas}}}\left[\frac{(\mu_n - \mu_p)^3}{3\pi^2(\hbar c)^3} - \rho_p^{\text{gas}}\right]. \tag{5.9}$$

5.3 Semiclassical approach

In the phase-coexistence picture described before, we could determine the volume fraction u, but not the actual size of the clusters. The latter is determined by finding the best compromise between the Coulomb energy (favoring small clusters) and the surface energy (favoring large clusters), which were both neglected in the phase-coexistence picture. Let us now consider a more sophisticated approach, where these effects are included.

5.3.1 Extended Thomas-Fermi approximation

In nuclear physics the development of semiclassical approaches, and in particular of the Extended Thomas-Fermi (ETF) method dates back to the 1980s [Brack et al., 1985]. At this time, the improvement of the fission barrier calculations [Brack et al., 1985] made necessary to perform new fits of the nuclear effective interactions (e.g. such as Skyrme or Gogny). The latter was too expensive in terms of computer times needed by HF calculations in the 1980s [Brack et al., 1985]. Hence, the ETF approximation turned out to be an efficient solution to perform new fits. Actually, the ETF theory provides local density functionals of kinetic energy $\tau[\rho]$ and spin current $\mathbf{J}[\rho]$ densities, defined for the Skyrme density functional in Ref. [Brack et al., 1985]. In the last years, interest has been renewed in ETF for the description of exotic neutron-rich nuclei, in neutron star matter [Aymard et al., 2014].

The ETF functionals are improvements of the Thomas-Fermi (TF) approximation, thanks to the semiclassical $\hbar$-expansion developed by [Wigner, 1932] and [Kirkwood, 1933] (the so-called *Wigner-Kirkwood expansion*). At the zeroth order (TF approximation), the kinetic energy reads as [Brack et al., 1985]:

$$\tau_{\mathrm{TF}}[\rho_q] = \frac{3}{5}(3\pi^2)^{2/3}\rho_q^{5/3}, \tag{5.10}$$

with ρ_q the single-particle density for $q=(n,p)$, neutron and proton, respectively. By expanding to the second $\hbar^2$ order, one has [Brack et al., 1985]:

$$\tau_2^L[\rho_q] = \frac{1}{36}\frac{(\nabla\rho_q)^2}{\rho_q} + \frac{1}{3}\Delta\rho_q, \tag{5.11}$$

$$\tau_2^{NL}[\rho_q] = \frac{1}{6}\frac{\nabla\rho_q\cdot\nabla f_q}{f_q} + \frac{1}{6}\rho_q\frac{\Delta f_q}{f_q} - \frac{1}{12}\rho_q\left(\frac{\nabla f_q}{f_q}\right)^2 + \frac{1}{2}\left(\frac{2m}{\hbar^2}\right)\rho_q\left(\frac{\mathbf{W}_q}{f_q}\right)^2. \tag{5.12}$$

In the two last equations, τ_2^L and τ_2^{NL} denote the second-order local and non-local (effective mass and finite range approximation, see Eq. (2.6)) terms, respectively. The effective mass ratio is defined by $f_q = m/m_q^*$, with m_q^* the effective mass (2.8). Finally, the total kinetic energy reads as:

$$\tau_{\mathrm{ETF}} = \sum_q \tau_{\mathrm{TF}}[\rho_q] + \tau_2^L[\rho_q] + \tau_2^{NL}[\rho_q]. \tag{5.13}$$

In addition, with respect to the ETF approximation, the spin current $\mathbf{J}_q$ is expressed as follows [Brack et al., 1985]:

$$\mathbf{J}_q = -\frac{2m}{\hbar^2}\frac{\rho_q \mathbf{W}_q}{f_q}, \tag{5.14}$$

with $\mathbf{W}_q$ the spin-orbit field [Chabanat et al., 1998]

$$\mathbf{W}_q = \frac{1}{2} W_0 (\nabla\rho + \nabla\rho_q), \tag{5.15}$$

and $\rho = \rho_n + \rho_p$ the total density.

5.3.2 Surface parametrization

In the introduction of this section, we mentioned briefly the necessity of the surface energy in order to determine the size of the clusters (in contrast to the phase-coexistence framework). Here, the surface energy is computed within the semiclassical ETF approximation [Brack et al., 1985, Aymard et al., 2014]. Instead of solving the Euler-Lagrange equation [Lassaut et al., 1987, Baldo et al., 2014], we use a parametrization of the density profile. Our density is parametrized with a generalized Fermi-Dirac (FD) profile

$$\rho_q(r) = \rho_q^{\mathrm{gas}} + \frac{\rho_q^{\mathrm{liq}} - \rho_q^{\mathrm{gas}}}{\left\{1 + \exp\left[(r - r_q)/a_q\right]\right\}^{\gamma_q}}, \tag{5.16}$$

and the energy is minimized with respect to the 11 parameters ρ_q^i, r_q, a_q, γ_q, and the cell size. Let us note that if one fixes $\gamma_q = 1$ then we have a standard Fermi-Dirac profile, so that the minimization is performed with respect to 9 parameters. This parametrization looks similar to the shape obtained in Hartree-Fock calculation, e.g., Ref. [Negele and Vautherin, 1973, Aymard et al., 2014] and has a simple interpretation: ρ_q^{liq} and ρ_q^{gas} correspond, respectively, to the asymptotic densities in the cluster and in the gas far away from the surface, r_q describes the cluster radius, including the possibility of a neutron skin if $r_n > r_p$, and a_q is the surface diffuseness. The factors γ_q add two degrees of freedom, which allow one to describe an "asymmetric" surface. One can compare FD and generalized FD profiles at same the chemical potential in Fig. 5.2. However, the difference for a same chemical potential is very slight and does not modify strongly the calculations (see Chap. 6), so that we restrict the minimization to 9 parameters by fixing $\gamma_q = 1$.

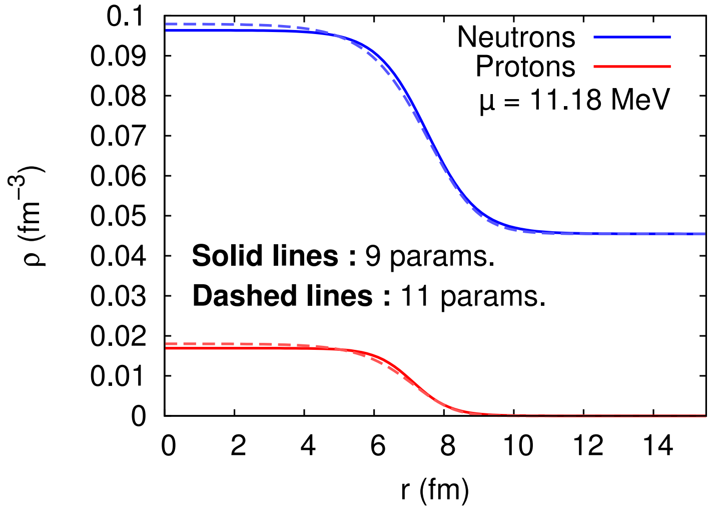

Figure 5.2: Density profiles obtained for a spherical cluster at fixed chemical potential $\mu = 11.18$ MeV. The solid line corresponds to the results obtained with 9 parameters (FD), while the dashed line describes the 11 parameters (generalized FD) results.

Note that a similar approach was followed by [Oyamatsu, 1993] and by [Pearson et al., 2012]. However, Oyamatsu used a completely different parametrization of the density, which did not become constant inside the cluster. Our parametrization (5.16) resembles more the one used by Pearson *et al.*

5.3.3 Energy minimization

As discussed in the preceding subsection, we chose to parametrize the surface, instead of solving the Euler-Lagrange equation, so that we have to minimize the energy with respect to all the parameters. Concerning the structure of the inner crust, it is belived to be periodic because a periodic lattice minimizes the Coulomb energy [Oyamatsu et al., 1984]. Let us note that the periodicity increases strongly the complexity of the Coulomb energy calculation, by requiring the Ewald summation. However, the Coulomb energy is absolutely necessary for the minimization, because of its major

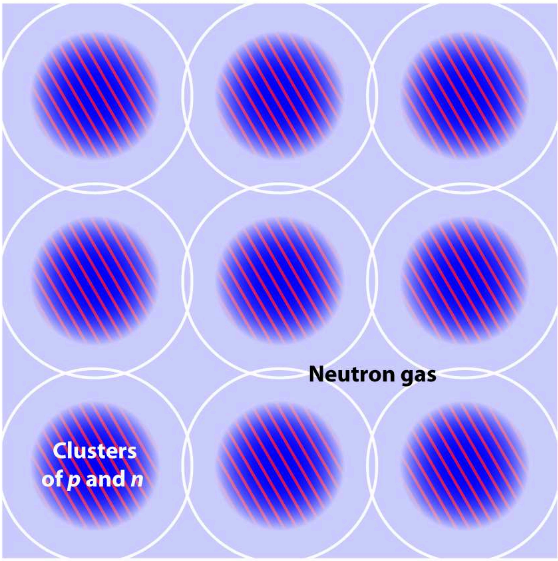

Figure 5.3: Scheme of the Wigner-Seitz (WS) approximation performed within the ETF framework. The WS cell borders are displayed by the white circles surrounding the clusters. The surface between the liquid and the gas is blurred in order to materialize the diffuseness of the surface.

role in the competition with the surface energy (see Sec. 1.3.1), which determines the cluster size and surface shape. Hence, we use the Wigner-Seitz (WS) approximation, i.e., we calculate the Coulomb energy in an isolated cell $r < R_{\mathrm{WS}}$, with R_{WS} chosen such that the volume of the WS cell corresponds to the volume of the unit cell, as displayed in Fig. 5.3.

In addition, it seems very hard to perform the minimization of the energy for fixed average densities (averaged over the WS cell), since the average densities depend on all the parameters. We therefore introduce chemical potentials μ_q as Lagrange parameters to fix the densities and minimize the thermodynamic potential instead of the energy. To be precise, we minimize $\omega = -P = \Omega/V_{\mathrm{WS}}$, where

$$\Omega = E_{\mathrm{Sk}} - \mu_n N - \mu_p Z - \mu_e Z + E_e + E_C + E_{\mathrm{ex}}\,, \tag{5.17}$$

which reduces to

$$\Omega = E_{\mathrm{Sk}} - \mu_n (N+Z) + E_e + E_C + E_{\mathrm{ex}}\,, \tag{5.18}$$

because of the β-equilibrium constraint (5.1). In this equation, E_{Sk} denotes the energy obtained with the Skyrme functional, N and Z are the total numbers of neutrons and protons in the WS cell, E_e denotes the energy of the electron gas, E_C the Coulomb energy, and E_{ex} the energy due to the Coulomb exchange term.

The volume V_{WS} of the WS cell depends on R_{WS} and on the geometry one considers (spheres, rods, or slabs). Let us define the functions $S_d(r)$ and $V_d(r)$ describing, respectively, the "surface" and the "volume" of a d dimensional sphere of radius r, i.e.,

$$S_1(r) = 2\,, \qquad S_2(r) = 2\pi r\,, \qquad S_3(r) = 4\pi r^2\,, \tag{5.19}$$

$$V_1(r) = 2r\,, \qquad V_2(r) = \pi r^2\,, \qquad V_3(r) = \tfrac{4}{3}\pi r^3\,. \tag{5.20}$$

In the case of spheres ($d = 3$), the volume of the WS cell is $V_{\text{WS}} = V_3(R_{\text{WS}})$. In the case of rods ($d = 2$), the "volume" $V_{\text{WS}} = V_2(R_{\text{WS}})$ is actually an area and consequently E, N, Z, etc. represent energies and particle numbers per unit length. Similarly, in the case of slabs ($d = 1$), the "volume" $V_{\text{WS}} = V_1(R_{\text{WS}})$ is a length and E, N, Z, etc. represent energies and particle numbers per unit area.

The integrated Skyrme energy in the WS cell, E_{Sk}, is defined as

$$E_{\text{Sk}} = \int_0^{R_{\text{WS}}} d^d r\, \mathscr{E}_{\text{Sk}}[\rho_n(r), \rho_p(r)]\,, \tag{5.21}$$

with $d^d r = S_d(r)dr$ and $\mathscr{E}_{\text{Sk}}$ the Skyrme EDF (2.6), the kinetic energy density $\tau_q(r)$ being calculated within the ETF approximation cf. Eqs. (5.10)–(5.14).

For the electron gas, we assume a constant density $\rho_e = Z/V_{\text{WS}}$. Hence, its energy can be written as $E_e = V_{\text{WS}}\epsilon_e$. The energy density ϵ_e, taking into account the electron mass m_e, reads [Baldo et al., 2014]

$$\epsilon_e = \frac{\hbar c k_{F,e}^4}{4\pi^2}\left[\left(1 + \frac{1}{2x_e^2}\right)\sqrt{1 + \frac{1}{x_e^2}} - \frac{\sinh^{-1} x_e}{2x_e^4}\right]\,, \tag{5.22}$$

with $k_{F,e} = (3\pi^2\rho_e)^{1/3}$ and $x_e = \hbar k_{F,e}/m_e c$.

The exchange term of the Coulomb interaction is computed within the Slater approximation [Baldo et al., 2014]. For the protons, it is given by the integral of

$$\epsilon_{\text{ex},p}(r) = -\frac{3}{4}\left(\frac{3}{\pi}\right)^{1/3} e^2 \rho_p^{4/3}(r)\,, \tag{5.23}$$

over the WS cell. For the relativistic electrons, the exchange energy includes also contributions from transverse photons and gets positive for $x_e \gtrsim 2.53$

[Salpeter, 1961]. Its expression reads [Rajagopal, 1978]

$$\epsilon_{\mathrm{ex},e} = \frac{e^2 k_{F,e}^4}{8\pi^3} \left\{ 3 \left[\sqrt{1 + \frac{1}{x_e^2}} - \frac{\sinh^{-1} x_e}{x_e^2} \right]^2 - 2 \right\}. \tag{5.24}$$

5.3.4 Coulomb energy

The Coulomb energy E_C is derived from the charge density $\rho_c(r) = \rho_p(r) - \rho_e$. We first calculate the Coulomb potential $V_C(r)$ satisfying the Poisson equation

$$\Delta V_C(r) = -4\pi e^2 \rho_c(r), \tag{5.25}$$

with $\nabla V_C(0) = 0$. This determines $V_C(r)$ only up to a constant, which is however irrelevant for the energy since the total charge of the WS cell is zero. The Coulomb energy is given by

$$E_C = \frac{1}{2} \int_0^{R_{\mathrm{WS}}} d^d r \rho_c(r) V(r). \tag{5.26}$$

Note that $V_C(r)$ and the integral (5.26) must be computed numerically, in contrast to the approximate expressions one obtains for uniformly charged spheres (or rods, or slabs, respectively) with a sharp surface which are often used in the literature [Ravenhall et al., 1983, Hashimoto et al., 1984, Avancini et al., 2010, Pais et al., 2014].

We relaxed the assumption of a constant electron density by using a screened Coulomb potential instead of the full one, i.e., replacing the Poisson equation (5.25) by

$$\left(\Delta - \frac{1}{\lambda^2} \right) V_C(r) = -4\pi e^2 \rho_c(r), \tag{5.27}$$

where λ denotes the Debye screening length, $1/\lambda^2 = (4\alpha/\pi) k_{Fe}^2$ (neglecting the electron mass), with $\alpha = e^2/\hbar c$. From Eq. (5.27), one can define the charge density if screening is included:

$$\rho_c^s(r) = \rho_c(r) - \frac{k_{F,e}^2}{\pi^2 \hbar c} V_C(r). \tag{5.28}$$

Hence, if we consider the proton density $\rho_p(r)$ to be identical in both cases (with and without screening), from now on the electron density is not constant anymore if one accounts for screening. Also, we introduce the density difference of the electrons

$$\Delta \rho_e = \rho_e^s(r) - \rho_e = \frac{k_{F,e}^2}{\pi^2 \hbar c} V_C(r), \tag{5.29}$$

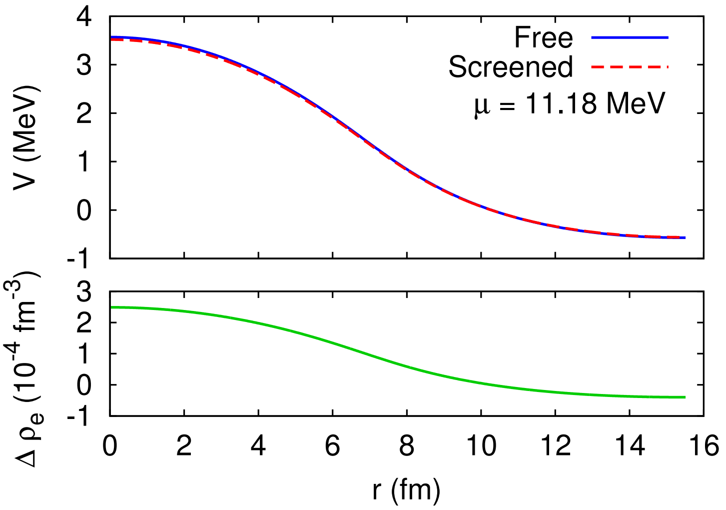

Figure 5.4: In the upper panel, we display the Coulomb potential V calculated without (blue line) and with (dashed red line) screening. This is the results for a spherical cell with neutron chemical potential $\mu = 11.18$ MeV. The lower panel, shows the density difference $\Delta\rho_e = \rho_e^s(r) - \rho_e$, with $\rho_e^s(r)$ the density of electrons if one accounts for the screening.

where $\rho_e^s(r)$ stands for the electron density if screening is included. However, as already noticed in [Maruyama et al., 2005], the screening length of the electrons is so large that this effect is negligible. In Figure 5.4, we present in the upper panel the effect of screening for the Coulomb potential V, where the difference is of the order of a few keV. While, the lower panel of Fig. 5.4 shows the deviation of the electron density, and its maximum is $\Delta\rho_e/\rho_e \sim 14\%$. However, the Poisson equation is function of the total charge density $\rho_c(r)$, the absolute value of maximum deviation is only $\sim 1.6\%$, with respect to $\rho_c(r)$. In conclusion, we neglect the screening effects in the following calculations.

5.3.5 Numerical methods

Since the minimum of the thermodynamic potential $\omega = \Omega/V_{\rm WS}$ (5.18) is very flat in parameter space, the numerical minimization is highly sensitive to slight numerical noise. One remarks that the expression of the kinetic energy $\tau[\rho_q]$ within the ETF framework [see Eqs. (5.11)–(5.13)], contains the Laplacian of the density $\Delta\rho_q$. This dependence is not explicitly written, but in the Skyrme EDF framework, Δf_q is a functional of $\Delta\rho_q$, where $f_q = m/m_q^*$ is the effective mass ratio. Hence, the density has to be constant at $r = 0$ if one wants to have a well defined Laplacian. This condition is not exactly fulfilled if one uses a Fermi-Dirac surface parametrization. Actually, the gradient of such parametrization is only zero in the limit $r \to \infty$.

This problem was solved by performing an integration by parts of the Laplacian terms. One remarks that Δf_q appears twice in the full expression of the Skyrme energy: (i) a term $\rho_q \Delta f_q / f_q$ in the expression of τ_{ETF} and (ii) another term in the velocity-dependent term of the Skyrme functional (2.6), expressed as $\rho_q^2 \Delta f_q / f_q$. The first term can be transformed as follows:

$$\int d^d r \, \rho_q \frac{\Delta f_q}{f_q} = \left[S_d(r) \rho_q \frac{\nabla f_q}{f_q} \right]_0^{R_{\mathrm{WS}}} - \int d^d r \, \nabla f_q \frac{f_q \nabla \rho_q - \rho_q \nabla f_q}{f_q^2} . \tag{5.30}$$

If the density was constant at $r = 0$ and $r = R_{\mathrm{WS}}$ as it should be, i.e., $\nabla \rho_q = 0$, the first term would vanish. Hence the preceding equation reduces to:

$$\int d^d r \, \rho_q \frac{\Delta f_q}{f_q} = - \int d^d r \, \nabla f_q \frac{f_q \nabla \rho_q - \rho_q \nabla f_q}{f_q^2} . \tag{5.31}$$

Similarly, we integrate by parts the velocity-dependent term

$$\int d^d r \, \rho_q \frac{\Delta f_q}{f_q} = - \int d^d r \, \rho_q \nabla f_q \frac{2 f_q \nabla \rho_q - \rho_q \nabla f_q}{f_q^2} . \tag{5.32}$$

It turned out that this approximation of a constant density in the center of the cluster and at the border of the WS cell was sufficient to solve the numerical instabilities.

As mentioned above, the minimization was very delicate because of the flat minimum. Actually, we had to find the most robust minimization procedure. In a first step we tried *gradient methods* which follow the trend of the function until the minimum is reached. However, such approaches require precise values of the gradient and small enough steps (otherwise the minimum could be missed). It turned out that these methods were not precise enough. Generally, the minimization stopped after reaching the boundaries of the parameter space. Another solution was the *Nelder-Mead Simplex (NMS) alorgithm* [Nelder and Mead, 1965]. In contrast to the gradient method, the NMS does not require gradients of the function to minimize. It proceeds by mapping the space surrounding a minimization point. Nevertheless, it requires a lot of computation time to map 9 or 11 dimensions of space. The numerical framework for a NMS minimization is available in the GNU Scientific Library (GSL), see Chap. 35 of Ref. [Galassi et al., 2009]. It required a binding of `FORTRAN` and `C` codes. In fact the GSL is written in `C`, while the core of the numerical calculation of ETF is developed in `FORTRAN`. In addition, we performed a speed up by using a multi-thread parallelization thanks to the OpenMP library.

Chapter 6

Results for the inner crust

After presenting methods for the description of neutron star matter, we will concentrate on the results for the inner crust. Actually, as mentioned in Sec 1.3.1, inhomogeneous nuclear matter is expected in the inner crust. Most of the results shown in the present chapter have been published previously in Ref. [Martin and Urban, 2015].

6.1 Phase coexistence

Let us first discuss the results obtained within the simple phase coexistence approach. Figure 6.1 represents the densities in the gas and in the liquid as functions of the baryon density

$$\rho_b = u(\rho_n^{\text{liq}} + \rho_p^{\text{liq}}) + (1-u)(\rho_n^{\text{gas}} + \rho_p^{\text{gas}}), \tag{6.1}$$

obtained with the BSk22 [Chamel et al., 2013a] and SLy4 interaction [Chabanat et al., 1998]. The main difference between the two parametrizations is the transition to uniform matter, i.e., the point where the liquid fills the whole volume ($u = 1$). For instance, the transition occurs at $\rho_b \approx 0.09$ fm^{-3} with SLy4, while with BSk22 it is below 0.08 fm^{-3}.

Figure 6.2 shows the same results, but on a logarithmic scale so that the low density region is better visible. The region below $\rho_b \approx 10^{-3}$ fm^{-3} corresponds to the outer crust, where $\rho_n^{\text{gas}} = \rho_p^{\text{gas}} = 0$ (i.e., $\mu_n, \mu_p \leq 0$). In the limit of extremely low densities, the droplets are made of symmetric nuclear matter at saturation density ($\rho_n = \rho_p = 0.08$ fm^{-3}). The kink in the densities visible in Fig. 6.2 corresponds to the transition between the outer and the inner crust, i.e., to the point where μ_n becomes positive and the neutron gas appears.

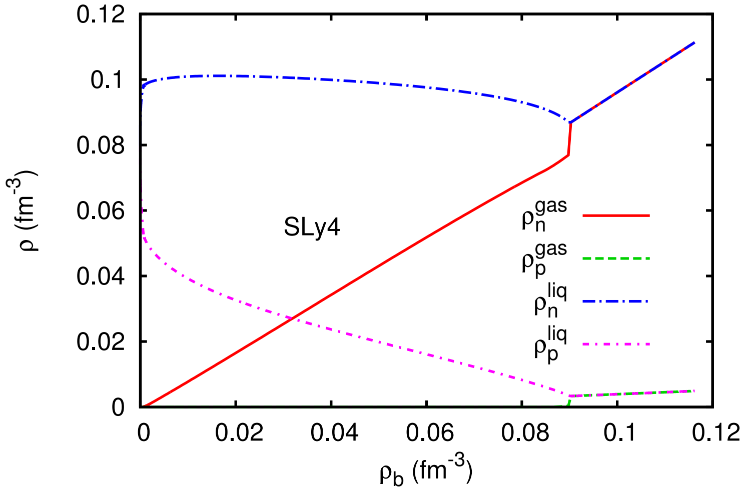

(a) SLy4

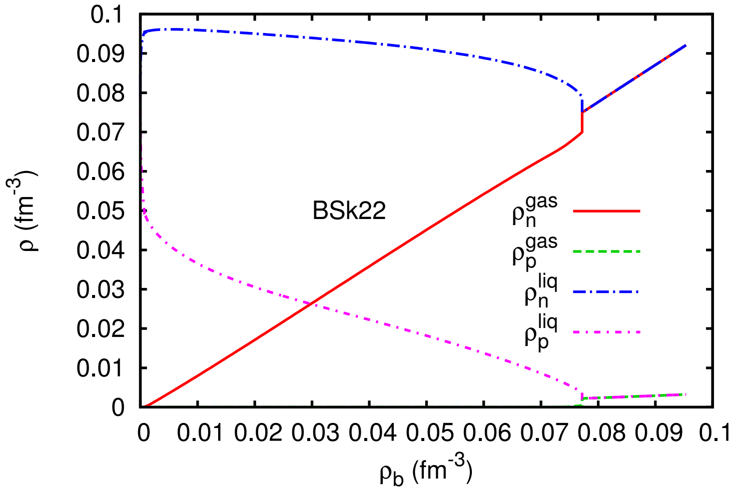

(b) BSk22

Figure 6.1: Neutron and proton densities in the coexisting liquid (droplets) and gas phases, calculated with the Skyrme parameterizations SLy4 and BSk22.

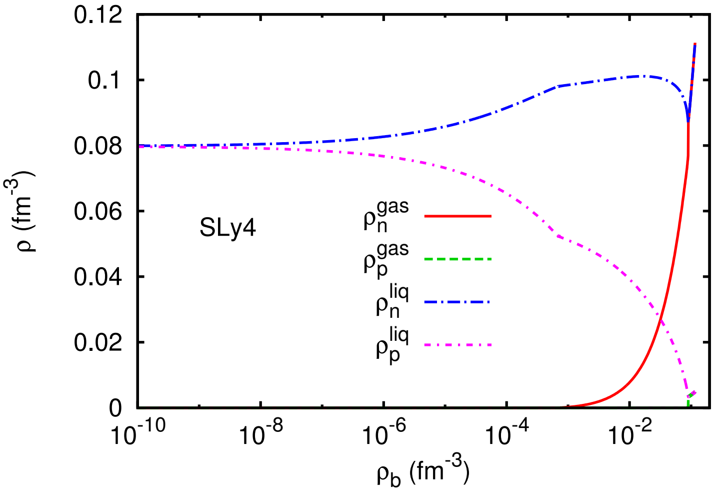

(a) SLy4

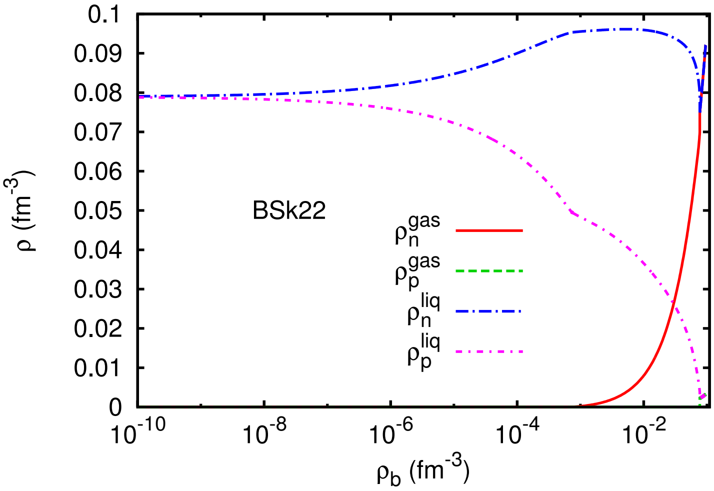

(b) BSk22

Figure 6.2: Same as Fig. 6.1 but with a logarithmic scale for the baryon density.

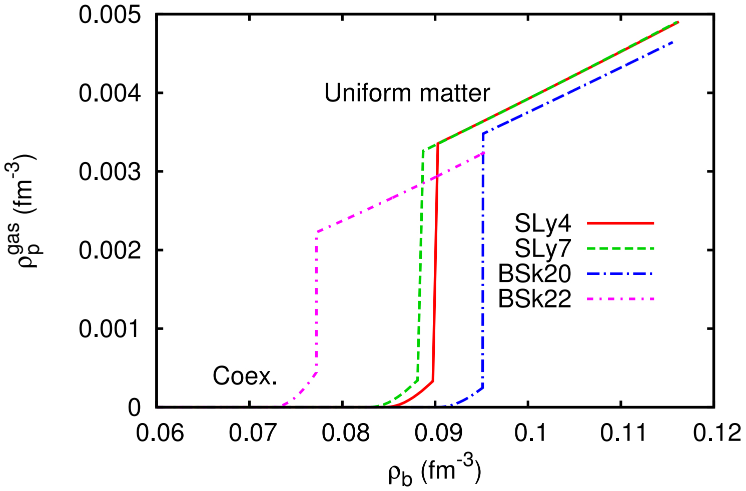

Figure 6.3: Proton density in the gas phase (and later in uniform matter) as function of the total baryon density calculated within the phase coexistence approach using the SLy4, SLy7, BSk20 and BSk22 Skyrme parametrizations.

Close to the transition to uniform matter, also μ_p becomes positive and the gas phase does not only contain neutrons, but also a small amount of protons. Figure 6.3 zooms on densities where protons are present in the gas. Note that the proton density in the gas is always very low, less than 10^{-3} fm^{-3} for all Skyrme parametrizations, compared to the other densities calculated in the phase coexistence framework.

6.2 Energy minimization

In the preceding section, we treated the inner crust as two nuclear fluids in phase coexistence. As already mentioned in Sec. 5.3, this approach misses surface and Coulomb effects, which are included in the minimization of the thermodynamic potential with respect to the parameters of the density profile given in Eq. (5.16). Actually, we perform the minimization for each of the three different geometries discussed in Sec. 5.3, namely spheres (3D), rods (2D), and slabs (1D). Let us remind that we restrict our minimization to 9 parameters as discussed in Sec. 5.3.2. The geometry giving the lowest thermodynamic potential should be the one that is physically realized.

From now on, we restrict ourselves to the range $\mu_n > 0$ corresponding to the inner crust and show the results as functions of the average baryon

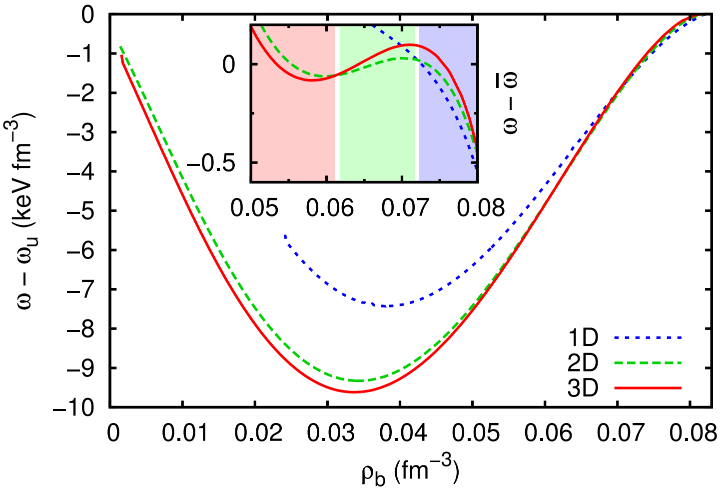

Figure 6.4: The thermodynamic potential ω as function of the baryon density ρ_b, with the thermodynamic potential ω_u of uniform matter subtracted. In the inset, a phenomenological function $\overline{\omega}$ is subtracted, which approximates the average behavior of the three ω's. The SLy4 interaction was used in this calculation.

density $\rho_b = A/V_{\text{WS}}$, where $A = N + Z$ is the total number of nucleons in the WS cell. Figure 6.4 displays the difference $\omega - \omega_u$ between the thermodynamic potentials ω in 3D, 2D, and 1D geometry, obtained by numerical minimization with the SLy4 interaction, and the thermodynamic potential ω_u of uniform npe matter in β-equilibrium with the same baryon density. The difference is negative, confirming that the inhomogeneous phase is favored over uniform matter in this density range. In order to make the differences between the 3D, 2D, and 1D geometries better visible, we subtract in the inset a purely phenomenological function $\bar{\omega}$ which approximates the average behavior of the three ω's. At densities below 0.061 fm^{-3}, the most favorable phase is the crystal (3D). From 0.061 to 0.073 fm^{-3} the preferred phase are the rods (“spaghetti”, 2D). Finally between 0.073 and 0.081 fm^{-3} we find the slabs (“lasagne”, 1D), until the system transforms into uniform matter. In contrast to other work [Ravenhall et al., 1983, Hashimoto et al., 1984, Lassaut et al., 1987, Oyamatsu, 1993, Pais et al., 2014, Pais et al., 2015], we did not find “inverted” geometries such as tubes and bubbles (“Swiss cheese”), which would correspond to $\rho_q^{\text{gas}} > \rho_q^{\text{liq}}$ in the parametrization (5.16) of the density profile in 2D and 3D, respectively.

Let us note that the energy differences between the three geometries are extremely small compared to the total energy, especially between 2D and 3D

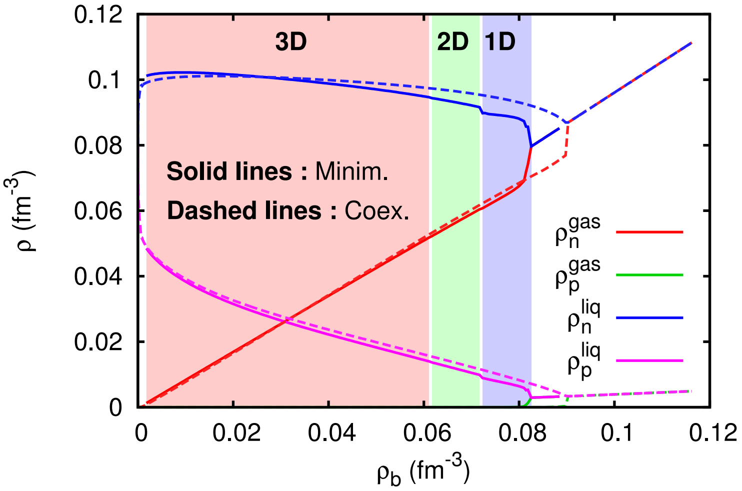

Figure 6.5: Solid lines: densities in the cluster (ρ_q^{liq}) and in the gas (ρ_q^{gas}) corresponding to the geometry (3D, 2D, 1D, or uniform matter) that minimizes ω in Fig. 6.4, obtained by the minimization of the SLy4 functional. Dashes: results obtained within the phase coexistence approach as in Fig. 6.1 but with the SLy4 interaction.

beyond ~ 0.05 fm^{-3}, so that one may expect coexistence of different geometries. This is because, in contrast to some other studies of the pasta phases, we do not consider a fixed proton fraction, but β-equilibrium. As pointed out in Ref. [Piekarewicz and Sánchez, 2012], the small proton fraction (see below) corresponding to β-equilibrium is very unfavorable for the formation of pasta phases.

Our method results necessarily in first-order phase transitions between the different geometries. In reality, however, it might happen that the system passes continuously from one phase to another, e.g., by deforming the nuclei in the 3D phase before they merge into rods [Ravenhall et al., 1983, Lattimer and Swesty, 1991].

The densities ρ_q^i in the favored geometry obtained by the minimization are displayed in Fig. 6.5 as the solid lines. We notice a discontinuity at the transition from 2D to 1D. It is due to the first-order phase transition mentioned above (the corresponding jump between 3D to 2D is too small to be seen on the figure). For comparison, the dashed lines in Fig. 6.5 were calculated as in Fig. 6.1 within the phase coexistence framework. The densities obtained within both approaches are quite similar, which means that even with Coulomb and surface effects, the mechanical and chemical equilibrium, Eqs. (5.5) and (5.6), are approximately satisfied for the densities

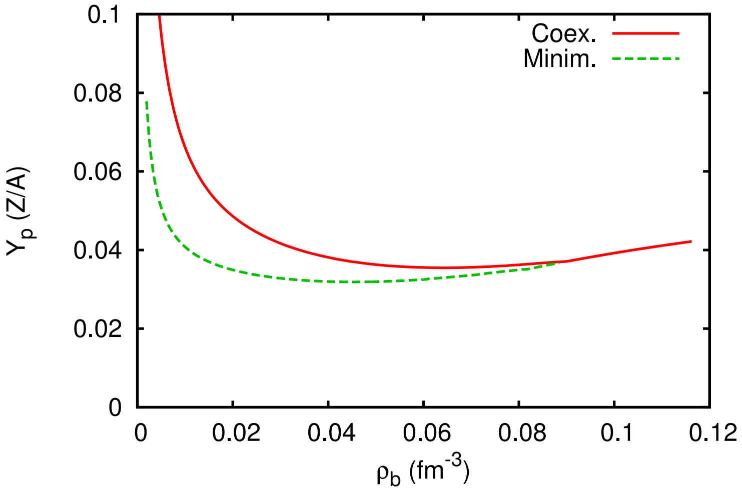

Figure 6.6: Proton fraction Y_p as function of the baryon density ρ_b. The proton fraction is computed using the SLy4 interaction with the phase coexistence (solid line) and the energy minimization (dots) approach.

in the cluster and in the gas away from the interface. The main difference is the transition density from the inner crust to uniform matter, i.e., to the neutron star core. Since Coulomb and surface effects favor uniform matter, the transition happens earlier (i.e., at lower ρ_b) in the minimization than in the phase coexistence approach.

Although the differences in the densities are small, they have a sizable effect on the proton fraction $Y_p = Z/A$. This can be seen in Fig. 6.6, where we compare the proton fractions obtained within the phase coexistence approach (solid lines) and by energy minimization (dashes). It appears that at low baryon density, the proton fraction obtained by minimizing the energy is significantly lower than in the phase coexistence picture, although the proton densities in the liquid are very close (cf. Fig. 6.5). A very similar difference between the two approaches is observed in the Relativistic Mean-Field (RMF) framework [Avancini et al., 2008]. This disagreement can be traced back to the tiny difference in ρ_n^{gas} due to the small Coulomb and surface corrections to the chemical and mechanical equilibrium. Since in this region the total density is dominated by the density of the gas, $\rho_b \approx \rho_n^{\text{gas}}$, and the volume fraction u is approximately proportional to the difference $\rho_B - \rho_n^{\text{gas}}$, the quantities u and consequently also Y_p are very sensitive to small deviations of ρ_n^{gas}.

The proton fractions obtained by energy minimization are similar to those obtained by Pearson et al. [Pearson et al., 2014] within the Hartree-

Fock-Bogoliubov (HFB) model with BSk interactions. However, in contrast to the HFB model, the ETF approximation does not include shell effects. Therefore, our proton number in the 3D phase varies smoothly from $Z \approx 34$ at low baryon density to $Z \approx 26$ at the transition to the 2D phase, while the HFB model gives $Z = 40$ in the whole inner crust except in the case of the BSk22 interaction where Z jumps from 40 to 20 at $\rho_b = 0.035$ fm^{-3} [Pearson et al., 2014].

6.3 Properties of the liquid-gas interface

Let us discuss in some more detail the properties of the liquid-gas interface obtained by energy minimization. To that end, we have to compare our WS cell with a reference system containing a cluster with constant densities ρ_q^{liq} and a sharp surface, surrounded by a gas with constant densities ρ_q^{gas}. The presence of a neutron skin $s_n = r_n - r_p > 0$ complicates this comparison, and we follow [Douchin et al., 2000] who discussed this problem in detail.

We define the radius r_p^{eff} of the reference cluster in such a way that it contains the same number of protons as the actual WS cell, i.e.,

$$(\rho_p^{\mathrm{liq}} - \rho_p^{\mathrm{gas}}) V_d(r_p^{\mathrm{eff}}) + \rho_p^{\mathrm{gas}} V_{\mathrm{WS}} = Z \tag{6.2}$$

($\rho_p^{\mathrm{gas}} = 0$ in most cases, except near the crust-core transition, cf. Fig. 6.5). Note that r_p^{eff} coincides with r_p in the case $d = 1$, but not in the cases $d = 2$ or 3. If we used an asymmetric surface (see discussion below Eq. (5.16)), r_p^{eff} would differ from r_p also in the case $d = 1$.

Since we define the reference cluster with a common surface at r_p^{eff} for protons and neutrons, i.e., without neutron skin, the reference system contains less neutrons than the actual WS cell. Therefore, rather than comparing the energies of two systems having different numbers of particles, one should compare their thermodynamic potentials. The surface contribution to the thermodynamic potential, Ω_s, is defined as the change in Ω (excluding Coulomb) with respect to the "bulk" thermodynamic potential (i.e., excluding gradient terms) of the reference cluster. We denote $V^{\mathrm{liq}} = V_d(r_p^{\mathrm{eff}})$ the volume of the reference cluster and $V^{\mathrm{gas}} = V_{\mathrm{WS}} - V^{\mathrm{liq}}$ the volume of the surrounding gas. Then the surface potential can be written as

$$\begin{aligned}\Omega_s = &E_{\mathrm{Sk}} - \mu_n N - \mu_p Z \\ &- V^{\mathrm{liq}}(\epsilon_{\mathrm{Sk}}^{\mathrm{liq}} - \mu_n \rho_n^{\mathrm{liq}} - \mu_p \rho_p^{\mathrm{liq}}) \\ &- V^{\mathrm{gas}}(\epsilon_{\mathrm{Sk}}^{\mathrm{gas}} - \mu_n \rho_n^{\mathrm{gas}} - \mu_p \rho_p^{\mathrm{gas}}),\end{aligned} \tag{6.3}$$

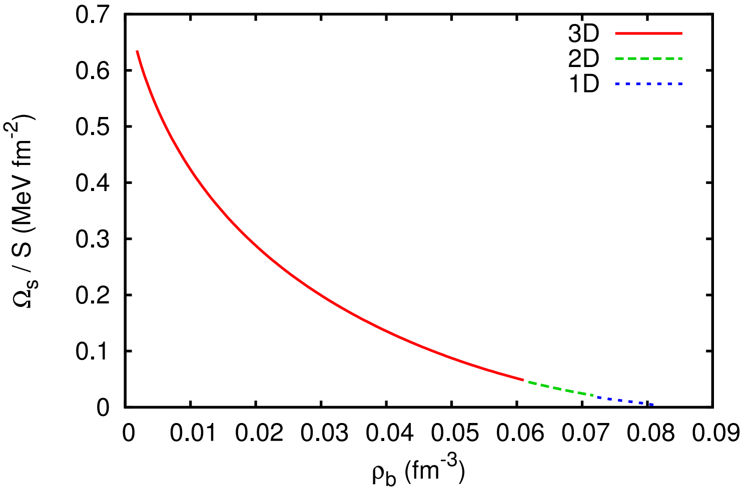

Figure 6.7: The surface tension $\sigma = \Omega/S$ as a function of the baryon density ρ_b. For each ρ_b, the result corresponding to the most favored geometry is displayed.

where ϵ^i_{Sk} is the energy density obtained with the Skyrme functional $\mathscr{E}_{\text{Sk}}$ in the case of uniform matter with densities ρ^i_n and ρ^i_p.

Analogously to Eq. (6.2), we define an effective neutron radius r^{eff}_n, and an effective volume of the neutron skin $V_s = V_d(r^{\text{eff}}_n) - V_d(r^{\text{eff}}_p)$. Then the number of neutrons in the skin, N_s, is given by

$$N_s = V_s(\rho^{\text{liq}}_n - \rho^{\text{gas}}_n), \tag{6.4}$$

and Eq. (6.3) can be rewritten as

$$\Omega_s = E_{\text{Sk}} - V^{\text{liq}}\epsilon^{\text{liq}}_{\text{Sk}} - V^{\text{gas}}\epsilon^{\text{gas}}_{\text{Sk}} - \mu_n N_s\,. \tag{6.5}$$

Finally, the surface energy E_s is given by $E_s = \Omega_s + \mu_n N_s$ [Douchin et al., 2000].

The surface tension is approximately given by $\sigma = \Omega_s/S_d(r^{\text{eff}}_p)$, where $S_d(r)$ is defined in Eq. (5.19). Although $V_d(r)$ and $S_d(r)$ have the dimensions of a volume and of an area only in the case $d = 3$, the ratio $\Omega_s/S_d(r^{\text{eff}}_p)$ is always an energy per area. Note that the above definition of the surface tension is only exact in 1D or if the cluster radius is so large that curvature effects can be neglected. In Fig. 6.7 we display the surface tension. We see that it decreases with increasing ρ_b. This is not surprising because with increasing ρ_b the densities in the gas and in the liquid get closer to each other.

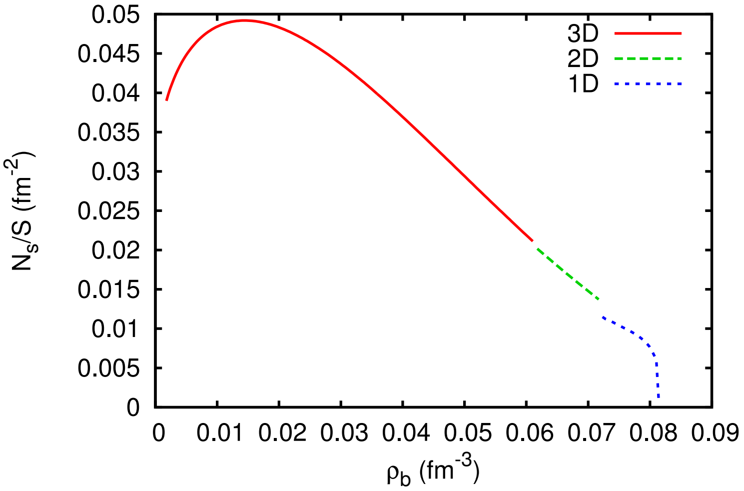

Figure 6.8: The number of the additional neutrons due to the skin, N_s, divided by the cluster surface $S_d(r_p^{\text{eff}})$.

In the low-density limit, where we have essentially isolated nuclei, our surface tension is consistent with the surface energy in the Bethe-Weizsäcker semi-empirical mass formula from which one obtains $\sigma = 1.03$ MeV fm^{-2} [Ring and Schuck, 1980]. Our surface tension is similar to the RMF results shown in Fig. 6(c) of [Avancini et al., 2008].

Another interesting quantity is the number of additional neutrons in the skin. Again, we normalize it to the surface and display in Fig. 6.8 the number of skin neutrons per unit surface, $N_s/S_d(r_p^{\text{eff}})$. We observe that, after a maximum at $\rho_b \sim 0.014$ fm^{-3}, the number of neutrons in the skin decreases with increasing baryon density, although the skin thickness remains about $s_n \sim 0.45$ fm, because the density difference $\rho_n^{\text{liq}} - \rho_n^{\text{gas}}$ decreases. Note that, compared to the total number of neutrons in the WS cell, the number of neutrons in the skin is very small: for instance, for $\rho_b = 0.02$ fm^{-3} there are about 800 neutrons in the cell, 200 in the cluster, and only 23 in the skin.

6.4 Conclusions

In this chapter we compared the results obtained for the inner crust within a simple phase-coexistence picture with results of the minimization of the energy with respect to the density profile. We used Skyrme interactions and the ETF approximation to calculate the energy. Both approaches give similar results for the neutron and proton densities in the clusters and in the gas, despite the Coulomb and surface effects included in the minimization but not in the phase coexistence.

However the phase-coexistence picture is insufficient to predict the cluster sizes and transitions between different geometries, since these result from the competition of Coulomb and surface energies not included in the phase coexistence. With increasing baryon density, we find crystals, rods and plates, but no “inverted” geometries such as tubes and bubbles. Because of the small proton fraction in β- equilibrium, the energy differences between the different geometries are extremely small. Another effect of Coulomb and surface energies is to shift the crust-core transition to lower baryon density.

Although the densities obtained by energy minimization do not present strong deviations from those of the phase coexistence, the proton fraction does, especially at low baryon densities. The small corrections to mechanical and chemical equilibrium due to Coulomb and surface effects slightly modify the density of the neutron gas, resulting in a considerable reduction of volume and proton fractions. The proton fractions obtained within the minimization are similar to HFB results in the literature [Pearson et al., 2014], although shell effects, which are present in HFB, are missing in the ETF approximation to the energy.

The minimization allowed us to calculate the surface tension and the number of skin neutrons in the cluster surface. These results can be used to improve the hydrodynamic description of collective modes in the inner crust similar to the ones of Refs. [Di Gallo et al., 2011, Magierski and Bulgac, 2004b] but including Coulomb and surface effects. The hydrodynamic description will be extensively detailed in the following Part IV.

Part IV

Entrainment of superfluid neutrons and application to glitches

Chapter 7

Superfluid hydrodynamics

7.1 Introduction

The inner crust of neutron stars is characterized by the presence of clusters in a more dilute and superfluid gas of unbound neutrons, cf. Chapter 6. The clusters, containing protons and neutrons, form probably a periodic lattice in order to minimize the Coulomb energy. The superfluid component of the crust can have potentially observable consequences for the hydrodynamical and thermodynamical properties of the crust [Page and Reddy, 2012]. It is therefore important to know the density of effectively free neutrons. This is a non-trivial problem because even the unbound neutrons might be "entrained" by the clusters because of their interactions. This entrainment effect has already been extensively discussed in the literature, e.g., in the framework of a band-structure theory for neutrons developed by N. Chamel and co-workers [Carter et al., 2005, Chamel, 2006, Chamel, 2012].

The entrainment has also a strong effect on the heat transport properties of the crust, and consequently on the cooling of the star, through a modification of the speed of lattice and superfluid phonons [Chamel et al., 2013b, Kobyakov and Pethick, 2013]. These have been discussed in the framework of an effective theory for low-energy, long-wavelength excitations [Cirigliano et al., 2011]. A long wavelength means in this context a wavelength that is large compared to the periodicity of the crystalline structures in the crust. This effective theory has a couple of parameters that have to be determined from more microscopic approaches. Among these parameters are the effective masses of the clusters, or, equivalently, the superfluid density.

However, under the assumption that pairing is sufficiently strong, superfluid hydrodynamics can also be applied on length scales that are smaller than the periodicity of the crystalline structures. This idea was used in [Sedrakian, 1996, Magierski and Bulgac, 2004a, Magierski and Bulgac, 2004b, Magierski, 2004] to estimate the effective mass of an isolated cluster immersed in a neutron gas, and more recently also to describe collective modes in the so-called “lasagne” phase in the deepest layers of the inner crust [Di Gallo et al., 2011, Urban and Oertel, 2015]. In the present work, we apply this superfluid hydrodynamics approach also to the crystalline and “spaghetti” phases.

7.2 Superfluid gas properties

7.2.1 Pairing gap

The dilute neutron gas surrounding the nuclear cluster is assumed to be superfluid. Therefore, low-energy excitations correspond to collective motion of Cooper pairs, see Chapter 3. Let us define the superfluid order parameter (gap)

$$\Delta(\mathbf{r}) = -|g| \langle \Psi_0 | \psi_\uparrow(\mathbf{r}) \psi_\downarrow(\mathbf{r}) | \Psi_0 \rangle \,, \tag{7.1}$$

with $|\Psi_0\rangle$ the BCS ground state (2.16) and $\psi_\sigma(\mathbf{r})$ the field operators (C.3) for both spin projections $\sigma = (\uparrow, \downarrow)$ up and down respectively. We use a contact interaction for the pairing interaction of strength $|g|$ and neglect the UV divergence.

However, the preceding equation is written for a static situation and can be extended to a uniform flow of Cooper pairs with velocity $\mathbf{v}_n$, which is fully detailed in Apx. C.2. We apply a boost of momentum $\mathbf{q} = m\mathbf{v}_n$ to the particles

$$a_\mathbf{k} \rightarrow a_{\mathbf{k}+\mathbf{q}} \quad \text{and} \quad a_{-\mathbf{k}} \rightarrow a_{-\mathbf{k}+\mathbf{q}} \,. \tag{7.2}$$

In this case we denote the boosted quantities with a *tilde*, thus the BCS ground state reads as:

$$\left|\widetilde{\Psi}_0\right\rangle = \prod_\mathbf{k} \frac{1}{v_k} \tilde{\alpha}_\mathbf{k} \tilde{\beta}_{-\mathbf{k}} |0\rangle \,, \tag{7.3}$$

with $\tilde{\alpha}_\mathbf{k}$ and $\tilde{\beta}_{-\mathbf{k}}$ the Bogoliubov operators boosted by a momentum $\mathbf{q}$ and defined in Eq. (C.12). In consequence, the pairing gap rewrites:

$$\Delta(\mathbf{r}) = -|g| \left\langle \widetilde{\Psi}_0 \right| \psi_\uparrow(\mathbf{r}) \psi_\downarrow(\mathbf{r}) \left| \widetilde{\Psi}_0 \right\rangle . \tag{7.4}$$

After computing the expectation value above, and thanks to definition of the Bogoliubov operators, it reduces to

$$\Delta(\mathbf{r}) = |g| e^{2i\mathbf{q}\cdot\mathbf{r}} \sum_\mathbf{p} u_p v_p \,, \tag{7.5}$$

with u_p and v_p the variational parameters of the BCS theory, cf. Chap.2. Finally, the superfluid order parameter is written as

$$\Delta(\mathbf{r}) = |\Delta| e^{i\varphi(\mathbf{r})}, \tag{7.6}$$

the velocity field of the neutron pairs is related to the phase $\varphi(\mathbf{r})$ by

$$\mathbf{v}_n(\mathbf{r}) = \frac{1}{2m}\nabla\varphi(\mathbf{r}), \tag{7.7}$$

where m denotes the neutron mass.[1] In the limit of zero temperature, and if one excludes pair breaking, this leads to the equations of superfluid hydrodynamics as discussed in Refs. [Urban and Schuck, 2006, Tonini et al., 2006] in the context of ultracold atoms. Let us also mention that, again in the context of ultracold atoms, a calculation in quasiparticle random-phase approximation (QRPA) [Grasso et al., 2005] showed that the collective modes can be described by hydrodynamics if $|\Delta|$ becomes much larger than the spacing of the discrete single-particle levels in the trap potential.

7.2.2 Limitations

In uniform neutron matter, the QRPA shows that the hydrodynamic behavior of the oscillations of the phase φ (Goldstone or Bogoliubov-Anderson mode) is well fulfilled as long as the excitation energy stays well below the two-quasiparticle (pair breaking) threshold as shown in Chap. 4. In the non-uniform inner crust, one in addition has to assume that the coherence length ξ of the Cooper pairs is small compared to the size of the inhomogeneities. Of all the assumptions, this is probably the most critical one, especially inside the dense clusters of the inner crust. However, as discussed in Ref. [Di Gallo et al., 2011], as long as the excitation does not involve Fermi surface deformation, the hydrodynamic approach remains reasonable even in the absence of pairing inside the cluster. Furthermore, QRPA calculations of collective modes of a cluster in a spherical Wigner-Seitz (WS) cell predicted the appearance of "supergiant" resonances that could be interpreted as hydrodynamic Bogoliubov-Anderson modes in the volume of the cell [Khan et al., 2005].

In a non-uniform system, hydrodynamics is valid if the coherence length ξ of the Cooper pairs is small compared to the size of the inhomogeneities. As we show in Fig. 7.1, the Cooper pair size ξ in the neutron gas is indeed

---

[1] In contrast to Refs. [Di Gallo et al., 2011, Urban and Oertel, 2015] we neglect here the "microscopic" entrainment of neutrons by protons in the liquid phase. It should be included in future studies.

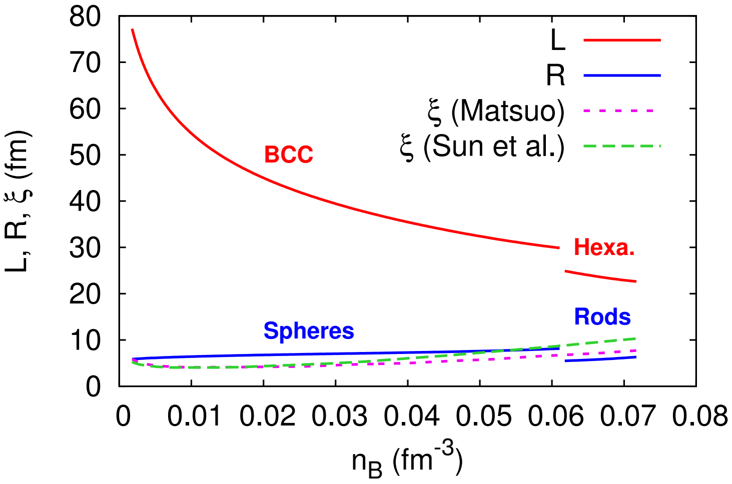

Figure 7.1: Root mean square radius ξ of the Cooper pair in the neutron gas (dashed lines) compared with the cell size L of the crystalline lattice (red solid line) and the cluster radius R (blue solid line) as functions of the total baryon density n_B in the inner crust. The neutron gas density $n_{n,1}$ and the shown results for L and R were obtained from calculations detailed in Part III. The results for ξ as functions of $n_{n,1}$ were obtained respectively in Ref. [Matsuo, 2006] using the Gogny force (purple short dashes) and in Ref. [Sun et al., 2010] using the Bonn potential (green long dashes) as pairing interactions.

much smaller than the size L of the unit cell of the crystalline lattice. At higher densities, where one expects the pasta phases, the comparison would be somewhat less favorable. However, the main problem is the small size of the clusters, whose radii R are as small as ξ.

The condition $\xi \ll R$ for the validity of hydrodynamics was already mentioned in Migdal's seminal work [Migdal, 1959] in which he explained the nuclear moments of inertia in the framework of the theory of superfluidity. Since the coherence length ξ and the nuclear radius R are of the same order of magnitude, rotating nuclei exhibit a combination of irrotational and rotational flow. Nevertheless, the nuclear moments of inertia are slightly closer to the irrotational (hydrodynamic) than to the rigid-body limit (see Fig. 8.2 in Ref. [Rowe, 1970]).

In analogy to this observation, we expect that probably our superfluid hydrodynamic model for the inner crust should give the right picture, although it might probably overestimate the superfluid flow inside (and close to) the clusters. We refer to Sec. 8.3 for a further discussion of this problem and possible solutions.

7.3 Hydrodynamics in the inner crust

7.3.1 Context

Let us briefly recall the simple hydrodynamic model of Refs. [Magierski and Bulgac, 2004a, Magierski and Bulgac, 2004b, Magierski, 2004, Urban and Oertel, 2015]. We assume that the clusters have constant neutron and proton densities $n_{n,2}$ and $n_{p,2}$ and a sharp surface separating them from the neutron gas, whose density $n_{n,1}$ is also constant, as displayed in Fig. 7.2. The densities have to satisfy the conditions of phase equilibrium (equal chemical potentials and pressure in both phases, i.e., the phase coexistence), which is actually a very good approximation (see Chap. 6) In the limit of small velocities, the size and shape of the clusters themselves as well as the densities in the clusters and in the gas do not change. We define the cluster surface as the surface of the sphere (3D) or rod (2D) of radius R_p containing the protons . Hence, the velocity of the clusters is equal to the velocity of the protons, $\mathbf{u}_p$. The neutrons, however, can pass through the cluster surface, and their velocity field $\mathbf{v}_n(\mathbf{r})$ is not uniform, since the neutrons of the gas somehow have to flow around or through the clusters.

Here, we focus on macroscopic (long wavelength) motion. In this case, the relative velocity between the clusters and the gas varies only on length

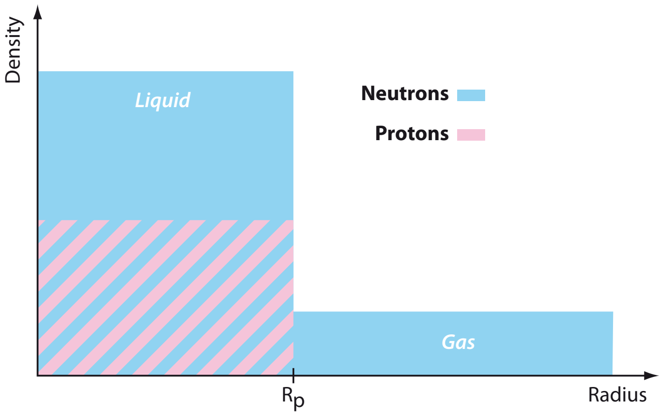

Figure 7.2: Schematic view of the cluster densities in the hydrodynamic model. The boundary between the liquid and the gas is materialized by the density step at R_p, which is the radius of the sphere or of the rod, in 3D or 2D case respectively.

scales that are much larger than the periodicity of the lattice. So, the properties of the flow inside a cell are identical to those of the entire flow. Furthermore, the long wavelength assumption excludes density waves (incompressible gas) and deformations of the cluster surface.

7.3.2 Boundary conditions

Now, let us concentrate on the neutron flow induced by the uniform flow of clusters. As mentioned in Sec. 7.2, the superfluidity of the neutron gas allows us to introduce a velocity potential $\phi = \varphi/(2m)$. Since the densities remain constant, we have $\nabla \cdot \mathbf{v}_n = 0$, i.e.,

$$\triangle \phi = 0 \,. \tag{7.8}$$

This equation is true in both phases, but it has to be complemented with suitable boundary conditions at the phase boundaries.

In Refs. [Sedrakian, 1996, Di Gallo et al., 2011], the phase boundary was treated as impermeable. However, this is not realistic, since neutrons inside and outside the cluster are indistinguishable and nothing prevents them from moving from the gas into the cluster or vice versa. The permeability of the phase boundary was included in the boundary conditions introduced by Magierski and Bulgac [Magierski and Bulgac, 2004a, Magierski and Bulgac, 2004b, Magierski, 2004]. Analogous boundary conditions were given in Ref. [Lazarides and Van Schaeybroeck, 2008] for a phase boundary in the context of ultracold atoms. They were also used in Ref. [Urban and Oertel, 2015] to describe collective modes in the "pasta" phases of the neutron-star crust.

First, the phase of the order parameter is continuous across the phase boundary, i.e.,

$$\phi_1 = \phi_2 \,, \tag{7.9}$$

where 1 and 2 refer to the limits of $\mathbf{r}$ approaching the interface from outside or inside the cluster, respectively. This boundary condition implies that the neutron velocity tangential to the interface is continuous, too.

Second, the neutron current crossing the interface conserves the particle number. Since the interface itself moves with velocity $\mathbf{u}_p$, this condition reads

$$n_{n,1}(\nabla\phi_1 - \mathbf{u}_p)\cdot\mathbf{S} = n_{n,2}(\nabla\phi_2 - \mathbf{u}_p)\cdot\mathbf{S} \,, \tag{7.10}$$

where $\mathbf{S}$ is the normal vector to the surface, pointing outwards.

So far, the boundary conditions are the same as in Ref. [Magierski and Bulgac, 2004a, Magierski and Bulgac, 2004b, Magierski, 2004], where the motion of a spherical nucleus in an infinite neutron gas was studied. In this case, Eqs. (7.8)–(7.10) can be solved analytically (see Sec. 7.5). However, except in the case of plates (1D), this is no longer true if one considers a periodic lattice of clusters.

To treat the periodicity, we introduce a primitive cell $\mathscr{C}$ spanned by the D primitive vectors $\mathbf{a}_i$ ($i = 1,\dots,D$) of the Bravais lattice, where $D = 3$ in the case of a crystal, $D = 2$ in the case of rods (spaghetti phase), and $D = 1$ in the case of plates (lasagne phase). Depending on the lattice structure, the primitive cell contains one or two clusters (see Sec. 7.7). While the velocity field $\mathbf{v}_n(\mathbf{r})$ is periodic,

$$\mathbf{v}_n(\mathbf{r} + \mathbf{a}_i) = \mathbf{v}_n(\mathbf{r}) \,, \tag{7.11}$$

the velocity potential itself can in general be the sum of a periodic and a linear function. The linear function can be written as $\mathbf{u}_n \cdot \mathbf{r}$, where $\mathbf{u}_n$ is the spatially averaged neutron velocity, which coincides with the velocity of the *superfluid* neutrons [Pethick et al., 2010, Kobyakov and Pethick, 2013] or *conduction* neutrons [Chamel et al., 2013b]. Note that $\mathbf{u}_n$ is different from the average neutron velocity $\bar{\mathbf{v}}_n$, which is defined via the spatially averaged neutron current (see below). Without loss of generality, let us choose the frame of reference such that $\mathbf{u}_n = 0$. In this frame, also the velocity potential is periodic,

$$\phi(\mathbf{r} + \mathbf{a}_i) = \phi(\mathbf{r}) \,. \tag{7.12}$$

7.3.3 Physical quantities of the flow

From the function $\phi(\mathbf{r})$ in the primitive cell one can derive the macroscopic (coarse grained) neutron current $\bar{\mathbf{j}}_n$ by averaging over the volume of the cell, $V_{\mathscr{C}}$:

$$\bar{\mathbf{j}}_n = \frac{1}{V_{\mathscr{C}}} \int_{\mathscr{C}} dV\, n_n(\mathbf{r}) \nabla\phi(\mathbf{r}). \tag{7.13}$$

Because of the uniform densities, the integral can be split into two parts:

$$\bar{\mathbf{j}}_n = \frac{1}{V_{\mathscr{C}}} \left[n_{n,1} \int_{\mathscr{C}_1} dV\, \nabla\phi(\mathbf{r}) + n_{n,2} \int_{\mathscr{C}_2} dV\, \nabla\phi(\mathbf{r}) \right], \tag{7.14}$$

with $\mathscr{C}_i$ the volume of the phase $i = (1,2)$ outside or inside the cluster, respectively. Let us remind the divergence theorem

$$\int_V dV\, \nabla f(\mathbf{r}) = \oint_S d\mathbf{S}\, f(\mathbf{r}), \tag{7.15}$$

with the volume V and the surface S of integration for an arbitrary function $f(\mathbf{r})$. By applying the previous theorem to Eq. (7.14) one has

$$\bar{\mathbf{j}}_n = \frac{1}{V_{\mathscr{C}}} (n_{n,2} - n_{n,1}) \oint_\Omega d\mathbf{S}\, \phi(r), \tag{7.16}$$

where Ω is the surface of the cluster(s) in the cell. The integral over the cell boundary vanishes because of the periodicity of ϕ. The negative sign in front of $n_{n,1}$ comes from the direction of the normal vector with respect to the surface.

Similarly, one can calculate the average kinetic energy density

$$\mathscr{E}_{\mathrm{kin},n} = \frac{m}{2V_{\mathscr{C}}} \int_{\mathscr{C}} dV\, n_n(\mathbf{r}) [\nabla\phi(r)]^2. \tag{7.17}$$

Using the Gauss theorem and Eq. (7.10), this expression can be simplified to [Magierski and Bulgac, 2004a]

$$\mathscr{E}_{\mathrm{kin},n} = \frac{m}{2V} (n_2 - n_1) \oint_\Omega d\mathbf{S} \cdot \mathbf{u}_p \phi(\mathbf{r}) = \frac{m}{2} \mathbf{u}_p \cdot \bar{\mathbf{j}}_n. \tag{7.18}$$

7.4 Entrainment

In Eq. (7.12) we assumed that $\mathbf{u}_n = 0$. The solution for ϕ in the general case $\mathbf{u}_n \neq 0$ is related to the periodic solution in the special case $\mathbf{u}_n = 0$ by

$$\Phi(\mathbf{r}; \mathbf{u}_p, \mathbf{u}_n) = \mathbf{r} \cdot \mathbf{u}_n + \phi(\mathbf{r}; \mathbf{u}_p - \mathbf{u}_n, 0). \tag{7.19}$$

The average velocity of neutrons $\bar{\mathbf{v}}_n$ is defined via the average current $\bar{\mathbf{j}}_n$ as

$$\bar{\mathbf{v}}_n = \frac{\bar{\mathbf{j}}_n}{\bar{n}_n}, \tag{7.20}$$

where

$$\bar{n}_n = \frac{V_1}{V_{\mathscr{C}}} n_{n,1} + \frac{V_2}{V_{\mathscr{C}}} n_{n,2} \tag{7.21}$$

denotes the average neutron density with $V_{1,2}$ the volume outside and inside the cluster(s), respectively. The neutron current is now written as

$$\begin{aligned}\bar{\mathbf{j}}_n = \frac{1}{V_{\mathscr{C}}} \int_{\mathscr{C}} dV\, n_n(r) \nabla\Phi(\mathbf{r};\mathbf{u}_p,\mathbf{u}_n) \\ = \bar{n}_n \mathbf{u}_n + \frac{1}{V_{\mathscr{C}}} \int_{\mathscr{C}} dV\, n_n(r) \nabla\phi(\mathbf{r};\mathbf{u}_p - \mathbf{u}_n, 0).\end{aligned} \tag{7.22}$$

Since the last term in Eq. (7.22) is linear in $\mathbf{u}_p - \mathbf{u}_n$, we can write the current in the form

$$\bar{\mathbf{j}}_n = \bar{n}_n \mathbf{u}_n + \underline{\mathbf{n}}_n^b (\mathbf{u}_p - \mathbf{u}_n), \tag{7.23}$$

with a 3 × 3 matrix $\underline{\mathbf{n}}_n^b$. Factorizing Eq. (7.23) with respect to $\mathbf{u}_n$, one sees that $\underline{\mathbf{n}}_n^b$ can be interpreted as the density of bound neutrons, which are entrained by the clusters with velocity $\mathbf{u}_p$, while the superfluid neutrons moving with velocity $\mathbf{u}_n$ have an average density $\underline{\mathbf{n}}_n^s = \bar{n}_n \underline{\mathbf{I}}_3 - \underline{\mathbf{n}}_n^b$. Concerning bound and superfluid neutrons, we follow here the nomenclature of Ref. [Pethick et al., 2010]. Hence, the final expression for the neutron current reads:

$$\bar{\mathbf{j}}_n = \underline{\mathbf{n}}_n^b \mathbf{u}_p + \underline{\mathbf{n}}_n^s \mathbf{u}_n . \tag{7.24}$$

The fact that $\underline{\mathbf{n}}_n^b$ and $\underline{\mathbf{n}}_n^s$ are matrices shows that the proportion of bound neutrons depends in general on the direction of the relative motion between neutrons and protons. This is intuitively clear, e.g., in the case of the 2D rod phase, where neutrons and protons can move independently of each other in the direction parallel to the rods, while this is not the case in the directions perpendicular to the rods. As will be shown in Sec. 7.7.1, $\underline{\mathbf{n}}_n^b$ and $\underline{\mathbf{n}}_n^s$ are proportional to the unit matrix if the lattice has a cubic symmetry.

It is straight-forward to generalize also Eq. (7.18) for the neutron kinetic energy to the general case $\mathbf{u}_n \neq 0$. First, note that in the case $\mathbf{u}_n = 0$, the current simplifies to $\bar{\mathbf{j}}_n = \underline{\mathbf{n}}_n^b \mathbf{u}_p$, and consequently Eq. (7.18) becomes $\mathscr{E}_{\mathrm{kin},n} = (m/2)\mathbf{u}_p^\top \underline{\mathbf{n}}_n^b \mathbf{u}_p$. Starting from Eq. (7.19) and repeating the same steps for the general case $\mathbf{u}_n \neq 0$, one obtains:

$$\mathscr{E}_{\mathrm{kin},n} = \frac{m}{2}\left(\mathbf{u}_n^\top \underline{\mathbf{n}}_n^s \mathbf{u}_n + \mathbf{u}_p^\top \underline{\mathbf{n}}_n^b \mathbf{u}_p\right), \tag{7.25}$$

which agrees with the expression of Chamel and Carter [Chamel and Carter, 2006] if one identifies n_n^b with the neutron *normal* density in their nomenclature.

In summary, the macroscopic entrainment coefficients of the crust are determined by the matrices $\underline{\mathbf{n}}_n^b$ and $\underline{\mathbf{n}}_n^s$ which we can obtain by solving numerically Eqs. (7.8)–(7.12) for the function $\Phi(\mathbf{r};\mathbf{u}_p,0)$.

7.5 Solution for a cluster in infinite matter

In the case of a single cluster (spherical or cylindrical) moving with velocity $\mathbf{u}_p$ through in an infinite and uniform neutron gas, and in the case of a 1D lattice of parallel plates, analytical solutions for the velocity potential can be found.

7.5.1 Spheres

The case of a spherical cluster of radius R was studied in Refs. [Magierski and Bulgac, 2004a, Magierski and Bulgac, 2004b, Magierski, 2004]. We begin with the general solution of the Laplace equation (7.8) in spherical coordinates [Jackson, 1975]

$$\phi_i(\mathbf{r}) = \sum_{l=0}^{\infty}\sum_{m=-l}^{l}\left[A_{lm}\,r^l + B_{lm}\,r^{-(l+1)}\right]Y_{lm}(\theta,\varphi), \tag{7.26}$$

in a phase $i = (1,2)$ outside or inside the cluster, respectively. We denote the spherical harmonics by $Y_{lm}(\theta,\varphi)$. The terms A_{lm} and B_{lm} stand for real coefficients, which will be constrained by the boundary conditions. If we place the origin of the coordinate system in the center of the cluster and suppose that the neutron gas is at rest at infinity ($\phi \to 0$ for $r \to \infty$), one has $A_{lm} = 0$ in phase 1 and $B_{lm} = 0$ in phase 2. Hence, the potential reads as

$$\phi_1(\mathbf{r}) = \sum_{l,m} B_{lm}\,r^{-(l+1)}\,Y_{lm}(\theta,\varphi), \tag{7.27a}$$

$$\phi_2(\mathbf{r}) = \sum_{l,m} A_{lm}\,r^l\,Y_{lm}(\theta,\varphi). \tag{7.27b}$$

Let us account for the radial flow conservation (7.10). We start by integrating the boundary condition over the solid angle in order to exploit the orthogonality properties of the spherical harmonics:

$$\int d\Omega\, Y^*_{l'm'}(\theta,\varphi)\left[n_{n,1}\nabla\phi_1 - n_{n,2}\nabla\phi_2\right]\cdot\mathbf{S} =$$

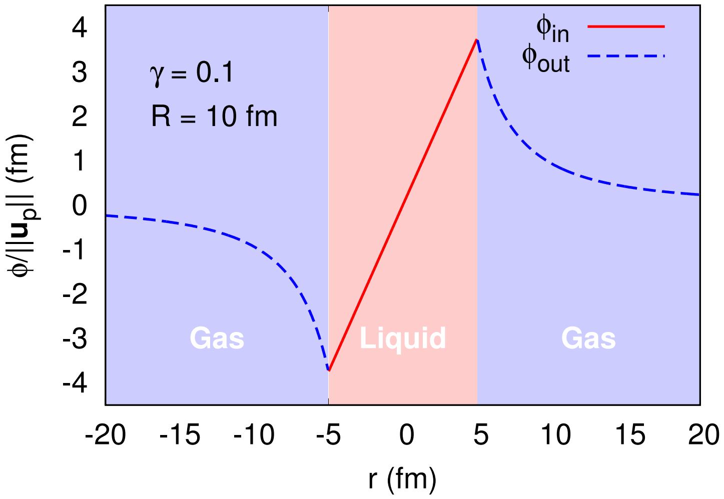

Figure 7.3: Schematic view of the velocity potential ϕ inside and outside the cluster along the axis $\mathbf{e}_x$ for $\mathbf{u}_p = u_p \mathbf{e}_x$. It was obtained for a arbitrary spherical cluster of radius $R = 5$ fm and density ratio $\gamma = 0.1$.

$$(n_{n,1} - n_{n,2}) \int d\Omega\, Y^*_{l'm'}(\theta, \varphi) ||\mathbf{u}_p|| \cos\theta\,, \quad (7.28)$$

with $d\Omega = d\varphi\, d\theta \sin\theta$ and $Y^*_{l'm'}$ the complex conjugate of $Y_{l'm'}$. Let us recall the orthogonality relation satisfied by the spherical harmonics: $\int d\Omega\, Y^*_{l'm'} Y_{lm} = \delta_{l,l'} \delta_{m,m'}$. Hence, by injecting the potential derivatives ($\nabla\phi_1$ and $\nabla\phi_2$) computed from Eqs. (7.27), the equation (7.28) reads as:

$$n_{n,1} B_{lm} (l+1) R^{-(l+2)} + n_{n,2} A_{lm}\, l R^{l-1} = \sqrt{\frac{4\pi}{3}} (n_{n,2} - n_{n,1}) ||\mathbf{u}_p|| \delta_{1,l} \delta_{m,0}\,, \quad (7.29)$$

with $\cos\theta = \sqrt{4\pi/3}\, Y_{10}$. Finally, the solution for the velocity potential is obtained thanks to the continuity of the velocity potential at the cluster surface (7.9)

$$\phi(\mathbf{r}) = \begin{cases} \dfrac{1-\gamma}{1+2\gamma} \mathbf{r} \cdot \mathbf{u}_p & \text{for } r < R\,, \\ \dfrac{R^3}{r^3} \dfrac{1-\gamma}{1+2\gamma} \mathbf{r} \cdot \mathbf{u}_p & \text{for } r \geq R\,, \end{cases} \quad (7.30)$$

where $\gamma = n_{n,1}/n_{n,2}$ is the ratio between the neutron densities in the gas and in the cluster. From this solution, one can compute the total momentum carried by neutrons in the cluster and in the gas. Identifying this momentum with $N_{\text{eff}} m \mathbf{u}_p$, one can define the number N_{eff} of neutrons effectively entrained by the protons of the cluster,

$$N_{\text{eff}} = N_{\text{r-cluster}} \frac{(1-\gamma)^2}{2\gamma+1}\,, \tag{7.31}$$

with

$$N_{\text{r-cluster}} = \frac{4\pi}{3} R^3\, n_{n,2} \tag{7.32}$$

the number of neutrons that are located inside the cluster (in coordinate space, denoted r-cluster following Ref. [Papakonstantinou et al., 2013]). It is interesting to note that $N_{\text{eff}} < N_{\text{r-cluster}}$, i.e., the main effect is not that the cluster entrains neutrons of the gas with it, but rather that the flow of gas neutrons through the cluster surface reduces the speed of the neutrons inside the cluster.

7.5.2 Cylinders

The case of a cylindrical rod moving through an infinite and uniform neutron gas can be treated analogously. Here, the velocity potential is given by

$$\phi(\mathbf{r}) = \begin{cases} \dfrac{1-\gamma}{1+\gamma}\mathbf{r}_\perp \cdot \mathbf{u}_p & \text{for } r_\perp < R\,, \\ \dfrac{R^2}{r_\perp^2}\dfrac{1-\gamma}{1+\gamma}\mathbf{r}_\perp \cdot \mathbf{u}_p & \text{for } r_\perp \geq R\,, \end{cases} \tag{7.33}$$

where $\mathbf{r}_\perp$ is the projection of $\mathbf{r}$ on the plane perpendicular to the symmetry axis of the rod. Since the rod is assumed to be infinite, one can only define N_{eff} and $N_{\text{r-cluster}}$ as numbers per unit length, e.g., $N_{\text{r-cluster}} = \pi R^2 n_{n,2}$. If the proton velocity $\mathbf{u}_p$ is parallel to the rod, the surface of the rod does not move and there is obviously no entrainment. However, for $\mathbf{u}_p$ perpendicular to the rod, the expression of effectively bound (entrained) neutrons reads as

$$N_{\text{eff}} = N_{\text{r-cluster}} \frac{(1-\gamma)^2}{1+\gamma}\,. \tag{7.34}$$

One sees that the number of entrained neutrons is again lower than the number of neutrons geometrically located inside the rod.

7.5.3 Plates

Another case in which an analytic solution can be found is the phase of plates (1D). Let us consider alternating layers of phases 1 and 2 with widths L_1 and

L_2, respectively. We take the layers parallel to the xy plane and choose the unit cell $0 < z < L = L_1 + L_2$ such that the region $0 < z < L_1$ corresponds to phase 1 and $L_1 < z < L$ to phase 2. Obviously the protons can entrain the neutrons only in z direction. In the rest frame of the superfluid neutrons, the solution for the velocity potential reads

$$\phi(\mathbf{r}) = \begin{cases} -\dfrac{1-\gamma}{L_1/L_2+\gamma} z u_{p,z} & \text{for } 0 \leq z \leq L_1 , \\ \dfrac{1-\gamma}{1+\gamma L_2/L_1}(z-L)u_{p,z} & \text{for } L_1 \leq z \leq L . \end{cases} \tag{7.35}$$

From this solution, one can readily obtain the density of bound neutrons (more precisely, the zz component of the matrix $\underline{\underline{\mathbf{n}}}_n^b$; all other components vanish):

$$n^b_{n,zz} = \bar{n}_n \frac{(1-\gamma)^2 L_1 L_2}{(L_1+\gamma L_2)(L_2+\gamma L_1)} . \tag{7.36}$$

In practice, $n^b_{n,zz}$ is much smaller than $\bar{n}_n$ ($n^b_{n,zz}/\bar{n}_n \lesssim 0.03$) because the plates are only found in the deepest layers of the neutron-star crust (as shown in Chap. 6), where the density of the gas is quite large ($\gamma \gtrsim 0.7$).

7.6 Numerical methods

In contrast the case of a single cluster in an infinite gas discussed in Sec. 7.5, we consider from now on finite cells with a periodic lattice arrangement of clusters, in 2D and 3D cases. Because of the complicated geometries of the clusters and of the lattice, the solution of the Laplace equation together with the boundary condition can only be obtained numerically in this case.

7.6.1 Space discretization and periodicity

We start by discretizing the cell space with a regular mesh of N points per row. Note that if the unit cell is not cubic (as in the hexagonal 2D case, see Sec. 7.7), the rows are not orthogonal one to another, as displayed in Fig. 7.4(b). The cluster surface is approximated by a set of N_S points given by the intersections of the mesh lines with the cluster surface. As an example, Fig. 7.4 illustrates two cases: (i) a spherical cluster in a simple cubic cell and (ii) a rod in a hexagonal unit cell. Points belonging to the cell mesh are shown as black circles and blue squares, those belonging to the cluster surface as red diamonds. Because of periodicity, points lying on opposite edges of the cell, shown as blue squares, are equivalent to each other. In total, the

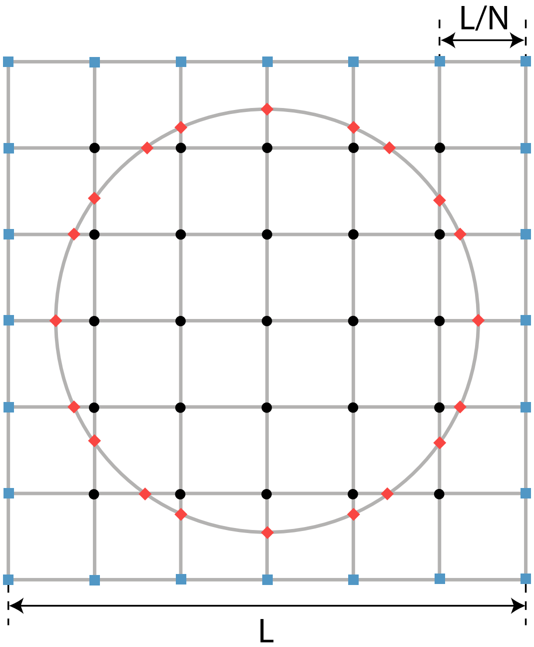

(a) Simple cubic cell and a spherical cluster

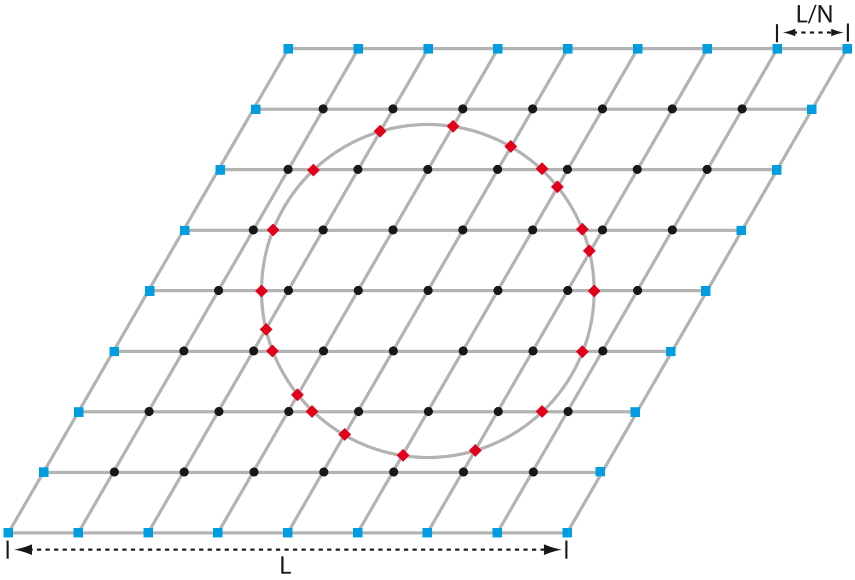

(b) Hexagonal cell and a cylindrical cluster

Figure 7.4: Schematic illustration of the discretization of different cells with a cluster in their center.

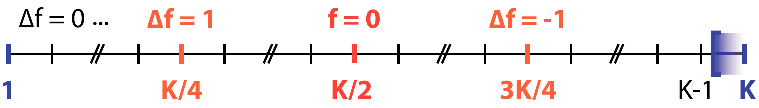

Figure 7.5: One dimensional grid made of K points with charges located at points $K/4$ and $3K/4$.

number of independent points is $\mathcal{N} = N^D + N_S$, with D the dimension of the lattice.

The numerical method for treating the periodicity is well described in Ref. [Evans and Okolie, 1982]. In order to illustrate the periodicity condition, let us consider a simple 1D periodic mesh, as shown in Figure 7.5. The mesh is made of K points, with charges located in points $K/4$ and $3K/4$ which are 1 and -1, respectively, a periodic solution exists only if the sum of the charges is zero. Here, the charges are given without units in order to be schematic. In this case, we propose to solve the Poisson equation in the mesh

$$\Delta f_k = q_k\,, \tag{7.37}$$

with $q_{K/4} = 1$ and $q_{3K/4} = -1$ and all others $q = 0$. The discretization of the mesh allows us to approximate the Laplacian in an arbitrary point k [Evans and Okolie, 1982]:

$$\Delta f_k = \frac{1}{d^2}(f_{k+1} - 2f_k + f_{k-1})\,, \tag{7.38}$$

with $d = x_{k+1} - x_k$ the distance between two neighbor points assumed to be constant. Now the system is made of K equations corresponding to the number of mesh points, however let us recall the periodicity condition which reads as $f_1 = f_K$. Hence, the system of equations to solve reduces to $K-1$ equations. In addition, the Poisson equation is defined up to an additive constant, so that we have to fix the value of f in one of the mesh point, by simplicity we choose the point $f_{K/2} = 0$.

Finally, the Poisson Eq. (7.37) can be rewritten in a matrix form:

$$\underline{\mathbf{C}}\mathbf{f} = \mathbf{q}\,, \tag{7.39}$$

with $\underline{\mathbf{C}}$ the matrix containing the coefficients of the discretized Laplace operator in 1D (7.38). In addition, the values of f_k are contained in the vector $\mathbf{f} = \{f_k\}$, while the right-hand side is contained in $\mathbf{q} = \{q_k\}$. In this way, solving Poisson equation accounts to inverting the matrix $\underline{\mathbf{C}}$, i.e., $\mathbf{f} = \underline{\mathbf{C}}^{-1}\mathbf{q}$. Now, if one accounts for the periodicity of the mesh, the coefficients of the matrix simply read

$$\underline{\mathbf{C}} = \frac{1}{d^2}\begin{pmatrix} -2 & 1 & & & & & 1 \\ 1 & -2 & 1 & & & & \\ & \ddots & \ddots & \ddots & & & \\ & & 0 & 1 & 0 & & \\ & & & \ddots & \ddots & \ddots & \\ & & & & 1 & -2 & 1 \\ 1 & & & & & 1 & -2 \end{pmatrix}_{(K-1)\times(K-1)} . \tag{7.40}$$

As we mentioned in the preceding paragraph, one of the mesh point has to be fixed. Hence, this explains why the line $K/2$ of the matrix reads: $\underline{\mathbf{C}}_{K/2} = (0 \cdots 1 \cdots 0)$ then the value of $f_{K/2}$ is set by $q_{K/2} = 0$. Surprisingly, the point $K/2$ will verify the equation Eq. (7.37) because the total charge is zero.

7.6.2 System of linear equations

Due to the space discretization, as displayed in the preceding section, the differential equation (7.8) and the boundary conditions (7.9)–(7.12) can be written as a linear system of equations. The solution is represented as a vector $\boldsymbol{\phi}$ of dimension $\mathcal{N}$ that contains the values of $\phi(\mathbf{x}_i)$, i.e., the solution of the differential equation in the points $\mathbf{x}_i$. In matrix form, the linear system of equations is written analogously to Eq. (7.39) as

$$\underline{\mathbf{C}}\boldsymbol{\phi} = \mathbf{y}. \tag{7.41}$$

The elements of the $\mathcal{N} \times \mathcal{N}$ matrix $\underline{\mathbf{C}}$ are the coefficients of the $\phi(\mathbf{x}_i)$ in the discretized versions of the Laplace equation (7.8) for all but one mesh points and of the boundary condition (7.10) for the N_S surface points. To obtain a closed system, the Laplace equation in one of the mesh points, say, $\mathbf{x}_{i_0}$ (we choose it to be the center of the cell), is replaced by $\phi(\mathbf{x}_{i_0}) = 0$, since otherwise ϕ would only be determined up to an additive constant, as discussed in the 1D example of the preceding subsection. The vector $\mathbf{y}$ of dimension $\mathcal{N}$ on the right-hand side of Eq. (7.41) contains the inhomogeneities arising from the boundary condition (7.10) due to the non-vanishing value of $\mathbf{u}_p$. The discretized first and second partial derivatives that are needed for the calculation of the matrix $\underline{\mathbf{C}}$ are obtained by inverting the Taylor expansion

$$\phi(\mathbf{x}_j) = \phi(\mathbf{x}_i) + \sum_{\mu=1}^{D} \left.\frac{\partial\phi(\mathbf{x})}{\partial x_\mu}\right|_{\mathbf{x}_i} (x_{j,\mu} - x_{i,\mu})$$

$$+\frac{1}{2}\sum_{\mu,\nu=1}^{D}\left.\frac{\partial^2\phi(\mathbf{x})}{\partial x_\mu \partial x_\nu}\right|_{\mathbf{x}_i}(x_{j,\mu}-x_{i,\mu})(x_{j,\nu}-x_{i,\nu}), \qquad (7.42)$$

for $\{\mathbf{x}_j\}$ the nine (in 3D) or five (in 2D) closest and linearly independent points around $\mathbf{x}_i$, lying on the same side of the cluster as the point $\mathbf{x}_i$. The indices μ and ν correspond to the spatial directions. In other words, for each mesh point $\mathbf{x}_i$ the corresponding elements of $\underline{\mathbf{C}}$ will be derived from the inversion of the matrix system

$$\begin{pmatrix} \phi(\mathbf{x}_1)-\phi(\mathbf{x}_i) \\ \phi(\mathbf{x}_2)-\phi(\mathbf{x}_i) \\ \vdots \\ \phi(\mathbf{x}_9)-\phi(\mathbf{x}_i) \end{pmatrix} = \begin{pmatrix} d^{(1)}_{1,i} & d^{(2)}_{1,i} & \cdots & d^{(2)}_{1,i}d^{(3)}_{1,i} \\ d^{(1)}_{2,i} & d^{(2)}_{2,i} & \cdots & d^{(2)}_{2,i}d^{(3)}_{2,i} \\ \vdots & \vdots & \ddots & \vdots \\ d^{(1)}_{9,i} & d^{(2)}_{9,i} & \cdots & d^{(2)}_{9,i}d^{(3)}_{9,i} \end{pmatrix} \begin{pmatrix} \frac{\partial\phi(\mathbf{x})}{\partial x_1} \\ \frac{\partial\phi(\mathbf{x})}{\partial x_2} \\ \vdots \\ \frac{\partial^2\phi(\mathbf{x})}{\partial x_2 \partial x_3} \end{pmatrix}, \qquad (7.43)$$

with $d^{(\mu)}_{j,i} = x_{j,\mu} - x_{i,\mu}$.

We note that in the special case of a 2D mesh with orthogonal axes (as in Fig. 7.4), one recovers in this way exactly the expressions given in Ref. [Greenspan, 1964] for the derivatives.

7.6.3 Algorithms

In order to reduce the size of the matrix $\underline{\mathbf{C}}$ in memory, we use a sparse matrix storage (i.e., only non-zero matrix elements are stored). Unfortunately, the solution of Eq. (7.41) cannot be found with iterative methods (e.g., Gauss-Seidel) because the matrix is not positive definite. Therefore, a direct LU decomposition is needed, during which the size of the matrix blows up, which limits the maximum size of N. The solution was the distribution of the memory to several computers with the help of OpenMPI and Intel MKL PARDISO libraries on the IN2P3 Calculation Center in Lyon.

7.7 Geometries

7.7.1 Body-Centered Cubic lattice (3D)

In the less dense parts of the inner crust, one expects a Coulomb lattice of spherical clusters. The most favorable arrangement in space is probably a BCC lattice [Oyamatsu et al., 1984]. The primitive cell of this lattice, Fig. 7.6, has one cluster at its center and one eighth at each corner, i.e., it contains in total two clusters.

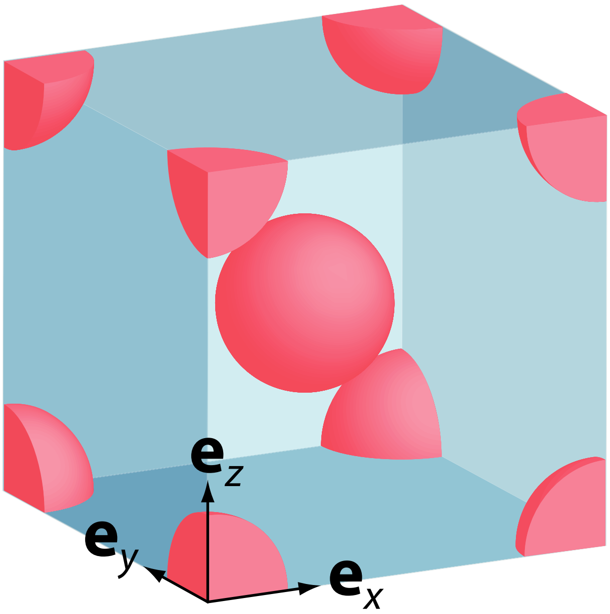

Figure 7.6: Primitive cell of a BCC lattice of spherical clusters.

The BCC primitive cell presents symmetries simplifying the expressions for the average current and the kinetic energy. Assuming a velocity $\mathbf{u}_p$ in direction x and $\mathbf{u}_n = 0$, the average neutron current reads

$$\bar{\mathbf{j}}_n = \underline{\mathbf{n}}_n^b \mathbf{u}_p = \begin{pmatrix} n_{n,11}^b \\ n_{n,21}^b \\ n_{n,31}^b \end{pmatrix} u_p \,, \tag{7.44}$$

with $n_{n,ij}^b$ the elements of the matrix $\underline{\mathbf{n}}_n^b$ in the basis $\{\mathbf{e}_x, \mathbf{e}_y, \mathbf{e}_z\}$. Because of the symmetry $y \leftrightarrow -y$ and $z \leftrightarrow -z$, the current $\bar{\mathbf{j}}_n$ cannot have any component in y or z directions, i.e., the off-diagonal elements $n_{n,21}^b$ and $n_{n,31}^b$ must vanish. Repeating the same arguments for velocities $\mathbf{u}_p$ in y or z directions, one finds that all off-diagonal elements are zero.

Furthermore, the directions x, y and z are equivalent in BCC symmetry. Thus all diagonal terms are equal, and the matrix simply reduces to a scalar matrix $\underline{\mathbf{n}}_n^b = n_n^b \underline{\mathbf{I}}_3$. So finally, in the BCC lattice, for $\mathbf{u}_n = 0$, $\bar{\mathbf{j}}_n$ and $\mathscr{E}_{\text{kin},n}$ are simply given by

$$\bar{\mathbf{j}}_n = n_n^b \mathbf{u}_p \quad \text{and} \quad \mathscr{E}_{\text{kin},n} = \frac{m}{2} n_n^b \mathbf{u}_p^2 \,, \tag{7.45}$$

and there is no effect of anisotropy.

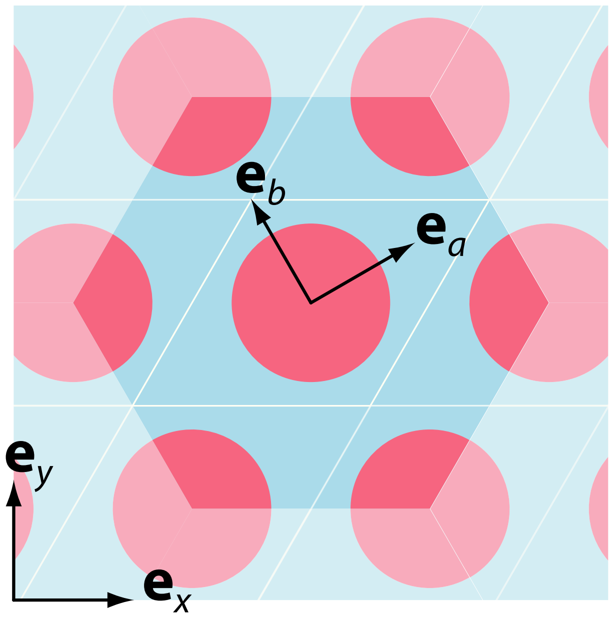

Figure 7.7: Cut through a hexagonal lattice of cylindrical rods. The primitive cell is the parallelogram delimited by the white lines.

7.7.2 Hexagonal lattice (2D)

Deeper in the crust, clusters are supposed to be rods of bound nucleons, cf. Chapter 1. In this case the most favored arrangement with respect to the Coulomb energy is a hexagonal lattice [Oyamatsu et al., 1984]. The primitive cell is a rhombus of side length L, height $\sqrt{3}L/2$ and an angle of $\pi/3$, as shown in Fig. 7.7. From the symmetry of the cell it is clear that the eigenvectors of $\underline{\mathbf{n}}_n^b$ are $\mathbf{e}_a$, $\mathbf{e}_b$ and $\mathbf{e}_z$ with:

$$\begin{pmatrix} \mathbf{e}_a \\ \mathbf{e}_b \end{pmatrix} = \begin{pmatrix} \sqrt{3}/2 & 1/2 \\ -1/2 & \sqrt{3}/2 \end{pmatrix} \begin{pmatrix} \mathbf{e}_x \\ \mathbf{e}_y \end{pmatrix} . \tag{7.46}$$

The vectors $\mathbf{e}_a$ and $\mathbf{e}_b$ are shown in Fig. 7.7. The three directions (a,b,z) are, however, not equivalent, thus in the basis $\{\mathbf{e}_a, \mathbf{e}_b, \mathbf{e}_z\}$ the diagonal elements (eigenvalues) of $\underline{\mathbf{n}}_n^b$ are all different: $n_{n,11}^b \neq n_{n,22}^b \neq n_{n,33}^b$. Let us note that the rods are invariant with respect to the z axis, i.e., all neutrons can move freely in that direction, consequently $n_{n,33}^b = 0$.

Chapter 8

Results for the entrainment

The inner crust consists of nuclear clusters in a dilute and superfluid neutron gas. However, the clusters are made of “bound” neutrons and protons, while the surrounding gas is also made of neutrons. This will affect the hydrodynamics of the inner crust, and we expect entrainment effects as introduced in Chapter 7. We will detail in this chapter most of the results presented in Ref. [Martin and Urban, 2016] which accounts for the periodic lattice arrangement of the crust.

8.1 Microscopic flow

We solve Eqs. (7.8)–(7.10) for a fixed velocity $\mathbf{u}_p$ of the clusters. As input for the radius of the clusters, the densities inside and outside the clusters, and the cell size, we use results obtained in Chap. 6 within the Extended Thomas-Fermi (ETF) method with a Skyrme energy-density functional (SLy4).

Figures 8.1 and 8.2 show streamlines and velocity potential in a BCC cell, in the case of $\mathbf{u}_p$ in x direction. The neutron-fluid streamlines are displayed as white arrows, they characterize the flow direction and are tangential to the velocity field vectors. The background color scheme indicates the speed, from dark purple in the slowest zones to red in the fastest ones. We chose two cuts through the cell parallel to the xy plane. Figure 8.1 corresponds to the plane through the center of the cell ($z = 0$), while Figure 8.2 corresponds to a plane between the clusters ($z = L/4$). In Fig. 8.1 the neutron velocity inside the cluster $\mathbf{v}_{n,2}$ is practically constant but lower than the velocity $\mathbf{u}_p$ of the surface. Here, the ratio between the fluid and the surface velocity is $|\mathbf{v}_{n,2}|/|\mathbf{u}_p| = 0.284$, which can be compared with the analytic result (7.30) for the neutron velocity inside a cluster moving through

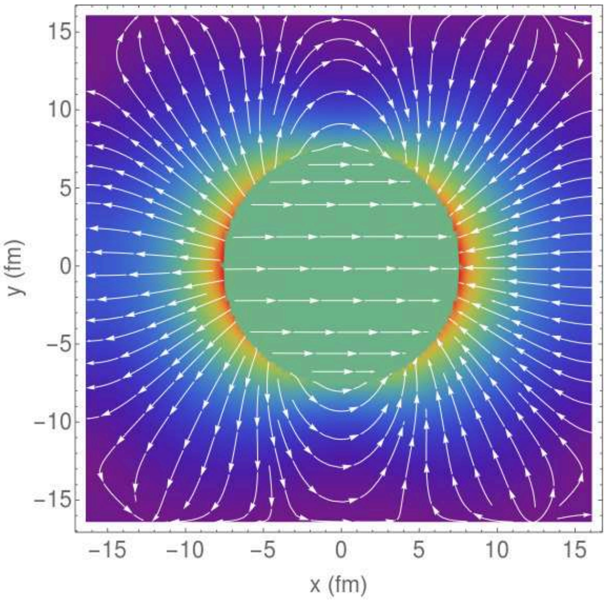

(a) Velocity field

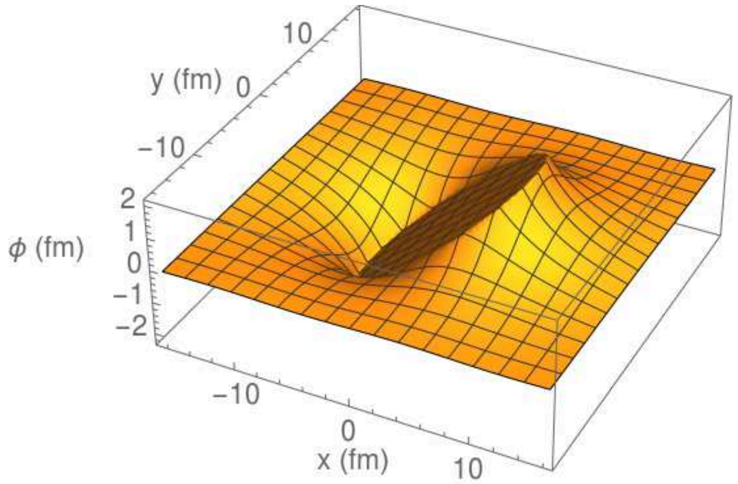

(b) Velocity potential

Figure 8.1: Streamlines and neutron speed (upper panel) and velocity potential (lower panel) in a BCC cell of size $L = 32.8$ fm, with a cluster of radius $R = 7.54$ fm moving with velocity $\mathbf{u}_p = \mathbf{e}_x$. The neutron density inside the cluster is $n_{n,2} = 0.0973$ fm^{-3} and outside $n_{n,1} = 0.0412$ fm^{-3} (the cluster and cell properties were obtained from calculations described in Chap. 6 and correspond to a baryon density of $n_B = 0.0485$ fm^{-3}). In the upper panel, the streamlines are shown as the white arrows, and the speed of the flow is indicated by the background color from dark purple (slowest) to red (fastest). The cross-section of the cell is done on its center at $z = 0$.

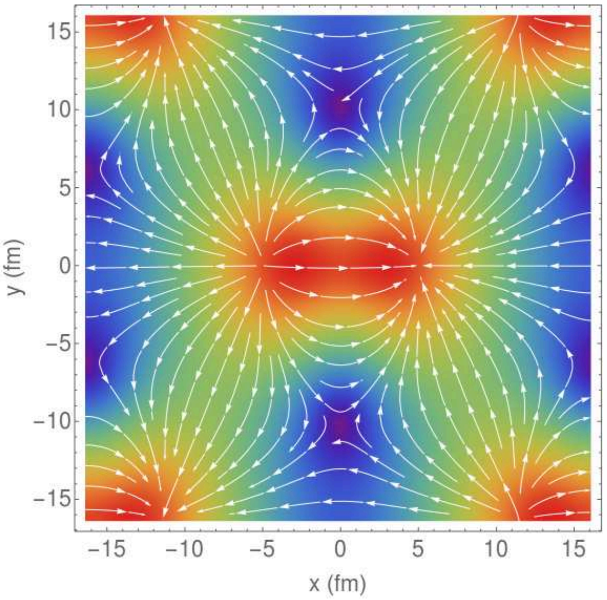

(a) Velocity field

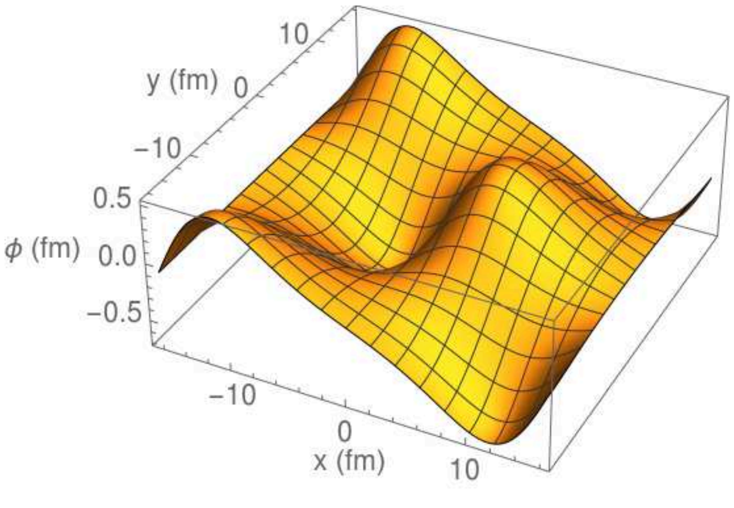

(b) Velocity potential

Figure 8.2: The results are presented similarly to Figure 8.1, but here we display a cross-section between the clusters at $z = L/4$.

an infinite neutron gas: $(1-\gamma)/(2\gamma+1) = 0.315$

Furthermore one sees that neutrons between the clusters move in the opposite direction. The velocity discontinuity at the cluster surface satisfies the boundary condition (7.10) of the conservation of the neutron current crossing the surface. When going away from the cluster surface, we observe that the speed decreases because the flux is spread over a larger surface. Figure 8.2 shows the plane between the clusters at $z = L/4$. One can observe on the edges of the cell the periodicity of the field. The five red areas correspond to the regions that are closest to the clusters.

Let us now discuss the case of the hexagonal lattice shown Figs. 8.3-8.4. Qualitatively, the behavior is similar to the one observed in the BCC lattice. However, in contrast to the BCC case, the hexagonal primitive cell is not isotropic. Thus we performed calculations with velocities $\mathbf{u}_p$ in the directions of the eigenvectors $\mathbf{e}_a$ and $\mathbf{e}_b$ (cf. Sec. 7.7.2). One can clearly see a strong difference of the periodic behavior between Fig. 8.3 and Fig. 8.4, especially at the corners of the primitive cell. In Fig. 8.4, the streamlines continue straight to the next cell, while in Fig. 8.3 they deviate from their initial trend $\mathbf{e}_a$. Instead of exiting or entering through the corners of the cell, the flow passes through its sides and then through the neighboring clusters situated in the directions of the translation vectors $\mathbf{a}_1$ and $\mathbf{a}_2$ of the Bravais lattice (parallel to the white lines in Fig. 7.7). Hence, the currents and the energies depend on the direction of $\mathbf{u}_p$. Nevertheless, the anisotropy effect on the ratio $|\mathbf{v}_{n,2}|/|\mathbf{u}_p|$ is very weak, numerically one finds 0.244 and 0.248 in the cases of $\mathbf{u}_p$ in direction $\mathbf{e}_a$ and $\mathbf{e}_b$, respectively. Similarly to the BCC case, this ratio is somewhat lower than the analytical result Eq. (7.33) for a single rod in an infinite gas, $|\mathbf{v}_{n,2}|/|\mathbf{u}_p| = 0.281$.

8.2 Cluster effective mass and superfluid density

With the help of Eq. (7.16), which is equivalent to averaging the microscopic current over the cell, one obtains the macroscopic quantities $\underline{\mathbf{n}}_n^s$ and $\underline{\mathbf{n}}_n^b$. In Sec. 7.4, they were interpreted as if $\underline{\mathbf{n}}_n^s$ were the neutrons that move independently of the clusters while $\underline{\mathbf{n}}_n^b$ are the neutrons moving with the clusters. However, the preceding discussion of the microscopic flow shows that this is a simplified picture. In the BCC case, staying within this picture, we can define a cluster effective mass number

$$A_{\text{eff}} = N_{\text{eff}} + Z = \frac{1}{2} V_{\mathscr{C}} n_n^b + Z \,, \tag{8.1}$$

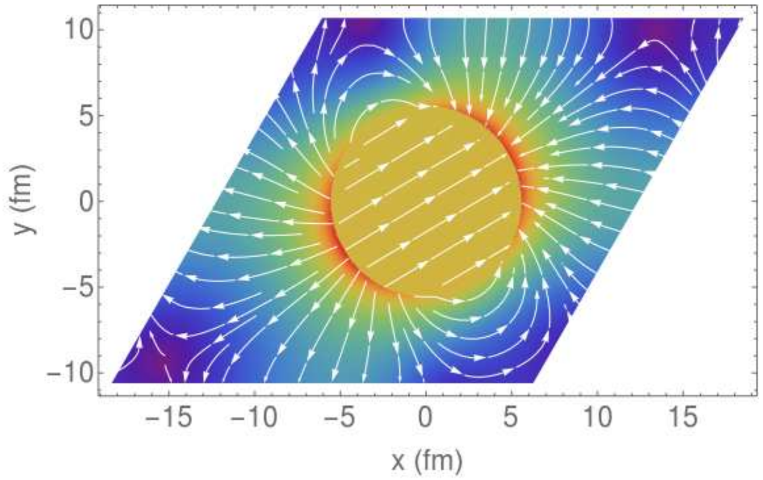

(a) Velocity field

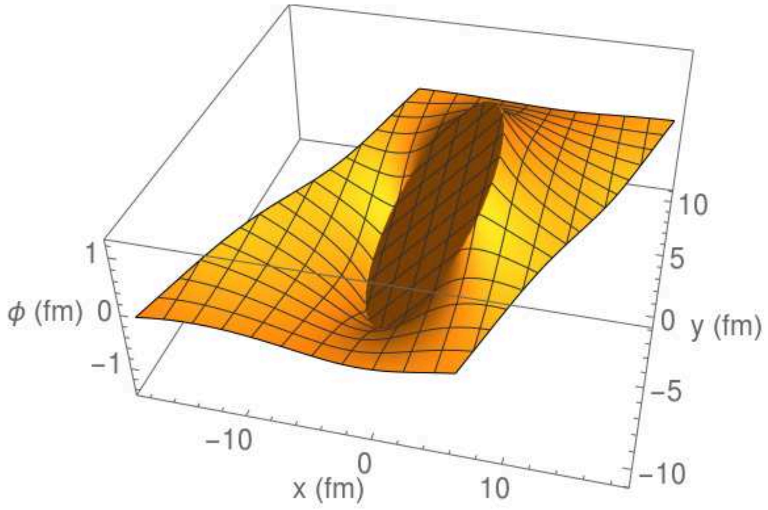

(b) Velocity potential

Figure 8.3: Same as Figs. 8.1-8.2, but for a hexagonal cell of size $L = 24.7$ fm, containing a cylindrical rod of radius 5.53 fm moving with velocity $\mathbf{u}_p = \mathbf{e}_a$. The neutron density inside the rod is 0.0942 fm^{-3} and outside 0.0528 fm^{-3} (corresponding to a baryon density of $n_B = 0.0624$ fm^{-3}).

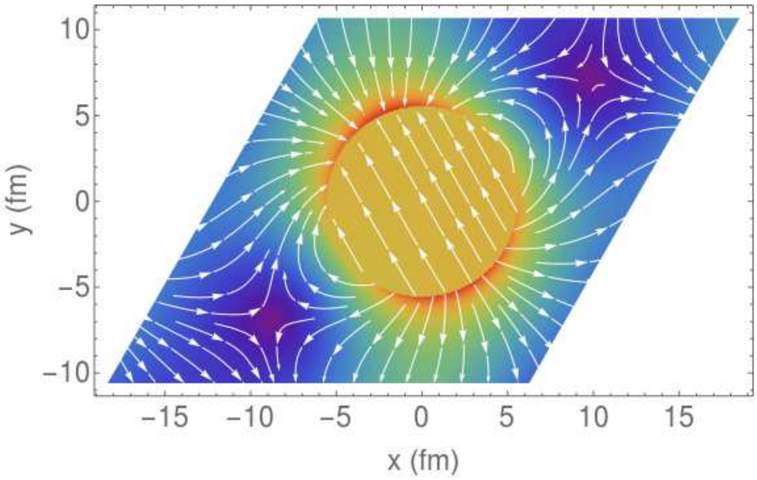

(a) Velocity field

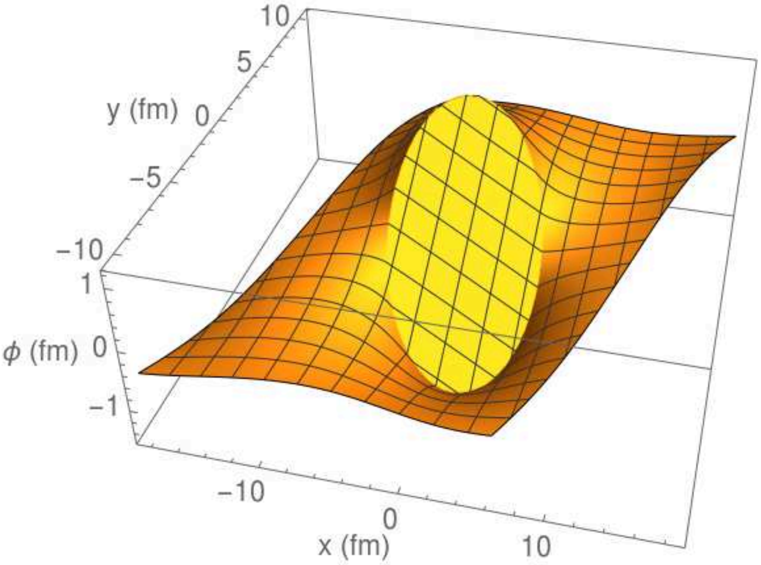

(b) Velocity potential

Figure 8.4: Same as Fig. 8.3, but for a velocity vector oriented in direction $\mathbf{u}_p = \mathbf{e}_b$.

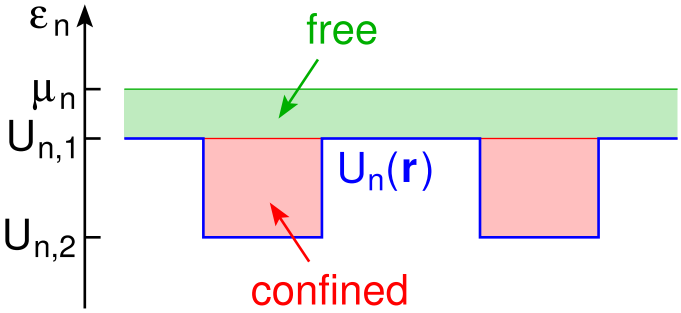

Figure 8.5: Schematic illustration of the definition of free and confined neutrons in energy space.

where the factor 1/2 accounts for the fact that there are two clusters per cell and Z is the number of protons in each cluster.

The cluster effective mass plays an important role for the calculation of the lattice phonons, as discussed, e.g., in Refs. [Sedrakian, 1996, Magierski, 2004, Chamel et al., 2013b]. It can be compared with the trivial result one obtains by counting all nucleons that are geometrically located inside the cluster, $A_{\text{r-cluster}} = N_{\text{r-cluster}} + Z$.

However, it might be more appropriate to define the cluster in energy space (e-cluster [Papakonstantinou et al., 2013]). In this picture, neutrons are considered *free* or *confined* [Chamel and Carter, 2006] (the word *bound* is also employed [Papakonstantinou et al., 2013, Carter et al., 2005] but should not be confused with the effectively bound neutrons defined in Sec. 7.4) depending on their energy and independently of their position, i.e., free neutrons may also be located inside the cluster. In our approximation of constant densities in the two phases, the neutron Hartree-Fock mean field $U_n(\mathbf{r})$ is also constant in each phase and takes the values $U_{n,1}$ in the gas and $U_{n,2}$ in the cluster. Confined neutrons are characterized by a single-particle energy $\epsilon_n(\mathbf{k}) = k^2/(2m_n^*) + U_n$ that lies below the mean field in the gas, $\epsilon_n(\mathbf{k}) < U_{n,1}$, while the single-particle energy of free neutrons lies above, $\epsilon_n(\mathbf{k}) > U_{n,1}$, see Fig. 8.5. Hence, the density of confined neutrons inside the cluster is in this picture given by

$$n_{n,2}^c = \frac{1}{3\pi^2}[2m_{n,2}^*(U_{n,1} - U_{n,2})]^{3/2}, \tag{8.2}$$

with $m_{n,i}^*$ the neutron effective mass calculated in phase i, and the remain-

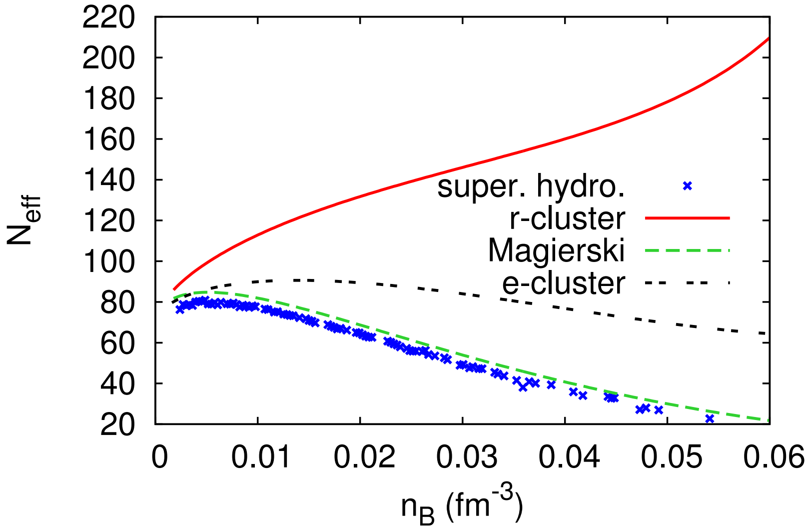

Figure 8.6: Effective neutron number of the clusters moving through the neutron gas as a function of the baryon density n_B. The results of our numerical calculations (blue crosses) are compared with the result of Eq. (7.31) by [Magierski and Bulgac, 2004a, Magierski and Bulgac, 2004b, Magierski, 2004] for an isolated cluster in a uniform neutron gas (green dashed line), and with the neutron numbers (7.32) and (8.4) of the cluster defined in coordinate (red solid line) and energy (black double-dashed line) space, respectively.

ing neutrons inside the cluster are free[1],

$$n^f_{n,2} = n_{n,2} - n^c_{n,2}\,. \tag{8.3}$$

The effective neutron and mass numbers of the cluster (in energy space) are therefore

$$N_{\text{e-cluster}} = \frac{4\pi}{3} R^3 n^c_{n,2} \tag{8.4}$$

and $A_{\text{e-cluster}} = N_{\text{e-cluster}} + Z$. The mean fields $U_{n,i}$ and effective masses $m^*_{n,i}$ in Eq. (8.2) are calculated with the same Skyrme functional (SLy4) that was used in the ETF calculation of the cell properties of Chapter 6.

In Fig. 8.6, we compare the effective neutron numbers of the clusters obtained within the different approaches as functions of the baryon density $n_B = \bar{n}_n + \bar{n}_p$. At low density, i.e., close to the outer crust, the density of

---

[1] Here we do not distinguish between localized and unlocalized unbound neutrons [Papakonstantinou et al., 2013].

the neutron gas is very low and all approaches converge towards the same result. However, at higher density, when the density of the neutron gas increases, the approaches start to differ considerably. More and more neutrons that are located inside the clusters (in coordinate space) are not bound in energy space. Therefore, the number of neutrons in the e-cluster (black double-dashed line) is considerably smaller than the number of neutrons in the r-cluster (red solid line).

However, the effective neutron number obtained within the present superfluid hydrodynamics approach (blue crosses) is even smaller: at the highest densities where one still expects the BCC lattice, one finds $N_{\text{e-cluster}}/N_{\text{r-cluster}} \approx 0.3$, while superfluid hydrodynamics predicts $N_{\text{eff}}/N_{\text{r-cluster}} \approx 0.1$. Quite surprisingly, even at the highest densities, where the unit cell is not very large compared to the cluster size, our numerical results stay quite close to the analytical ones, Eq. (7.31) one would obtain for an isolated cluster (green dashed line).

Concerning the (small) difference between the numerical results and those of Eq. (7.31), one might think that it comes from the restriction of the integration to a finite volume. Actually, one can easily derive a modified version of Eq. (7.31) where one integrates the neutron current $n_n \nabla\phi$ only up to the WS radius instead of infinity, but it turns out that the difference is negligible. The main reason for the difference between the numerical results and those of Eq. (7.31) is the change of the velocity potential ϕ itself due to the periodic boundary conditions.

Another quantity of interest is the superfluid density n_n^s. In Fig. 8.7 we show the superfluid fraction $n_n^s/\bar{n}_n$ as a function of the baryon density n_B. Unfortunately, we cannot perform numerical calculations at very low total densities (as they prevail near the outer crust), because the unit cells become too large. But it seems that at these low densities, the superfluid density obtained within our hydrodynamic approach (solid red line) agrees approximately with the density of free neutrons (green dashed line). At higher total neutron densities, the superfluid fraction is larger than the density of free neutrons and it increases rapidly above 90 %, exceeding 97 % at the transition towards the 2D phase.

We compare these results with those obtained by [Chamel, 2012] in the framework of the band theory for neutrons (black circles). This theory is analogous to the band theory in solid-state physics to describe electrons in the periodic Coulomb potential of a crystal [Ashcroft and Mermin, 1976]. In the inner crust of a neutron star, one has instead neutrons in the periodic mean field generated by the clusters. The superfluid density is in this approach obtained from an average of the Fermi velocity over the (highly nontrivial) Fermi surface [Carter et al., 2005, Chamel, 2006,

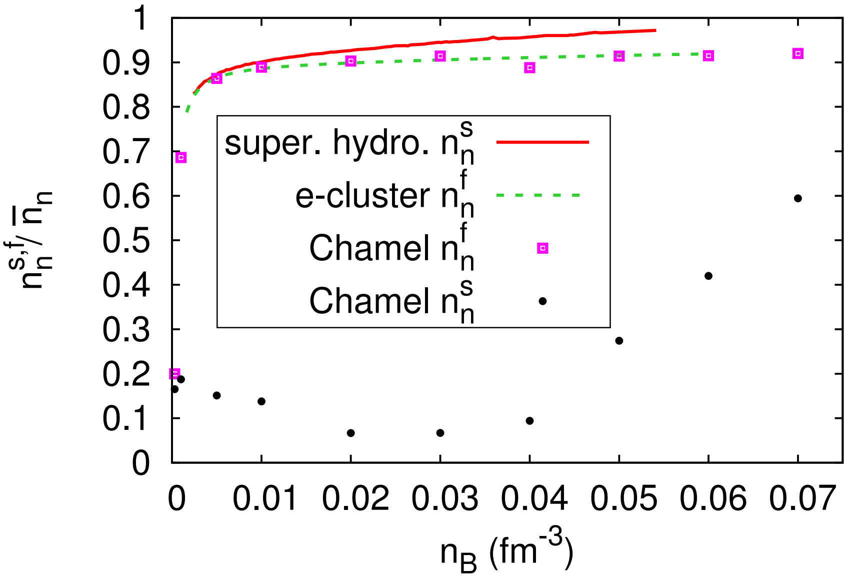

Figure 8.7: Fraction of superfluid neutrons, $n_n^s/\bar{n}_n$ as a function of the baryon density n_B. Results of the present superfluid hydrodynamics approach (red solid line) are compared with the result of band-structure calculations by [Chamel, 2012] (black circles). We display also our results for the fraction of (energetically) free neutrons $n_n^f/\bar{n}_n$ (green dashes) and those obtained within the band-structure approach [Chamel, 2012] (purple squares).

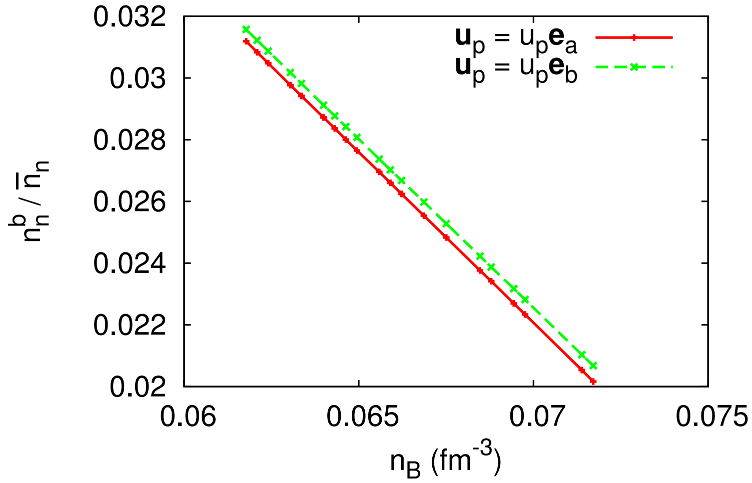

Figure 8.8: Fractions of effectively bound neutrons in the 2D (spaghetti) phase for velocities in the directions of the two eigenvectors $\mathbf{e}_a$ and $\mathbf{e}_b$ as functions of total baryon density.

Chamel et al., 2013b]. While in our hydrodynamic approach the superfluid density is higher than the density of free neutrons, the band-structure calculation predicts a much lower superfluid density. Possible reasons for this discrepancy will be discussed in Sec. 8.4.

As a consistency check, we also compare our results for the fraction of free neutrons with those of the band-structure approach (purple squares), and for this quantity the agreement is excellent in spite of the crude approximations (sharp interface between the cluster and the gas, Thomas-Fermi approximation for the density of states) underlying Eq. (8.2).

So far we discussed the BCC lattice, where the densities of bound and superfluid neutrons are scalar quantities. The situation is different in the 2D hexagonal lattice of rods. In this case, if the velocity is parallel to the rods (z direction), the neutrons can move independently of the protons and the superfluid fraction is 100 %. In the transverse plane, however, there is some entrainment. In Fig. 8.8, we show the fractions of bound neutrons, $n_n^b/\bar{n}_n$, for velocities in the directions of the eigenvectors $\mathbf{e}_a$ (red solid line) and $\mathbf{e}_b$ (green dashed line), as functions of the baryon density in the density range where we expect to find the 2D phase, i.e., between ~ 0.06 and 0.07 fm^{-3}, see Chap. 6. It can be seen that the anisotropy in the transverse plane, i.e., the difference between the directions a and b, is very small.

8.3 Superfluidity within clusters

In the previous sections of this chapter, we discussed the results for clusters in which all neutrons were assumed to participate in the superfluid flow. However, in Sec. 7.2.2, we mentioned the analogy with rotating nuclei which exhibit a mixture of rotational and irrotational flow. This was motivated by the fact that, as in ordinary nuclei, the coherence length ξ of the Cooper pairs is similar to the cluster size. Hence, one might think about describing the neutrons in the clusters as a mixture of superfluid neutrons, whose motion is governed by the phase φ of the gap, and normal-fluid neutrons, which move together with the protons. Recently it was suggested in the supplemental material of Ref. [Wlazłowski et al., 2016] to modify the hydrodynamic model of Refs. [Magierski and Bulgac, 2004a, Magierski and Bulgac, 2004b, Magierski, 2004] in this sense by reinterpreting the densities $n_{n,1}$ and $n_{n,2}$ as effective superfluid densities. For instance, if we assume that all neutrons in the gas but only a fraction δ of the neutrons in the cluster participate in the superfluid motion, Eq. (7.31) for the effective mass of a single spherical cluster becomes

$$N_{\text{eff}} = N_{\text{r-cluster}}\Big(1-\delta+\frac{(\delta-\gamma)^2}{\delta+2\gamma}\Big). \tag{8.5}$$

In the extreme case $\delta = 0$ (no superfluidity inside the clusters, i.e., all neutrons in the cluster move together with the protons), one retrieves the picture of the gas flowing around the cluster as in Ref. [Sedrakian, 1996], resulting in $N_{\text{eff}} = N_{\text{r-cluster}}(1+\gamma/2)$. However, this extreme case does not seem to be realistic, since, e.g., in rotating nuclei at least one half of the nucleons follow the superfluid motion as one can conclude from the moments of inertia. Furthermore, we note that the present situation of a uniform flow of neutrons through the cluster is more favorable for hydrodynamics than the rotation of nuclei: while in a deformed nucleus rotating around the z axis the phase φ is proportional to xy [Migdal, 1959], our phase is (inside the clusters) only linear in the coordinates. Therefore, δ should probably be larger than one half. In analogy to the result of Sec. 8.2 that N_{eff} in the periodic lattice follows closely the analytic formula (7.31), we can also compute the superfluid density

$$n_n^s = \bar{n}_n - 2\frac{N_{\text{eff}}}{V_{\mathscr{C}}}, \tag{8.6}$$

with N_{eff} from Eq. (8.5). The resulting superfluid fractions for three values of δ are shown in Fig. 8.9. The case $\delta = 1$ corresponds to the one shown already in Fig. 8.7, but also for $\delta = 0.5$ and even in the extreme case $\delta = 0$ we obtain a superfluid density that is considerably larger than the one

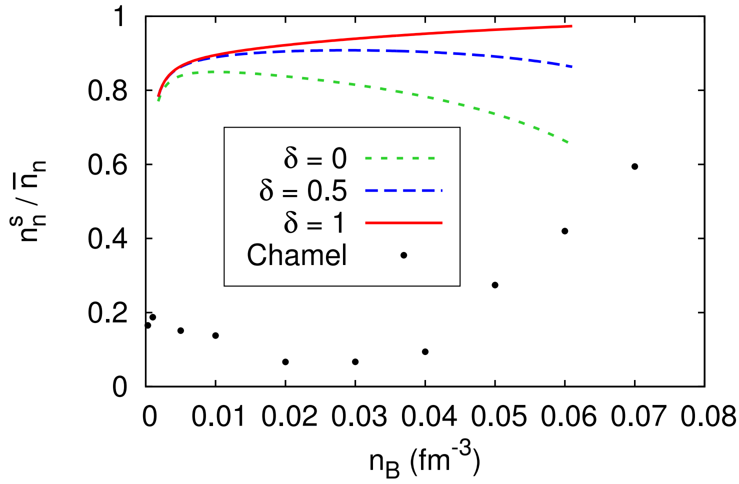

Figure 8.9: Superfluid fraction $n_n^s/\bar{n}_n$ as a function of the baryon density n_B, obtained under the assumption that a fraction $\delta = 0$ (green short dashes), 0.5 (blue long dashes), or 1 (red solid line) of the neutrons in the clusters are superfluid. For comparison, the black circles are the result of the band-structure calculations [Chamel, 2012].

of Ref. [Chamel, 2012].

8.4 Discussion

In this chapter, we used a superfluid hydrodynamics approach to determine how the gas neutrons flow on a microscopic scale around and through the clusters when the crystal lattice of the clusters is uniformly and slowly moved through the gas. This allowed us to compute the densities of superfluid and bound (entrained) neutrons, n_n^s and n_n^b, and the effective mass of the clusters. Surprisingly, it turned out that n_n^s is larger than the density of free neutrons, n_n^f. As a consequence, the cluster effective mass number A_{eff} is not only smaller than the number of nucleons that are spatially located inside the cluster, but even smaller than the number of energetically bound nucleons.

Our results are in line with those obtained in Refs. [Magierski and Bulgac, 2004a, Magierski and Bulgac, 2004b, Magierski, 2004] using the same hydrodynamic approach but for the case of an isolated cluster in an infinite neutron gas. However, in other studies, the opposite effect was found, namely that the effective mass of the clusters is increased by the presence of the gas.

For instance, in Ref. [Sedrakian, 1996], a hydrodynamic approach was used, too, but with different boundary conditions at the interface between the cluster and the gas. In that work, the gas was assumed to flow around the cluster, increasing the total kinetic energy, while in our approach and that of Refs. [Magierski and Bulgac, 2004a, Magierski and Bulgac, 2004b, Magierski, 2004] the permeability of the phase boundary allows the neutrons to flow through the cluster, reducing the neutron velocity inside the cluster and the total kinetic energy.

Studies of entrainment in the framework of band-structure theory [Carter et al., 2005, Chamel, 2012] also predict a strong reduction of n_n^s as compared to n_n^f, and therefore a strong increase of A_{eff}. This approach was developed in analogy to band structure theory for electrons in condensed-matter physics. However, the situation of neutrons in the inner crust differs in some respects from the one of electrons in superconducting metals. In superconductors, the distance between the energy bands, of the order of a few eV, is much larger than the pairing gap Δ which is typically of the order of a few Kelvin (10^{-4} eV). This is why the pairing affects only electrons of the conduction band. The spatial extension of a Cooper pair of electrons is much larger than the unit cell of the crystal. In contrast, the neutron energy bands in the neutron-star crust lie very close to one another (cf. Figs. 2–4 in Ref. [Chamel, 2012]): for a given quasimomentum $\mathbf{k}$, there can be many bands α whose energies $\epsilon_{\alpha\mathbf{k}}$ are separated by less than 1 MeV, which is the typical scale for the pairing gap Δ. This goes along with a coherence length ξ that is smaller than the unit cell.

For hydrodynamics to be quantitatively accurate, one would need a coherence length ξ that is much smaller than the clusters. Since this condition is not satisfied either, the true answer lies probably somewhere between the two extreme results, i.e., the entrainment is maybe stronger than the one predicted by hydrodynamics, but weaker than the one predicted by band structure theory. To find a clear answer to this question, one should ideally perform a QRPA calculation on top of a Hartree-Fock-Bogoliubov (HFB) ground state imposing the Bloch boundary conditions [Ashcroft and Mermin, 1976] on the single-particle wave functions as in band structure theory. However, at present this objective seems to be out of reach. Using a much simpler QRPA calculation in a spherical Wigner-Seitz (WS) cell, as in Ref. [Khan et al., 2005], could help to resolve at least the issue of the most realistic boundary conditions to be used in hydrodynamic calculations. Furthermore, as pointed out in Ref. [Kobyakov and Pethick, 2013], one should probably also consider zero-point oscillations of the clusters that would reduce the band-structure effects.

Chapter 9

Pulsar glitches

9.1 Introduction

Glitches correspond to a sudden transfer of angular momentum from the superfluid to the normal parts of the star [Anderson and Itoh, 1975, Pines and Alpar, 1985, Shapiro and Teukolsky, 2004]. In the preceding Chapters 7 and 8, we discussed the densities of bound and superfluid neutrons in the inner crust. These quantities play a crucial role in the understanding of glitches in the neutron star [Chamel and Carter, 2006, Chamel, 2013]. In particular, as pointed out in Ref. [Chamel, 2013], the observed glitches of the Vela pulsar can hardly be understood with the low superfluid fraction obtained in band structure theory. Since our results for the superfluid fraction are very different from those of band structure theory, let us discuss how this changes the conclusions from the analysis of glitch data. In this subsection, we follow to a large extent the arguments given in Refs. [Chamel and Carter, 2006, Chamel, 2013].

9.2 Superfluid part as a reservoir of angular momentum

Let us assume that the superfluid and the normal parts of the star rotate at slightly different but spatially constant frequencies Ω_s and Ω_b, i.e., the velocity fields are given by $\mathbf{u}_n = \mathbf{\Omega}_s \times \mathbf{r}$ and $\mathbf{u}_p = \mathbf{\Omega}_b \times \mathbf{r}$.

Note that $\mathbf{u}_n$ has to be understood as the average velocity field on length scales that are large compared to the distance between the quantized vortices [Lifshitz and Pitaevskii, 1980]. If we consider, e.g., a frequency of $\Omega_s = 100\ \text{s}^{-1}$, the number of vortices per area is [Pines and Alpar, 1985]

$2m\Omega_s/(\pi\hbar) \approx 10^9$ m^{-2}, i.e., the vortices are separated by ~ 30 μm. Since this distance is many orders of magnitude larger than the crystalline structures in the inner crust, one may use the results for n_n^s and n_n^b calculated for a uniform velocity field.

The total angular momentum of the star reads as:

$$J = \int m \left[n_n^s u_n + n_n^b u_p \right] r_\perp d^3r \,, \tag{9.1}$$

with $r_\perp = r\sin\theta$ the radial distance from the rotation axis. According to Eq. (9.1), the angular momentum can be decomposed into two contributions,

$$J = J_s + J_b = I_s\Omega_s + I_b\Omega_b \,. \tag{9.2}$$

where I_s and I_b are the moments of inertia of the superfluid and normal-fluid components, respectively [1]:

$$I_s = \int m n_n^s r_\perp^2 d^3r \,, \qquad I_b = \int m(n_n^b + n_p) r_\perp^2 d^3r \,. \tag{9.3}$$

As argued in Refs. [Link et al., 1999, Chamel and Carter, 2006], the entire core is probably rotating together with the non-superfluid part. Therefore, the superfluid contribution comes only from the superfluid neutrons in the inner crust, and the neutrons in the core are counted in n_n^b, although they are of course not bound to clusters.

Between two glitches, the observable frequency Ω_b is slowly decreasing because the emission of radiation leads to some loss of angular momentum of the normal component. Let us denote by $\Delta\Omega_b < 0$ the frequency change during the interglitch time. The superfluid component, however, is supposed to slow down much less than the normal component, e.g., because the vortices are pinned. In consequence, during the interglitch time we suppose in the most favorable case that

$$\Delta\Omega_s = 0 \,. \tag{9.4}$$

Hence, the superfluid component can serve as a reservoir of angular momentum for the next glitch [Link et al., 1999]. A glitch is interpreted as a sudden transfer of angular momentum from the superfluid to the normal fluid component. However, during the short duration of the glitch, the total angular momentum is conserved, $\delta J = 0$. Therefore, the differences of the frequencies before and after the glitch, denoted by $\delta\Omega_s$ and $\delta\Omega_b$, satisfy

$$I_s\delta\Omega_s + I_b\delta\Omega_b = 0 \,. \tag{9.5}$$

---

[1] Note that, unlike in Ref. [Chamel and Carter, 2006], there are no non-diagonal contributions to the angular momentum (contributions of Ω_s to J_b and vice versa) because we are working in the chemical basis of superfluid and bound neutrons, cf. Eq. (7.25).

This conservation of angular momentum leads to a relation between the loss of angular velocity of the superfluid and the increase of angular velocity of the normal part of the star

$$\delta\Omega_s = -\frac{I_s}{I_b}\delta\Omega_b\,. \tag{9.6}$$

Since $\Omega_s - \Omega_b$ cannot become too large, Ω_s must in average (after many glitches) decrease by the same amount as Ω_b, i.e.,

$$\langle\delta\Omega_s\rangle \geq \langle\Delta\Omega_b\rangle + \langle\delta\Omega_b\rangle\,, \tag{9.7}$$

where the equality corresponds to the limiting case that the superfluid does not slow down at all between two glitches ($\Delta\Omega_s = 0$). Combining Eq. (9.6) and (9.7), one arrives at the simple relation:

$$\frac{I_s}{I} \geq -\frac{\langle\delta\Omega_b\rangle}{\langle\Delta\Omega_b\rangle} \equiv \mathcal{G}\,, \tag{9.8}$$

with $I = I_s + I_b$ the total moment of inertia of the neutron star, and $\mathcal{G}$ the *coupling parameter*, which is closely related to the *pulsar activity parameter* [Link et al., 1999].

9.3 Limit of a thin crust

Following Ref. [Chamel, 2013], one can make some additional approximations in order to obtain a quick estimate for the ratio I_s/I. First, we write

$$\frac{I_s}{I} = \frac{I_{\text{crust}}}{I}\frac{I_s}{I_{\text{crust}}}\,, \tag{9.9}$$

where I_{crust} is the moment of inertia of the crust. For the crustal fraction of the moment of inertia, I_{crust}/I, Lattimer and Prakash [Lattimer and Prakash, 2000] gave an approximate expression that depends only on the pressure P_{core} and density n_{core} at the crust-core transition and on the total radius R and mass M of the star, but does not require detailed knowledge of the high-density equation of state (EOS) in the core.

Let us start with the Tolman-Oppenheimer-Volkoff (TOV) [Tolman, 1939, Oppenheimer and Volkoff, 1939] equation which defines the mass-radius relation for a non-rotating neutron star

$$\frac{dP(r)}{dr} = -\frac{Gn_B(r)m(r)}{r^2}\left[1+\frac{P(r)}{n_B(r)}\right]\left[1+\frac{4\pi r^3P(r)}{m(r)}\right]\left[1-\frac{2Gm(r)}{rc^2}\right]^{-1}\,, \tag{9.10}$$

with the gravitational constant G and the integrated mass

$$m(r) = \int_0^r m n_B(r) d^3 r, \tag{9.11}$$

with m the nucleon mass. The right hand side of the TOV equation (9.10) is a function of the baryon density $n_B(r)$ and of the pressure $P(r)$ in the star. Moreover, making use of the thin crust approximation $\Delta R \ll R$ with ΔR the crust width and R the neutron star radius, one can simplify the TOV equation to [Lorenz et al., 1993]

$$\frac{dP(r)}{dr} \simeq \frac{n_B(r) G M \Lambda}{R^2}, \tag{9.12}$$

with the redshift factor

$$\Lambda = \left(1 - \frac{2GM}{Rc^2}\right)^{-1}. \tag{9.13}$$

Let us express Eq. (9.9) in terms of the inner crust densities and pressures. We start by writing the momenta of inertia of the crust

$$I_{\text{crust}} = \int_{R-\Delta R}^{R} m n_B(r) r_\perp^2 \, d^3 r, \tag{9.14}$$

which under the assumption of $\Delta R \ll R$ simplifies to

$$I_{\text{crust}} = \frac{8\pi}{3} m R^4 \int_{R-\Delta R}^{R} n_B(r) dr. \tag{9.15}$$

By injecting the simplified TOV equation (9.12) in the preceding expression and using $P(R) = 0$ one finds:

$$I_{\text{crust}} = \frac{8\pi}{3} \frac{R^6}{GM\Lambda} P_{\text{core}}, \tag{9.16}$$

with P_{core} the pressure at the crust-core transition. This value is obtained from our calculations of the inner crust properties detailed in Chapter 6. Similarly, one has for the moment of inertia of the superfluid component in the inner crust:

$$I_s = \int_{R-\Delta R}^{R} m n_n^s(r) r_\perp^2 \, d^3 r, \tag{9.17}$$

which in the limit of a thin crust simplifies to

$$I_s = \frac{8\pi}{3} \frac{R^6}{GM\Lambda} \int_0^{P_{\text{core}}} \frac{n_n^s(P)}{n_B P} dP. \tag{9.18}$$

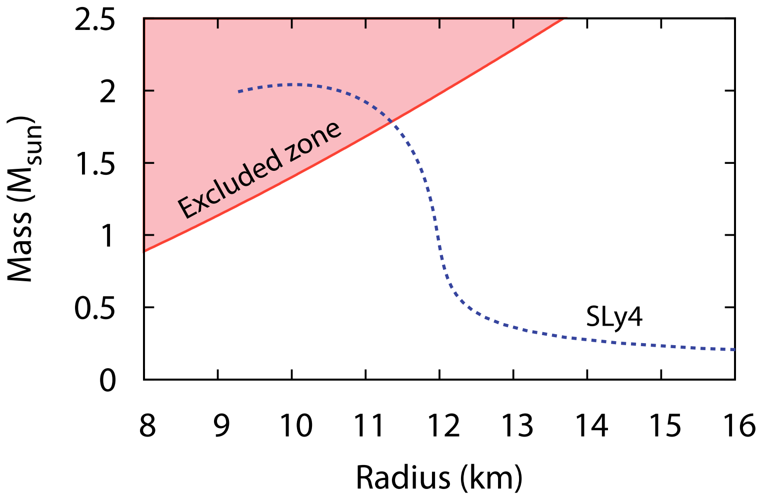

Figure 9.1: Constraints on mass and radius of the Vela pulsar from its observed glitch activity.

Finally, by combining Eqs. (9.16)–(9.18) we have for the ratio I_s/I_{crust}:

$$\frac{I_s}{I_{\text{crust}}} = \frac{1}{P_{\text{core}}} \int_{P_{\text{drip}}}^{P_{\text{core}}} \frac{n_n^s}{n_B} \, dP \,, \tag{9.19}$$

where P_{drip} is the pressure at the transition between the outer and the inner crust (in the outer crust, $n_n^s = 0$). Here, we use the EOS of the ETF model of the inner crust presented in Chap. 6. With our results for the superfluid density, we obtain $I_s/I_{\text{crust}} \approx 0.92$. For the pasta phases with anisotropy (rods, plates), we assume that the orientation is random so that one can average the superfluid density over the three directions.

For the Vela pulsar, one has $\mathscr{G} \approx 1.6\%$ [Chamel, 2013]. With the approximations mentioned above, this allows one to identify an excluded zone in the mass-radius diagram. This is shown in Fig. 9.1. No assumption has been made so far concerning the EOS in the core. To be more specific, we show in Fig. 9.1 also the mass-radius relation obtained by solving the TOV equations with the EOS given by the SLy4 interaction in the whole star (for the outer crust, we use the results of Ref. [Douchin and Haensel, 2000]). One sees that, with this EOS, Vela could have a mass of up to $\lesssim 1.7 M_{\text{sun}}$.

As shown in Ref. [Chamel, 2013], the strong entrainment predicted by band-structure theory can only be conciliated with the observed glitch activity if either Vela is a very unusual neutron star with $M < 0.7 M_{\text{sun}}$, or also the core has a superfluid component that can serve as a reservoir of angular momentum. However, in Fig. 9.1 we see that, with the much larger superfluid density predicted by our approach, the observed glitch activity is compatible with the assumption that Vela is a perfectly normal neutron star.

9.4 Discussion

In this chapter we applied the results of Chapter 8 concerning the superfluid properties of the inner crust to glitch activity of pulsars. Actually, extensive studies of the glitch mechanism [Anderson and Itoh, 1975, Pines and Alpar, 1985, Link et al., 1999] showed a direct relation between the superfluidity and the glitch activity. We based our description on a hydrodynamic treatment as was done in Refs. [Sedrakian, 1996, Magierski and Bulgac, 2004b], with a cluster surface that is permeable for neutrons, as in [Magierski and Bulgac, 2004b]. This approach is assumed to be consistent under the inner crust conditions especially because of the strong pairing gap [Grasso et al., 2005].

We started with the description of a slowly-rotating pulsar in the chemical basis of bound and superfluid parts, avoiding the complications of non-diagonal terms due to entrainment as in [Chamel and Carter, 2006]. We treated the inertial properties of the neutron star by determining I, I_{crust} and I_s in the thin-crust approximation [Lorenz et al., 1993, Carter et al., 2005]. The inertial properties of the star depend on the superfluidity, and previous calculations presented a small superfluid fraction ($n_n^s/\bar{n}_n \lesssim 0.6$) [Chamel, 2013]. However, in Chapter 8 we observed an opposite behavior ($n_n^s/\bar{n}_n \gtrsim 0.8$) which let us suppose a strongly different conclusion for glitches. Indeed, concerning the Vela pulsar we found a mass up to $\sim 1.7 M_\odot$ would be compatible with its observed glitch activity, while in [Chamel, 2013] it would have to be lower than $\sim 0.7 M_\odot$.

However, before drawing firm conclusions our calculations should be improved first of all by treating Vela pulsar with the exact TOV equation, in order to avoid errors from the thin-crust approximation. In fact, as we presented in Fig. 1.2 of Chap. 1, the crust represents a few kilometers of the star. Moreover, the glitch mechanism was treated in a simple model of transfer of angular momentum and in the limit of a uniformly rotating star, but as argued by [Pines and Alpar, 1985, Andersson et al., 2012] this model has to be refined.

Conclusions and outlook

In this thesis we described the characteristics of the inner crust from the nuclear physics point of view. The work was split into the study of three parts: the neutron gas, the nuclear clusters, and the interaction of both of them. We concentrated on the hydrodynamic approach for the dynamics of the inner crust and we compared it to other formalisms. Finally, we discussed the astrophysical impact of the inner crust description we had developed.

In Part II we began by treating a uniform neutron gas. As mentioned in Chapter 1, the inner crust consists of clusters immersed in a dilute and superfluid neutron gas. According to the work of [Anderson, 1958], we expect that this superfluid presents low-energy excitations, i.e., a Goldstone mode. We described the collective mode in Chapter 4 in the framework of the quasiparticle random phase approximation (QRPA), see Chap. 3. We included the complete particle-hole (ph) residual interaction from a Skyrme functional in QRPA calculation, as detailed in Appendix B. We focused on the response functions (RFs) computed from QRPA, which eventually present poles related to the presence of the collective mode. It was interesting to compare the RFs obtained with the complete interaction with the one obtained within Landau approximation. We pointed out that this approximation does not affect the energy of the collective mode at low energy (undamped mode) involving only excitations close to the Fermi surface. However, the shape of the RFs are different for high momentum, when the (damped) collective mode enters in the continuum and involves ph excitations far from the Fermi surface. This difference can affect neutrino scattering calculations which are often performed by using RFs of neutron matter.

In a first approximation, the dispersion relation of the collective mode can be described in the limit of low momentum and low energy excitation by hydrodynamics, so that one finds a sound mode (linear dispersion relation), see Chap. 3. In addition, the slope of the dispersion relation derived from QPRA fits exactly the sound mode, until its energy gets too close to the pair-breaking threshold. Then, the collective mode deviates from the linear dispersion relation and follows the behavior of the pair-breaking threshold until reaching the continuum. However, the heat capacity is only weakly sensitive to the deviation form the linear shape. The heat capacities computed with QRPA and with the sound mode are approximately the same. Hence, hydrodynamics can be used in a first approximation to evaluate the heat capacity of the collective mode in neutron stars, it has also the benefit of being computationally much easier. To conclude, let us notice that we clearly observed that the contribution of the collective mode to the heat capacity may be important, because it is as large as the electron contribution, which is usually dominant at low temperature. However, in the calculation of the collective mode, we restricted ourselves to the limit of zero temperature, while it might be important to perform the QRPA at finite temperature if one goes close to the critical temperature of the superfluid. This would result in a damping of the collective mode [Leggett, 1966] and we do not know how this would modify the contribution of the collective mode to heat capacity.

After this study of the uniform matter, we focused on nuclear clusters, i.e., the inhomogeneities of the inner crust, see Part III. In Chapter 5 we described the clusters with the help of the extended Thomas-Fermi (ETF) approximation. This approximation provides a density functional of the kinetic energy and of the spin current. The standard procedure is to solve the Euler-Lagrange equation, however recent work [Aymard et al., 2014] showed that a surface parametrization gives similar results. From the ETF calculations we obtained information on the composition (densities inside and outside the cluster) and on the geometries of the inhomogeneities in the crust (cluster size, cell size). We also obtained a description of the pasta phases by including the possibility of rods and plates of bound nuclear matter to appear. However, it is important to mention that we did not include the cluster deformation. In this approximation, we observed these three phases (spheres, rods and plates) appearing in three different zones of the inner crust, however if the energy differences between the different phases are very small. We formed from the top of the crust to the bottom: spheres, rods and plates, until reaching the core. Let us note that if we had included the cluster deformation, the transition between phases would had been smooth. Hence, in future works it would be interesting to extended this description to deformed clusters. Furthermore, shell effects which are neglected in the ETF framework should be included, by using for instance the Hartee-Fock-Bogoliubov framework. In contrast to certain studies, such as Refs. [Ravenhall et al., 1983, Oyamatsu, 1993, Avancini et al., 2008] we did not observe inverse phases, such as tubes or bubbles. This is due to the proton fraction which is very low $Y_p \sim 0.02-0.05$ in our case because of the β-equilibrium constraint, in contrast to the work of [Avancini et al., 2008] the minimum proton fraction was fixed at $Y_p = 0.3$. We also made the comparison between the ETF approach and the phase coexistence approximation. This latter approximated the inner crust as two nuclear fluids in chemical and mechanical equilibrium. In contrast to ETF, the phase coexistence approach does not include the surface and the Coulomb energies, so that the geometry and the size of the clusters are not accessible anymore. However, we noticed in Chapter 6 that the composition obtained from both approaches seems to coincide, except at the crust-core transition, which appears earlier in the ETF approximation. This phenomena is simply due to the competition between the surface and Coulomb energies which favor the transition to the core. In conclusion, the inner crust description we made with ETF can be used as a starting point for the equation of state and hydrodynamics of the collective modes of the inner crust. In fact, we extracted from ETF the physical quantities required for hydrodynamics: cluster and gas densities, cluster and cell sizes, surface tension. Let us just mention that so far we neglected the zero-point motion of the clusters, i.e., we assumed a static position of the clusters in coordinate space. However, in the work of [Pethick and Potekhin, 1998] it was shown that the displacement of the clusters in certain directions might not lead to a restoring force, so that clusters would be delocalized. In this case, the crust would rather resemble to a liquid crystal. This latter conclusion can completely change the inner crust description.

Finally, we concluded the thesis by treating the entrainment between the clusters and the surrounding gas. In fact, we could not expect to treat both constituents independently, as it was already discussed in the literature [Magierski and Bulgac, 2004b, Chamel, 2013]. We proposed to treat the inner crust by extending the framework of [Magierski and Bulgac, 2004b] to a periodic lattice arrangement of clusters, again assuming that the clusters are localized at well defined periodic positions. Magierski and Bulgac considered an isolated cluster moving with a uniform velocity in an infinite neutron gas, they used the superfluid hydrodynamics to determine the characteristics of the flow. Hydrodynamics is assumed to be consistent under the neutron star conditions, actually the range of densities implies a strong gap which excludes pair-breaking. In addition, the strong gap ensures that the coherence length of the Cooper pairs is strictly smaller than the periodicity scale of the lattice. The lattice arrangement was detailed and determined thanks to Ewald summations in Ref. [Oyamatsu et al., 1984]. The complicated geometries of cells and of clusters required a numerical procedure to solve the hydrodynamic equations. We deduced from these calculations a discrepancy of the number of bound neutrons because of the neutron entrainment is compared to the results for a single cluster in an infinite gas.

These results must be also compared to the work of [Chamel, 2013] who finds more bound neutrons than the geometrical number. This contradiction might originate from the fact that he uses a completely different approach for the entrainment. Actually, he describes the inner crust in the framework of the band structure theory, initially developed for the electrons in solid state physics. However, in neutron star conditions, the pairing gap is as large as the energy gaps between bands, while for Cooper pairs of electrons in solids the gap between bands is much larger than the electron pairing gap.

These results were applied to pulsar glitches, which are supposed to come from a sudden transfer of angular momentum from the superfluid part of the star to the normal one [Anderson and Itoh, 1975, Pines and Alpar, 1985]. If one knows the ratio of superfluidity in the star, one can deduce a limit for the maximal mass of the pulsar. Hence, our results give for the Vela pulsar a maximal mass of $\sim 1.7 M_\odot$, while Chamel finds $\sim 0.7 M_\odot$ [Chamel, 2013, Andersson et al., 2012], unless one admits a contribution of the core to superfluid fraction. However, it is important to mention that our hydrodynamics calculations must be improved by including surface tension and neutron skin of the clusters. In addition, we restricted ourselves to a stationary case where there is no density waves and a static cluster arrangement. In further studies it would be interesting to improve the hydrodynamic calculations we performed, in order to extract the phonons of the lattice contribution to the heat capacity. Most importantly, the quantitative accuracy of hydrodynamics is questionable as it relies on a small coherence length, while pairing inside the cluster is probably too weak. The best approach for the collective mode would be a complete QRPA calculation which includes the lattice arrangement, however such calculation seems out of reach.

Appendix A

Skyrme parameters in PNM

In spin-unpolarized pure neutron matter, the general Skyrme functional [Vautherin and Brink, 1972, Engel et al., 1975, Chabanat et al., 1998] takes the particularly simple form given in Eq. (2.9). The parameters s_i are related to the more common parameters t_i and x_i of Ref. [Chabanat et al., 1998] by

$$s_0 = t_0(1 - x_0), \tag{A.1a}$$

$$s_1 = t_1(1 - x_1), \tag{A.1b}$$

$$s_2 = t_2(1 + x_2), \tag{A.1c}$$

$$s_3 = t_3(1 - x_3). \tag{A.1d}$$

For the numerical values of the parameters t_i, x_i, and α, we use the SLy4 parametrization of Ref. [Chabanat et al., 1998]. For completeness, the parameters s_i and α are listed in Table A.1. Decomposing the ph interaction matrix element Eq. (2.14) according to Eq. (2.15), one obtains:

$$W_1(q) = s_0 + \frac{(\alpha+2)(\alpha+1)}{12} s_3 \rho^\alpha + \frac{s_1 - 3s_2}{4} q^2, \tag{A.2a}$$

$$W_2 = \frac{s_1 + 3s_2}{4}. \tag{A.2b}$$

Table A.1: Parameters of the Sly4 interaction for the case of pure neutron matter.

Parameter	Value
s_0 (MeV fm^3)	-413.16
s_1 (MeV fm^5)	654.29
s_2 (MeV fm^5)	0
s_3 (MeV fm$^{3+3\alpha}$)	-4877.06
α	1/6

Appendix B

Matrix of response function in QRPA

Below we give the explicit expressions for the 16 free quasiparticle response functions that form the matrix $\Pi_{\mathbf{q}}^{(0)}$ in Eq. (3.27).

The ρ^+ response:

$$\Pi_{\mathbf{k}_+,\mathbf{k}_-}^{\rho^+,h^+} = \frac{E_{\mathbf{k}_+}E_{\mathbf{k}_-} - \xi_{\mathbf{k}_+}\xi_{\mathbf{k}_-} + \Delta_{\mathbf{k}_+}\Delta_{\mathbf{k}_-}}{4E_{\mathbf{k}_+}E_{\mathbf{k}_-}} G_{\mathbf{k},\mathbf{q}}^{-}(\omega), \tag{B.1a}$$

$$\Pi_{\mathbf{k}_+,\mathbf{k}_-}^{\rho^+,h^-} = -\frac{E_{\mathbf{k}_+}\xi_{\mathbf{k}_-} - \xi_{\mathbf{k}_+}E_{\mathbf{k}_-}}{4E_{\mathbf{k}_+}E_{\mathbf{k}_-}} G_{\mathbf{k},\mathbf{q}}^{+}(\omega), \tag{B.1b}$$

$$\Pi_{\mathbf{k}_+,\mathbf{k}_-}^{\rho^+,\Delta^+} = -\frac{\xi_{\mathbf{k}_+}\Delta_{\mathbf{k}_-} + \Delta_{\mathbf{k}_+}\xi_{\mathbf{k}_-}}{4E_{\mathbf{k}+}E_{\mathbf{k}-}} G_{\mathbf{k},\mathbf{q}}^{-}(\omega), \tag{B.1c}$$

$$\Pi_{\mathbf{k}_+,\mathbf{k}_-}^{\rho^+,\Delta^-} = -\frac{E_{\mathbf{k}_+}\Delta_{\mathbf{k}_-} + \Delta_{\mathbf{k}_+}E_{\mathbf{k}-}}{4E_{\mathbf{k}+}E_{\mathbf{k}-}} G_{\mathbf{k},\mathbf{q}}^{+}(\omega). \tag{B.1d}$$

The ρ^- response:

$$\Pi_{\mathbf{k}_+,\mathbf{k}_-}^{\rho^-,h^+} = -\frac{E_{\mathbf{k}_+}\xi_{\mathbf{k}_-} - \xi_{\mathbf{k}_+}E_{\mathbf{k}_-}}{4E_{\mathbf{k}_+}E_{\mathbf{k}_-}} G_{\mathbf{k},\mathbf{q}}^{+}(\omega), \tag{B.1e}$$

$$\Pi_{\mathbf{k}_+,\mathbf{k}_-}^{\rho^-,h^-} = \frac{E_{\mathbf{k}_+}E_{\mathbf{k}_-} - \xi_{\mathbf{k}_+}\xi_{\mathbf{k}_-} - \Delta_{\mathbf{k}_+}\Delta_{\mathbf{k}_-}}{4E_{\mathbf{k}_+}E_{\mathbf{k}_-}} G_{\mathbf{k},\mathbf{q}}^{-}(\omega), \tag{B.1f}$$

$$\Pi_{\mathbf{k}_+,\mathbf{k}_-}^{\rho^-,\Delta^+} = -\frac{E_{\mathbf{k}_+}\Delta_{\mathbf{k}_-} - \Delta_{\mathbf{k}_+}E_{\mathbf{k}_-}}{4E_{\mathbf{k}_+}E_{\mathbf{k}_-}} G_{\mathbf{k},\mathbf{q}}^{+}(\omega), \tag{B.1g}$$

$$\Pi_{\mathbf{k}_+,\mathbf{k}_-}^{\rho^-,\Delta^-} = -\frac{\xi_{\mathbf{k}_+}\Delta_{\mathbf{k}_-} - \Delta_{\mathbf{k}_+}\xi_{\mathbf{k}_-}}{4E_{\mathbf{k}_+}E_{\mathbf{k}_-}} G_{\mathbf{k},\mathbf{q}}^{-}(\omega). \tag{B.1h}$$

The κ^+ response:

$$\Pi_{\mathbf{k}_+,\mathbf{k}_-}^{\kappa^+,h^+} = \frac{\xi_{\mathbf{k}_+}\Delta_{\mathbf{k}_-} + \Delta_{\mathbf{k}_+}\xi_{\mathbf{k}_-}}{4E_{\mathbf{k}_+}E_{\mathbf{k}_-}} G_{\mathbf{k},\mathbf{q}}^{-}(\omega), \tag{B.1i}$$

$$\Pi^{\kappa^+,h^-}_{\mathbf{k}_+,\mathbf{k}_-} = \frac{E_{\mathbf{k}_+}\Delta_{\mathbf{k}_-} - \Delta_{\mathbf{k}_+}E_{\mathbf{k}_-}}{4E_{\mathbf{k}_+}E_{\mathbf{k}_-}} G^+_{\mathbf{k},\mathbf{q}}(\omega), \tag{B.1j}$$

$$\Pi^{\kappa^+,\Delta^+}_{\mathbf{k}_+,\mathbf{k}_-} = -\frac{E_{\mathbf{k}_+}E_{\mathbf{k}_-} + \xi_{\mathbf{k}_+}\xi_{\mathbf{k}_-} - \Delta_{\mathbf{k}_+}\Delta_{\mathbf{k}_-}}{4E_{\mathbf{k}+}E_{\mathbf{k}-}} G^-_{\mathbf{k},\mathbf{q}}(\omega), \tag{B.1k}$$

$$\Pi^{\kappa^+,\Delta^-}_{\mathbf{k}_+,\mathbf{k}_-} = -\frac{E_{\mathbf{k}_+}\xi_{\mathbf{k}_-} + \xi_{\mathbf{k}_+}E_{\mathbf{k}_-}}{4E_{\mathbf{k}_+}E_{\mathbf{k}_-}} G^+_{\mathbf{k},\mathbf{q}}(\omega). \tag{B.1l}$$

The κ^- response:

$$\Pi^{\kappa^-,h^+}_{\mathbf{k}_+,\mathbf{k}_-} = \frac{E_{\mathbf{k}_+}\Delta_{\mathbf{k}_-} + \Delta_{\mathbf{k}_+}E_{\mathbf{k}_-}}{4E_{\mathbf{k}_+}E_{\mathbf{k}_-}} G^+_{\mathbf{k},\mathbf{q}}(\omega), \tag{B.1m}$$

$$\Pi^{\kappa^-,h^-}_{\mathbf{k}_+,\mathbf{k}_-} = \frac{\xi_{\mathbf{k}_+}\Delta_{\mathbf{k}_-} - \Delta_{\mathbf{k}_+}\xi_{\mathbf{k}_-}}{4E_{\mathbf{k}_+}E_{\mathbf{k}_-}} G^-_{\mathbf{k},\mathbf{q}}(\omega), \tag{B.1n}$$

$$\Pi^{\kappa^-,\Delta^+}_{\mathbf{k}_+,\mathbf{k}_-} = -\frac{E_{\mathbf{k}_+}\xi_{\mathbf{k}_-} + \xi_{\mathbf{k}_+}E_{\mathbf{k}_-}}{4E_{\mathbf{k}_+}E_{\mathbf{k}_-}} G^+_{\mathbf{k},\mathbf{q}}(\omega), \tag{B.1o}$$

$$\Pi^{\kappa^-,\Delta^-}_{\mathbf{k}_+,\mathbf{k}_-} = -\frac{E_{\mathbf{k}_+}E_{\mathbf{k}_-} + \xi_{\mathbf{k}_+}\xi_{\mathbf{k}_-} + \Delta_{\mathbf{k}_+}\Delta_{\mathbf{k}_-}}{4E_{\mathbf{k}_+}E_{\mathbf{k}_-}} G^-_{\mathbf{k},\mathbf{q}}(\omega). \tag{B.1p}$$

In the above expressions we have used the abbreviation

$$G^{\pm}_{\mathbf{k},\mathbf{q}}(\omega) = \frac{1}{\omega - \Omega_{\mathbf{k},\mathbf{q}} + i\eta} \pm \frac{1}{\omega + \Omega_{\mathbf{k},\mathbf{q}} + i\eta}, \tag{B.2}$$

where $\Omega_{\mathbf{k},\mathbf{q}} = E_{\mathbf{k}_+} + E_{\mathbf{k}_-}$.

The matrix $\langle\langle \Pi^{(0)}_{\mathbf{q}} V \rangle\rangle$ used in Eq. (3.34) is defined as

$$\begin{aligned}
\langle\langle \Pi^{(0)}_{\mathbf{q}} V \rangle\rangle = W_1(q) &\begin{pmatrix}
\langle\langle \Pi^{\rho^+,h^+}_{\mathbf{k}_+,\mathbf{k}_-} \rangle\rangle & 0 & 0 & 0 & 0 \\
\langle\langle k^2 \Pi^{\rho^+,h^+}_{\mathbf{k}_+,\mathbf{k}_-} \rangle\rangle & 0 & 0 & 0 & 0 \\
\langle\langle kz \Pi^{\rho^- h^+}_{\mathbf{k}_+\mathbf{k}_-} \rangle\rangle & 0 & 0 & 0 & 0 \\
\langle\langle F(k) \Pi^{\kappa^+,h^+}_{\mathbf{k}_+,\mathbf{k}_-} \rangle\rangle & 0 & 0 & 0 & 0 \\
\langle\langle F(k) \Pi^{\kappa^-,h^+}_{\mathbf{k}_+,\mathbf{k}_-} \rangle\rangle & 0 & 0 & 0 & 0
\end{pmatrix} \\
+ W_2 &\begin{pmatrix}
\langle\langle k^2 \Pi^{\rho^+,h^+}_{\mathbf{k}_+,\mathbf{k}_-} \rangle\rangle & \langle\langle \Pi^{\rho^+,h^+}_{\mathbf{k}_+,\mathbf{k}_-} \rangle\rangle & -2\langle\langle kz \Pi^{\rho^+,h^-}_{\mathbf{k}_+,\mathbf{k}_-} \rangle\rangle & 0 & 0 \\
\langle\langle k^4 \Pi^{\rho^+,h^+}_{\mathbf{k}_+,\mathbf{k}_-} \rangle\rangle & \langle\langle k^2 \Pi^{\rho^+,h^+}_{\mathbf{k}_+,\mathbf{k}_-} \rangle\rangle & -2\langle\langle k^3 z \Pi^{\rho^+,h^-}_{\mathbf{k}_+,\mathbf{k}_-} \rangle\rangle & 0 & 0 \\
\langle\langle k^3 z \Pi^{\rho^-,h^+}_{\mathbf{k}_+,\mathbf{k}_-} \rangle\rangle & \langle\langle kz \Pi^{\rho^-,h^+}_{\mathbf{k}_+,\mathbf{k}_-} \rangle\rangle & -2\langle\langle k^2 z^2 \Pi^{\rho^-,h^-}_{\mathbf{k}_+,\mathbf{k}_-} \rangle\rangle & 0 & 0 \\
\langle\langle F(k) k^2 \Pi^{\kappa^+,h^+}_{\mathbf{k}_+,\mathbf{k}_-} \rangle\rangle & \langle\langle F(k) \Pi^{\kappa^+,h^+}_{\mathbf{k}_+,\mathbf{k}_-} \rangle\rangle & -2\langle\langle F(k) kz \Pi^{\kappa^+,h^-}_{\mathbf{k}_+,\mathbf{k}_-} \rangle\rangle & 0 & 0 \\
\langle\langle F(k) k^2 \Pi^{\kappa^-,h^+}_{\mathbf{k}_+,\mathbf{k}_-} \rangle\rangle & \langle\langle F(k) \Pi^{\kappa^-,h^+}_{\mathbf{k}_+,\mathbf{k}_-} \rangle\rangle & -2\langle\langle F(k) kz \Pi^{\kappa^-,h^-}_{\mathbf{k}_+,\mathbf{k}_-} \rangle\rangle & 0 & 0
\end{pmatrix}
\end{aligned} \tag{B.3}$$

$$+\,g\begin{pmatrix}0 & 0 & 0 & \langle\!\langle F(k)\Pi^{\rho^+,\Delta^+}_{\mathbf{k}_+,\mathbf{k}_-}\rangle\!\rangle & \langle\!\langle F(k)\Pi^{\rho^+,\Delta^-}_{\mathbf{k}_+,\mathbf{k}_-}\rangle\!\rangle \\ 0 & 0 & 0 & \langle\!\langle F(k)k^2\Pi^{\rho^+,\Delta^+}_{\mathbf{k}_+,\mathbf{k}_-}\rangle\!\rangle & \langle\!\langle F(k)k^2\Pi^{\rho^+,\Delta^-}_{\mathbf{k}_+,\mathbf{k}_-}\rangle\!\rangle \\ 0 & 0 & 0 & \langle\!\langle F^2(k)\Pi^{\kappa^+,\Delta^+}_{\mathbf{k}_+,\mathbf{k}_-}\rangle\!\rangle & \langle\!\langle F^2(k)\Pi^{\kappa^+,\Delta^-}_{\mathbf{k}_+,\mathbf{k}_-}\rangle\!\rangle \\ 0 & 0 & 0 & \langle\!\langle F^2(k)\Pi^{\kappa^+,\Delta^+}_{\mathbf{k}_+,\mathbf{k}_-}\rangle\!\rangle & \langle\!\langle F^2(k)\Pi^{\kappa^+,\Delta^-}_{\mathbf{k}_+,\mathbf{k}_-}\rangle\!\rangle \\ 0 & 0 & 0 & \langle\!\langle F^2(k)\Pi^{\kappa^-,\Delta^+}_{\mathbf{k}_+,\mathbf{k}_-}\rangle\!\rangle & \langle\!\langle F^2(k)\Pi^{\kappa^-,\Delta^-}_{\mathbf{k}_+,\mathbf{k}_-}\rangle\!\rangle\end{pmatrix},$$

with $z = \cos\sphericalangle(\mathbf{k},\mathbf{q})$.

Appendix C

Relation between velocity and phase of the gap in BCS gases

C.1 Gas at rest

Typically, the BCS state is defined for a gas at rest, i.e., the total momentum is equal to zero. Also, let us recall the definition of the BCS ground state (2.23)

$$|\Psi_0\rangle = \prod_{\mathbf{k}} \frac{1}{v_k} \alpha_{\mathbf{k}} \beta_{-\mathbf{k}} |0\rangle \,, \tag{C.1}$$

with $\alpha_{\mathbf{k}}$ and $\beta_{-\mathbf{k}}$ the Bogoliubov operators defined in Eq. (2.24).

Here it is important to treat the expression of the gap equation, which is directly related to the dynamics of the gas. We have for the definition of Δ in coordinate space:

$$\Delta(\mathbf{r}) = -|g| \langle \Psi_0 | \psi_\uparrow(\mathbf{r}) \psi_\downarrow(\mathbf{r}) | \Psi_0 \rangle \,, \tag{C.2}$$

for the sake of simplicity we use for pairing a contact interaction of strength $|g|$ and neglect UV divergence. In the preceding equation we introduced field operators $\psi_\sigma(\mathbf{r})$, which read as:

$$\psi_\uparrow(\mathbf{r}) = \sum_{\mathbf{k}} a_{\mathbf{k},\uparrow} e^{i\mathbf{k}\cdot\mathbf{r}} \,, \tag{C.3a}$$

$$\psi_\downarrow(\mathbf{r}) = \sum_{\mathbf{k}} a_{-\mathbf{k},\downarrow} e^{-i\mathbf{k}\cdot\mathbf{r}} \,, \tag{C.3b}$$

where $a_{\mathbf{k},\sigma}$ stand for annihilation operators. As in Sec. 2.4, we keep the notation that the spins up are associated with $\mathbf{k}$ and spins down with $-\mathbf{k}$. By injecting the definitions of ψ_σ in Eq. (C.2) one has

$$\Delta(\mathbf{r}) = -|g| \sum_{\mathbf{p}\mathbf{p}'} e^{i(\mathbf{p}-\mathbf{p}')\cdot\mathbf{r}} \langle \Psi_0 | a_{\mathbf{p},\uparrow} a_{-\mathbf{p}',\downarrow} | \Psi_0 \rangle \,. \tag{C.4}$$

It is more convenient to express the annihilation operators $a_{\mathbf{k},\sigma}$ in terms of Bogoliubov operators [Fetter and Walecka, 1971]

$$a_{\mathbf{k}\uparrow} = u_k \alpha_{\mathbf{k}} + v_k \beta^{\dagger}_{-\mathbf{k}}, \tag{C.5}$$

$$a_{-\mathbf{k}\downarrow} = u_k \beta_{-\mathbf{k}} - v_k \alpha^{\dagger}_{\mathbf{k}}. \tag{C.6}$$

Hence, the gap equation rewrites as:

$$\Delta(\mathbf{r}) = -|g| \sum_{\mathbf{p}\mathbf{p}'} e^{i(\mathbf{p}-\mathbf{p}')\cdot\mathbf{r}} \langle \Psi_0 | (u_p \alpha_{\mathbf{p}} + v_p \beta^{\dagger}_{-\mathbf{p}})(u_{p'} \beta_{-\mathbf{p}'} - v_{p'} \alpha^{\dagger}_{\mathbf{p}'}) | \Psi_0 \rangle \,. \tag{C.7}$$

Now we proceed step by step. First, consider the term $\alpha^{\dagger}_{\mathbf{p}'} |\Psi_0\rangle$ which annihilates a particle already created by $\alpha_{\mathbf{p}'}$ within $|\Psi_0\rangle$. The product in $|\Psi_0\rangle$ runs over all momenta $\mathbf{k}$ with $\mathbf{p}'$ included. Hence, this term is non-zero and remains in further simplifications. Second, we note that $\beta_{-\mathbf{p}'} |\Psi_0\rangle$ vanishes, since we apply twice the same operator $\beta_{-\mathbf{p}'}$ on the vacuum. It is important to mention that this conclusion is a direct consequence of the anticommutation rules of the Bogoliubov operators (2.26). If one considers the previous results, the pairing gap reduces into

$$\Delta(\mathbf{r}) = |g| \sum_{\mathbf{p}\mathbf{p}'} v_{p'} e^{i(\mathbf{p}-\mathbf{p}')\cdot\mathbf{r}} \langle \Psi_0 | (u_p \alpha_{\mathbf{p}} + v_p \beta^{\dagger}_{-\mathbf{p}}) \alpha^{\dagger}_{\mathbf{p}'} | \Psi_0 \rangle \,. \tag{C.8}$$

Similarly to the effect of $\beta_{-\mathbf{k}}$ on the BCS state, the term $\langle \Psi_0 | \beta^{\dagger}_{-\mathbf{p}}$ vanishes which leads to

$$\Delta(\mathbf{r}) = |g| \sum_{\mathbf{p}\mathbf{p}'} u_p v_{p'} e^{i(\mathbf{p}-\mathbf{p}')\cdot\mathbf{r}} \langle \Psi_0 | \alpha_{\mathbf{p}} \alpha^{\dagger}_{\mathbf{p}'} | \Psi_0 \rangle \,. \tag{C.9}$$

Finally, let us remind the anticommutator of the Bogolibov operator $\{\alpha_{\mathbf{p}}, \alpha^{\dagger}_{\mathbf{p}'}\} = \delta_{\mathbf{p},\mathbf{p}'}$, so the gap equation is simply:

$$\Delta(\mathbf{r}) = |g| \sum_{\mathbf{p}} u_p v_p \,. \tag{C.10}$$

C.2 Uniform flow

Previously we treated the typical case of a BCS gas at rest, as in Refs. [Fetter and Walecka, 1971, Lifshitz and Pitaevskii, 1980]. However in hydrodynamics one has to consider the BCS gas moving with a velocity $\mathbf{v}$. In consequence we assume Cooper pairs made of particles with momenta $\mathbf{k}+\mathbf{q}$ and $-\mathbf{k}+\mathbf{q}$, with $\mathbf{q} = m\mathbf{v}$ and m the mass. In such case, the operators are modified by the applied boost. First, we introduce boosted annihilation operators:

$$\tilde{a}_{\mathbf{k}} = a_{\mathbf{k}+\mathbf{q}} \quad \text{and} \quad \tilde{a}_{-\mathbf{k}} = a_{-\mathbf{k}+\mathbf{q}}\,, \tag{C.11}$$

with $a_{\mathbf{k}}$ the usual annihilation operators. Analogously, the Bogoliubov operators are modified and rewrite as follows:

$$\tilde{\alpha}_{\mathbf{k}} = u_k \tilde{a}_{\mathbf{k}\uparrow} - v_k \tilde{a}^{\dagger}_{-\mathbf{k}\downarrow} \quad \text{and} \quad \tilde{\beta}_{-\mathbf{k}} = u_k \tilde{a}_{-\mathbf{k}\downarrow} + v_k \tilde{a}^{\dagger}_{\mathbf{k}\uparrow}\,. \tag{C.12}$$

Finally, the BCS state for a gas moving uniformly reads as

$$\left|\widetilde{\Psi}_0\right\rangle = \prod_{\mathbf{k}} \frac{1}{v_k} \tilde{\alpha}_{\mathbf{k}} \tilde{\beta}_{-\mathbf{k}} \left|0\right\rangle \tag{C.13}$$

As mentioned in the previous section, the dynamics of the BCS gas is function of its pairing gap. The computation of $\Delta(\mathbf{r})$ requires the expression of the field operators, which in terms of the boosted annihilation operators read as:

$$\psi_{\uparrow}(\mathbf{r}) = \sum_{\mathbf{k}} \tilde{a}_{\mathbf{k},\uparrow} e^{i(\mathbf{k}+\mathbf{q})\cdot\mathbf{r}}\,, \tag{C.14}$$

$$\psi_{\downarrow}(\mathbf{r}) = \sum_{\mathbf{k}} \tilde{a}_{-\mathbf{k},\downarrow} e^{i(-\mathbf{k}+\mathbf{q})\cdot\mathbf{r}}\,. \tag{C.15}$$

Now, let us write the gap equation for $\left|\widetilde{\Psi}_0\right\rangle$:

$$\Delta(\mathbf{r}) = -|g| \sum_{\mathbf{p}\mathbf{p}'} e^{i(\mathbf{p}-\mathbf{p}'+2\mathbf{q})\cdot\mathbf{r}} \left\langle\widetilde{\Psi}_0\right| (u_p \tilde{\alpha}_{\mathbf{p}} + v_p \tilde{\beta}^{\dagger}_{-\mathbf{p}})(u_{p'} \tilde{\beta}_{-\mathbf{p}'} - v_{p'} \tilde{\alpha}^{\dagger}_{\mathbf{p}'}) \left|\widetilde{\Psi}_0\right\rangle\,. \tag{C.16}$$

The properties of the boosted operators $\tilde{\alpha}$ and $\tilde{\beta}$ are identical to those at rest. Thus, we proceed analogously to the former case (cf. Sec. C.1) and the gap equation is simply:

$$\Delta(\mathbf{r}) = |g| \sum_{\mathbf{p}\mathbf{p}'} u_p v_{p'} e^{i(\mathbf{p}-\mathbf{p}'+2\mathbf{q})\cdot\mathbf{r}} \left\langle\widetilde{\Psi}_0\right| \tilde{\alpha}_{\mathbf{p}} \tilde{\alpha}^{\dagger}_{\mathbf{p}'} \left|\widetilde{\Psi}_0\right\rangle\,. \tag{C.17}$$

Let us recall the anticommutator $\{\tilde{\alpha}_{\mathbf{p}}, \tilde{\alpha}^{\dagger}_{\mathbf{p}'}\} = \delta_{\mathbf{p},\mathbf{p}'}$, hence

$$\Delta(\mathbf{r}) = |g| e^{2i\mathbf{q}\cdot\mathbf{r}} \sum_{\mathbf{p}} u_p v_p\,, \tag{C.18}$$

with the phase of the gap $\varphi = 2\mathbf{q}\cdot\mathbf{r}$.

Here it is important to mention that we obtain the famous results for the velocity of a superfluid [Lifshitz and Pitaevskii, 1980]

$$\mathbf{v} = \frac{1}{2m} \nabla\varphi\,. \tag{C.19}$$

Annexe D

Résumé en français

Les étoiles à neutrons ont été largement étudiées depuis que [Baade and Zwicky, 1934] ont postulé leur existence. Ces études sont réalisées à l'interface de différents domaines la physique tels que : l'astrophysique en rayons X [Giacconi et al., 1962], l'observation des pulsars [Hewish et al., 1968, ATNF, 2016], la relativité générale [Tolman, 1939, Oppenheimer and Volkoff, 1939], et plus dernièrement les ondes gravitationnelles [Riles, 2013], la physique du solide [Oyamatsu et al., 1984, Chamel, 2013], ainsi que la physique nucléaire [Glendenning, 1982, Ravenhall et al., 1983, Douchin and Haensel, 2000, Avancini et al., 2008].

Dans cette thèse nous nous concentrerons sur la description des étoiles à neutrons et en particulier de la croûte interne de l'étoile dans le cadre de la physique nucléaire. En effet, la croûte interne présente une structure complexe faite d'agrégats nucléaires immergés dans un gaz de neutrons, tous deux en équilibre mécanique et chimique. C'est ainsi que nous construirons notre étude en trois parties. Tout d'abord nous commencerons par traiter le gaz de neutrons entourant les agrégats. Puis nous en viendrons à la description des agrégats et de leur déformation [Ravenhall et al., 1983] à mesure que l'on descend dans la croûte. Enfin nous traiterons l'interaction entre le gaz et les agrégats, dont la dynamique ne peut pas être traitée indépendamment pour les deux constituants [Sedrakian, 1996, Magierski and Bulgac, 2004b, Chamel, 2013].

Tout d'abord commençons ce travail par une brève introduction sur les étoiles à neutrons.

D.1 Historique et caractéristiques

Historiquement, les étoiles à neutrons ont été postulées bien avant leur première observation et ce dès les années trente [Baade and Zwicky, 1934]. Ils proposèrent alors un modèle d'étoiles massives et compactes. De plus, ils postulèrent qu'elles pourraient être issues des supernovæ.

Commencèrent ainsi les premières études théoriques de la structure de ces étoiles. On notera en particulier les travaux de [Tolman, 1939, Oppenheimer and Volkoff, 1939], qui établirent les premiers développements de l'équilibre hydrostatique des étoiles à neutrons (équation de *Tolman-Oppenheimer-Volkoff*, aussi abrégée *TOV*) en tenant compte des effets relativistes. Encore aujourd'hui l'équation TOV est utilisée pour les calculs de relations masse-rayon des étoiles à neutrons non déformées (dont la vitesse de rotation n'excède pas $\sim$ 200 Hz). Cependant, depuis les premiers développements en 1939, où ils considérèrent un gaz de neutron idéal, les équations d'état de la matière stellaire ont été grandement améliorées [Glendenning, 1982, Douchin and Haensel, 2000, Avancini et al., 2008].

Ce fut une vingtaine d'années plus tard que les premières observations supposées d'étoiles à neutrons furent faites. On retiendra en 1962, la première observation de sources de rayons X extérieures au système solaire par [Giacconi et al., 1962]. Il s'avéra que certaines de ces sources sont des étoiles à neutrons et que leur rayonnement X est le marqueur de leur refroidissement. Il vint ensuite l'observation radio de J. Bell et A. Hewish, qui interceptèrent le premier signal pulsar [Hewish et al., 1968]. Initialement, l'origine de ce signal pulsé et régulier était indéterminée, ironiquement le premier nom que porta l'objet fut *Little Green Men 1* (LGM-1)[1].

Les observations successives confirmèrent que les étoiles à neutrons sont formées lors de l'effondrement gravitationnel du cœur des supernovæ [Shapiro and Teukolsky, 2004, Foglizzo et al., 2015], ce qui n'était jusque là qu'une hypothèse [Baade and Zwicky, 1934]. Cet effondrement a lieu lors de la fin de vie d'étoiles massives de $10-20M_\odot$, avec $M_\odot$ la masse du soleil [Chamel and Haensel, 2008]. Les étoiles à neutrons ainsi formées ont une masse comprise entre 1 et $2M_\odot$ [Demorest et al., 2010] pour un rayon de $\sim$ 10 km [Yakovlev et al., 2001]. On parlera ainsi d'étoiles compactes où la densité est élevée $\sim 10^{15}$ g cm^{-3}, et nécessite la prise en compte des effets relativistes.

La densité élevée de l'étoile donne lieu à une structure interne exotique, que l'on peut diviser en trois différentes strates [Chamel and Haensel, 2008] : la *croûte externe*, la *croûte interne* et le *cœur.*

---

[1] Petits Hommes Verts 1.

La croûte externe est constituée de noyaux atomiques arrangés en un réseau cristallin et d'un gaz d'électrons relativistes. L'arrangement cristallin des noyaux est favorisé par l'interaction Coulombienne entre eux [Oyamatsu et al., 1984]. À mesure que l'on descend dans la croûte de l'étoile on constate une forte augmentation de la fraction de neutrons dans les noyaux, et ce pour satisfaire l'équilibre β. Ainsi, à partir d'une certaine profondeur l'excès de neutrons dans les noyaux est si important qu'ils sont relâchés dans le milieu et un gaz de neutron apparaît. Désormais nous ne parlons plus de noyaux mais d'*agrégats nucléaires* puisque tous les nucléons qui les composent ne sont plus systématiquement liés [Ravenhall et al., 1983]. Dès lors nous faisons notre entrée dans la croûte interne formée d'un gaz et d'agrégats nucléaires en équilibre mécanique et chimique. De plus en raison de la faible température de l'étoile $\sim$ 10 keV [Yakovlev et al., 2001] on s'attend à une superfluidité du gaz de neutrons [Pines and Alpar, 1985].

D.2 Gaz de neutrons superfluide

Comme introduit précédemment les agrégats nucléaires sont immergés dans un gaz de neutrons qui est supposé superfluide [Pines and Alpar, 1985]. Dans ces conditions, on s'attend à voir apparaître dans le gaz un mode collectif de basse énergie, i.e., un mode de Goldstone [Anderson, 1958]. Ce mode collectif va être à l'origine d'une contribution supplémentaire à la capacité calorifique de l'étoile.

Dans la Partie II, nous proposons une description basée sur l'approximation des phases aléatoires des quasiparticules (aussi nommée dans la littérature anglophone *quasiparticle random phase approximation*, soit *QRPA*). Cette approche microscopique est construite sur la théorie Hartree-Fock-Bogoliubov dépendante du temps (*TDHFB*) et développée dans le cadre de la réponse linéaire. Ainsi, nous nous limitons à des modes collectifs de faible amplitude. De plus, nous introduisons dans le formalisme de la QRPA l'interaction particule-trou (*particle-hole*, ou *ph*) complète, qui est dérivée de la fonctionnelle de Skyrme [Chabanat et al., 1997] pour la matière de neutrons. L'expression complète de cette interaction est détaillée dans l'Annexe B. Les résultats sont présentés Chapitre 4 où nous commençons avec les fonctions de réponse obtenues en QRPA. Sur certaines d'entre elles, on constate un pôle qui traduit la présence d'un mode collectif. Ces fonctions de réponse sont aussi comparées à celles obtenues dans l'approximation de Landau, c'est-à-dire dans l'approximation que les excitations ont lieu à proximité de la surface de Fermi. On remarque qu'à grande longueur d'onde, l'énergie du mode collectif est insensible à cette approximation. Mais lorsque le moment du mode collectif est proche du moment de Fermi, on constate une forme très différente des fonctions de réponse. Cela pourrait impacter les calculs de libre parcours moyen des neutrinos dans les étoiles à neutrons, calculs en général dérivés des fonctions de réponse de la matière de neutrons.

Nous nous sommes aussi penchés sur l'approximation du mode collectif à petit moment et énergie à l'aide de l'approche hydrodynamique. Dans cette limite, la relation de dispersion du mode collectif est linéaire, soit un comportement très différent de la QRPA. En effet, la QRPA présente une relation de dispersion tout d'abord linéaire, suivant précisément la pente du mode hydrodynamique. Puis le mode dévie, et il est contraint par l'énergie limite de brisure d'une paire de Cooper. Quant à la chaleur spécifique issue du mode collectif, qu'elle soit calculée par la QPRA ou par l'hydrodynamique, les résultats se trouvent être du même ordre de grandeur. L'hydrodynamique peut donc servir en première approximation pour évaluer la contribution de ce mode collectif. Finalement, nous constatons que le mode collectif peut contribuer tout autant que les électrons, qui jusque là étaient considérés comme dominants. Cependant, nous avons effectué nos calculs dans la limite de température nulle, ce qui peut être imprécis si la température du milieu s'approche de la température critique du superfluide. Dans ce cas un calcul QRPA à température finie serait nécessaire, ce qui aurait pour effet d'amortir le mode collectif [Leggett, 1966] et de modifier sa contribution à la chaleur spécifique.

D.3 Modélisation de la croûte interne

Alors que nous nous sommes concentrés sur le gaz de neutrons uniforme, nous proposons désormais de traiter les inhomogénéités qui composent la croûte, c'est-à-dire les agrégats nucléaires.

Nous réalisons cette étude à l'aide de l'approximation de Thomas-Fermi étendue (*ETF*), comme décrite dans la Partie III et plus précisément dans le Chapitre 5. La procédure standard aurait été de résoudre les équation d'Euler-Lagrange, cependant une paramétrisation de la surface des agrégats est tout aussi précise [Aymard et al., 2014]. Nous incluons dans ces calculs les phases exotiques que peuvent prendre les agrégats qu'ont prédit [Ravenhall et al., 1983], soit des : *cylindres*, *plaques* et des phases inverses (*trous* et *tubes*). Cependant, nous nous limitons à des géométries non déformées, alors que l'on devrait s'attendre à une déformation continue des agrégats avec l'augmentation de la densité. L'approche la plus complète serait de traiter les agrégats dans le cadre de la théorie

Hartree-Fock-Bogoliubov (HFB), qui inclurait les déformations et les effets de couches. Tout de même, nos résultats montrent l'apparition dans la croûte de : sphères, cylindres et plaques à mesure que l'on descend, cf. Chap. 6. À la différence d'un certain nombre d'études [Ravenhall et al., 1983, Oyamatsu, 1993, Avancini et al., 2008] nous n'observons pas de phases inverses. Cela s'explique par la très faible fraction de protons dans la croûte $Y_p \sim 0.02 - 0.05$, due à l'équilibre β, alors que par exemple dans les travaux de [Avancini et al., 2008] la fraction de protons est fixée à un minimum de $Y_p = 0.3$. Nous avons obtenu de ces travaux une description des propriétés des agrégats : densités interne et externe, tailles de la cellule et des agrégats, ainsi que leur tension de surface. Ces calculs nous donnent donc une description complète de la croûte interne qui servira de base pour les calculs d'équation d'état, ainsi que pour l'hydrodynamique de la croûte.

D.4 Hydrodynamique de la croûte interne

Comme introduit précédemment la croûte est formée d'agrégats immergés dans un gaz de neutrons superfluides. Ainsi les deux étant composés des mêmes nucléons, leur comportement dynamique n'est pas indépendant l'un de l'autre.

On propose d'effectuer la description dynamique de la croûte dans le cadre de l'hydrodynamique superfluide, voir Partie IV. Pour ce faire nous généralisons l'approche de [Magierski and Bulgac, 2004a] pour un agrégat isolé dans un gaz infini, à une cellule de taille finie et périodique. Effectivement, les calculs de [Oyamatsu et al., 1984] ont montré que les agrégats nucléaires chargés positivement tendent à s'organiser en un réseau cristallin de telle sorte à minimiser l'énergie Coulombienne. Ainsi les sphères et les cylindres s'organisent respectivement en maille cubique centrée et hexagonale. La géométrie des agrégats ajouté à leur arrangement cristallin requiert une résolution numérique de l'hydrodynamique superfluide. La description dynamique obtenue pour les agrégats dans le gaz est détaillée dans le Chapitre 8. Les résultats montrent que le nombre de neutrons effectivement liés aux agrégats est très inférieur par rapport au nombre de neutrons localisés spatialement dans leur rayon. Cet effet est appelé l'*entraînement* des neutrons et est ici accentué par la périodicité. Cependant, ces résultats doivent être comparés à ceux effectués par [Chamel, 2013] dans le cadre de la théorie des bandes, initialement développée pour les électrons dans les solides. Il trouve un comportement très différent, en présentant des neutrons fortement liés aux agrégats. Cette différence peut s'expliquer par l'applicabilité de chacune des approches effectuées. En effet, l'appariement des neutrons présent dans la croûte [Pines and Alpar, 1985] est négligé dans les calculs de [Chamel, 2013]. De plus dans le cadre de la physique des solides, le gap d'appariement des électrons est beaucoup plus petit que la différence d'énergie entre les bandes, alors qu'ici nous sommes dans une situation inversée. D'autre part, la théorie hydrodynamique est valide si l'appariement est fort, ce qu'on vérifie dans le gaz. Alors que dans les agrégats la densité est importante et peut engendrer un appariement faible, d'où une longueur de cohérence des paires de Cooper comparable à la taille des agrégats. De plus nous avons tous les deux négligés les effets de mouvements de point zéro [Pethick and Potekhin, 1998, Kobyakov and Pethick, 2013] qui peuvent réduire les effets de structure de bande, et affecter l'hydrodynamique car [Pethick and Potekhin, 1998] ont montré que la croûte aurait des propriétés élastiques proches des cristaux liquides.

La superfluidité dans la croûte interne impacte directement le mécanisme de *glitch* des pulsars[2]. Effectivement, les glitches sont compris comme un transfert soudain de moment cinétique du superfluide non ralenti (fluide non visqueux) vers la partie normale qui est ralentie par l'émission pulsar [Anderson and Itoh, 1975, Pines and Alpar, 1985]. Ainsi, la partie superfluide de l'étoile fait office de réservoir de moment cinétique pour le glitch. La taille du réservoir donne la proportion de neutrons superfluides qui composent la croûte, et contraint la masse maximal de l'étoile qui permet de comprendre les glitches fréquents de certains pulsars, comme présenté dans le Chapitre 9. Ici, nous trouvons des résultats très différents entre l'approche hydrodynamique et la théorie des bandes, ce qui implique des conclusions très éloignées quant à la masse des étoiles. Par exemple pour le pulsar Vela, nous trouvons une masse maximale de $\sim 1.7 M_\odot$, alors que la théorie des bandes prédit une masse maximale de $\sim 0.7 M_\odot$ [Chamel, 2013]. Comme discuté dans le paragraphe précédent, ces conclusions peuvent être impactées par la validité de l'hydrodynamique et de la théorie des bandes dans la croûte interne, mais aussi par la compréhension que nous avons des glitches, car comme le soulignent [Pines and Alpar, 1985, Andersson et al., 2012] ce modèle pour les glitches doit être amélioré.

D.5 Conclusion

Dans cette thèse, nous avons traité la croûte interne de façon assez large, en établissant les propriétés de chacun des éléments qui la composent. Puis

---

[2] Un glitch correspond à un saut dans la période des étoiles à neutrons en rotation et émettant un rayonnement par leurs pôles magnétiques (aussi appelées pulsars).

nous nous sommes penchés sur les impacts que cette description a au niveau astrophysique.

Cependant le travail n'est pas terminé, et il reste de nombreuses questions en suspens. Comme discuté, il serait intéressant d'effectuer la QRPA à température finie. Concernant la description des agrégats, un traitement HFB incluant la déformation et les effets de couches serait beaucoup plus précis. Quant à l'hydrodynamique et aux glitches, leur descriptions doivent être améliorées et consolidées pour pouvoir apporter des réponses plus précises à l'astrophysique. Pour terminer, notons que l'hydrodynamique sera un point de départ pour la caractérisation des phonons du réseau cristallin, qui contribuent eux aussi à la chaleur spécifique de l'étoile.

Bibliography

[Aguilera et al., 2009] Aguilera, D. N., Cirigliano, V., Pons, J. A., Reddy, S., and Sharma, R. (2009). Superfluid heat conduction and the cooling of magnetized neutron stars. *Physical Review Letters*, 102:091101.

[Anderson, 1958] Anderson, P. W. (1958). Random-phase approximation in the theory of superconductivity. *Physical Review*, 112:1900–1916.

[Anderson and Itoh, 1975] Anderson, P. W. and Itoh, N. (1975). Pulsar glitches and restlessness as a hard superfluidity phenomenon. *Nature*, 256:25–27.

[Andersson et al., 2012] Andersson, N., Glampedakis, K., Ho, W. C. G., and Espinoza, C. M. (2012). Pulsar glitches: The crust is not enough. *Physical Review Letters*, 109:241103.

[Arnett et al., 1989] Arnett, D., Bahcall, J., Kirshner, R., and Woosley, S. (1989). Supernova 1987A. *Annual Review of Astronomy and Astrophysics*, 27:629–700.

[Ashcroft and Mermin, 1976] Ashcroft, N. and Mermin, N. (1976). *Solid state physics*. Saunders College, Fort Worth.

[ATNF, 2016] ATNF (cited the April 26th, 2016). Australia Telescope National Facility pulsar catalogue. Website: `http://www.atnf.csiro.au/research/pulsar/psrcat/`.

[Avancini et al., 2010] Avancini, S. S., Chiacchiera, S., Menezes, D. P., and Providência, C. (2010). Warm “pasta” phase in the thomas-fermi approximation. *Physical Review C*, 82:055807.

[Avancini et al., 2008] Avancini, S. S., Menezes, D. P., Alloy, M. D., Marinelli, J. R., Moraes, M. M. W., and Providência, C. (2008). Warm and cold pasta phase in relativistic mean field theory. *Physical Review C*, 78:015802.

[Aymard et al., 2014] Aymard, F., Gulminelli, F., and Margueron, J. (2014). In-medium nuclear cluster energies within the extended thomas-fermi approach. *Physical Review C*, 89:065807.

[Baade and Zwicky, 1934] Baade, W. and Zwicky, F. (1934). Remarks on super-novae and cosmic rays. *Physical Review*, 46:76.

[Baldo et al., 2014] Baldo, M., Burgio, G., Centelles, M., Sharma, B., and Viñas, X. (2014). From the crust to the core of neutron stars on a microscopic basis. *Physics of Atomic Nuclei*, 77(9):1157–1165.

[Baldo and Ducoin, 2011] Baldo, M. and Ducoin, C. (2011). Elementary excitations in homogeneous superfluid neutron star matter: Role of the proton component. *Physical Review C*, 84:035806.

[Bardeen et al., 1957] Bardeen, J., Cooper, L. N., and Schrieffer, J. R. (1957). Theory of superconductivity. *Physical Review*, 108:1175–1204.

[Bethe and Wilson, 1985] Bethe, H. and Wilson, J. (1985). Revival of stalled supernova shock by neutrino heating. *The Astrophysical Journal*, 295:14.

[Bogner et al., 2007] Bogner, S., Furnstahl, R., Ramanan, S., and Schwenk, A. (2007). Low-momentum interactions with smooth cutoffs. *Nuclear Physics A*, 784:79.

[Bogoliubov et al., 1959] Bogoliubov, N., Tolmachev, V., and Shirkov, D. (1959). *A New Method in the Theory of Superconductivity*. Consultants Bureau, New York.

[Brack et al., 1985] Brack, M., Guet, C., and Håkansson, H.-B. (1985). Self-consistent semiclassical description of average nuclear properties a link between microscopic and macroscopic models. *Physics Reports*, 123(5):275 – 364.

[Cao et al., 2006] Cao, L. G., Lombardo, U., and Schuck, P. (2006). Screening effects in superfluid nuclear and neutron matter within brueckner theory. *Physical Review C*, 74:064301.

[Carter et al., 2005] Carter, B., Chamel, N., and Haensel, P. (2005). Entrainment coefficient and effective mass for conduction neutrons in neutron star crust: simple microscopic models. *Nuclear Physics A*, 748:675 – 697.

[Chabanat et al., 1997] Chabanat, E., Bonche, P., Haensel, P., Meyer, J., and Schaeffer, R. (1997). A skyrme parametrization from subnuclear to neutron star densities. *Nuclear Physics A*, 627(4):710 – 746.

[Chabanat et al., 1998] Chabanat, E., Bonche, P., Haensel, P., Meyer, J., and Schaeffer, R. (1998). A skyrme parametrization from subnuclear to neutron star densities. Part II. nuclei far from stabilities. *Nuclear Physics A*, 635:231 – 256.

[Chamel, 2006] Chamel, N. (2006). Effective mass of free neutrons in neutron star crust. *Nuclear Physics A*, 773(3–4):263–278.

[Chamel, 2012] Chamel, N. (2012). Neutron conduction in the inner crust of a neutron star in the framework of the band theory of solids. *Physical Review C*, 85:035801.

[Chamel, 2013] Chamel, N. (2013). Crustal entrainment and pulsar glitches. *Physical Review Letters*, 110:011101.

[Chamel and Carter, 2006] Chamel, N. and Carter, B. (2006). Effect of entrainment on stress and pulsar glitches in stratified neutron star crust. *Monthly Notices of the Royal Astronomical Society*, 368(2):796–808.

[Chamel et al., 2010] Chamel, N., Goriely, S., Pearson, J. M., and Onsi, M. (2010). Unified description of neutron superfluidity in the neutron-star crust with analogy to anisotropic multiband bcs superconductors. *Physical Review C*, 81:045804.

[Chamel and Haensel, 2008] Chamel, N. and Haensel, P. (2008). Physics of neutron star crusts. *Living Reviews in Relativity*, 11:10.

[Chamel et al., 2013a] Chamel, N., Page, D., and Reddy, S. (2013a). Low-energy collective excitations in the neutron star inner crust. *Physical Review C*, 87:035803.

[Chamel et al., 2013b] Chamel, N., Page, D., and Reddy, S. (2013b). Low-energy collective excitations in the neutron star inner crust. *Physical Review C*, 87:035803.

[Cirigliano et al., 2011] Cirigliano, V., Reddy, S., and Sharma, R. (2011). Low-energy theory for superfluid and solid matter and its application to the neutron star crust. *Physical Review C*, 84:045809.

[Combescot et al., 2006] Combescot, R., Kagan, M. Y., and Stringari, S. (2006). Collective mode of homogeneous superfluid fermi gases in the BEC-BCS crossover. *Physical Review A*, 74:042717.

[Craft Jr., 1970] Craft Jr., H. D. (September 1970). *Radio observations of the pulse profiles and dispersion measures of twelve pulsars*. PhD thesis, Cornell University.

[Dean and Hjorth-Jensen, 2003] Dean, D. J. and Hjorth-Jensen, M. (2003). Pairing in nuclear systems: from neutron stars to finite nuclei. *Reviews of Modern Physics*, 75:607.

[Debye, 1912] Debye, P. (1912). Zur theorie der spezifichen wärmen. *Annals of Physics (Leipzig)*, 39:789.

[Demorest et al., 2010] Demorest, P. B., Pennucci, T., Ransom, S. M., Roberts, M. S. E., and Hessels, J. W. T. (2010). A two-solar-mass neutron star measured using shapiro delay. *Nature*, 467:1081.

[Di Gallo et al., 2011] Di Gallo, L., Oertel, M., and Urban, M. (2011). Collective excitations in the neutron star inner crust. *Physical Review C*, 84:045801.

[Douchin and Haensel, 2000] Douchin, F. and Haensel, P. (2000). Inner edge of neutron-star crust with sly effective nucleon-nucleon interactions. *Physics Letters B*, 485:107 – 114.

[Douchin et al., 2000] Douchin, F., Haensel, P., and Meyer, J. (2000). Nuclear surface and curvature properties for SLy Skyrme forces and nuclei in the inner neutron-star crust. *Nuclear Physics A*, 665(3-4):419 – 446.

[Engel et al., 1975] Engel, Y., Brink, D., Goeke, K., Krieger, S., and Vautherin, D. (1975). Time-dependent hartree-fock theory with Skyrme's interaction. *Nuclear Physics A*, 249(2):215 – 238.

[Erler et al., 2013] Erler, J., Horowitz, C. J., Nazarewicz, W., Rafalski, M., and Reinhard, P.-G. (2013). Energy density functional for nuclei and neutron stars. *Physical Review C*, 87:044320.

[Evans and Okolie, 1982] Evans, D. and Okolie, S. (1982). The numerical solution of an elliptic P.D.E. with periodic boundary conditions in a rectangular region by the spectral resolution method. *Journal of Computational and Applied Mathematics*, 8(4):237 – 241.

[Fetter and Walecka, 1971] Fetter, A. and Walecka, J. (1971). *Quantum Theory of Many-particle Systems*. McGraw-Hill, New York.

[Foglizzo et al., 2015] Foglizzo, T., Kazeroni, R., Guilet, J., Masset, F., González, M., Krueger, B. K., Novak, J., Oertel, M., Margueron, J., Faure, J., Martin, N., Blottiau, P., Peres, B., and Durand, G. (2015). The explosion mechanism of core-collapse supernovae: Progress in supernova theory and experiments. *Publications of the Astronomical Society of Australia*, 32:e009 (17 pages).

[Forbes and Sharma, 2014] Forbes, M. M. and Sharma, R. (2014). Validating simple dynamical simulations of the unitary fermi gas. *Physical Review A*, 90:043638.

[Fortin et al., 2010] Fortin, M., Grill, F., Margueron, J., Page, D., and Sandulescu, N. (2010). Thermalization time and specific heat of the neutron stars crust. *Physical Review C*, 82:065804.

[Galassi et al., 2009] Galassi, M., Davies, J., Theiler, J., Gough, B., Jungman, G., Alken, P., Booth, M., and Rossi, F. (2009). *GNU Scientific Library Reference Manual - Third Edition (v1.12)*. Network Theory Limited, U.K. e-print: `https://www.gnu.org/software/gsl/manual/`.

[García-Recio et al., 1992] García-Recio, C., Navarro, J., Nguyen, V. G., and Salcedo, L. (1992). Response functions for infinite fermion systems with velocity dependent interactions. *Annals of Physics (N.Y.)*, 214(2):293 – 340.

[Gezerlis and Carlson, 2008] Gezerlis, A. and Carlson, J. (2008). Strongly paired fermions: Cold atoms and neutron matter. *Physical Review C*, 77:032801.

[Gezerlis and Carlson, 2010] Gezerlis, A. and Carlson, J. (2010). Low-density neutron matter. *Physical Review C*, 81:025803.

[Giacconi et al., 1962] Giacconi, R., Herbert, G., Paolini, F., and Rossi, B. (1962). Evidence for X Rays from sources outside the solar system. *Physical Review Letters*, 9(11).

[Glendenning, 1982] Glendenning, N. K. (1982). The hyperon composition of neutron stars. *Physics Letters B*, 114(6):392 – 396.

[Goldstone et al., 1962] Goldstone, J., Salam, A., and Weinberg, S. (1962). Broken symmetries. *Physical Review*, 127:965.

[Goriely et al., 2013] Goriely, S., Chamel, N., and Pearson, J. M. (2013). Further explorations of skyrme-hartree-fock-bogoliubov mass formulas. xiii.

the 2012 atomic mass evaluation and the symmetry coefficient. *Physical Review C*, 88:024308.

[Gor'kov and Melik-Barkhudarov, 1961] Gor'kov, L. P. and Melik-Barkhudarov, T. K. (1961). Contribution to the theory of superfluidity in an imperfect fermi gas. *Soviet Physics JETP*, 13(5):1018.

[Grasso et al., 2005] Grasso, M., Khan, E., and Urban, M. (2005). Temperature dependence and finite-size effects in collective modes of superfluid-trapped fermi gases. *Physical Review A*, 72:043617.

[Greenspan, 1964] Greenspan, D. (1964). On the numerical solution of problems allowing mixed boundary conditions. *Journal of the Franklin Institute*, 277(1):11 – 30.

[Hashimoto et al., 1984] Hashimoto, M.-a., Seki, H., and Yamada, M. (1984). Shape of nuclei in the crust of neutron star. *Progress of Theoretical Physics*, 71(2):320–326.

[Hebeler et al., 2007] Hebeler, K., Schwenk, A., and Friman, B. (2007). Dependence of the BCS $^1S_0$ superfluid pairing gap on nuclear interactions. *Physics Letters B*, 648:176 – 180.

[Hewish et al., 1968] Hewish, A., Bell, S., Pilkington, J., Scott, P., and Collins, R. (1968). Observation of a rapidly pulsating radio source. *Nature*, 217.

[Jackson, 1975] Jackson, J. D. (1975). *Classical Electrodynamics, Second Edition*. John Wiley & sons, New York.

[Keller and Sedrakian, 2013] Keller, J. and Sedrakian, A. (2013). Response functions of cold neutron matter: Density, spin, and current fluctuations. *Physical Review C*, 87:045804.

[Khan et al., 2005] Khan, E., Sandulescu, N., and Giai, N. V. (2005). Collective excitations in the inner crust of neutron stars: Supergiant resonances. *Physical Review C*, 71:042801(R).

[Khan et al., 2002] Khan, E., Sandulescu, N., Grasso, M., and Van Giai, N. (2002). Continuum quasiparticle random phase approximation and the time-dependent hartree-fock-bogoliubov approach. *Physical Review C*, 66:024309.

[Kirkwood, 1933] Kirkwood, J. G. (1933). Quantum statistics of almost classical assemblies. *Physical Review*, 44:31–37.

[Kobyakov and Pethick, 2013] Kobyakov, D. and Pethick, C. J. (2013). Dynamics of the inner crust of neutron stars: Hydrodynamics, elasticity, and collective modes. *Physical Review C*, 87:055803.

[Lassaut et al., 1987] Lassaut, M., Flocard, H., Bonche, P., Heenen, P., and Suraud, E. (1987). Equation of state of hot dense matter. *Astronomy and Astrophysics*, 198:L3–L6.

[Lattimer and Prakash, 2000] Lattimer, J. M. and Prakash, M. (2000). Nuclear matter and its role in supernovae, neutron stars and compact object binary mergers. *Physics Reports*, 333:121–146.

[Lattimer and Swesty, 1991] Lattimer, J. M. and Swesty, F. D. (1991). A generalized equation of state for hot, dense matter. *Nuclear Physics A*, 535(2):331 – 376.

[Lazarides and Van Schaeybroeck, 2008] Lazarides, A. and Van Schaeybroeck, B. (2008). Collective excitations of trapped imbalanced fermion gases. *Physical Review A*, 77:041602.

[Leggett, 1966] Leggett, A. (1966). Theory of a superfluid fermi liquid. ii. collective oscillations. *Physical Review*, 147:119–130.

[Lifshitz and Pitaevskii, 1980] Lifshitz, E. M. and Pitaevskii, L. P. (1980). *Statistical Physics, Part 2: Theory of the Condensed State*. Number 9 in Landau Lifshitz Course of Theoretical Physics. Pergamon, Oxford.

[Link et al., 1999] Link, B., Epstein, R. I., and Lattimer, J. M. (1999). Pulsar constraints on neutron star structure and equation of state. *Physical Review Letters*, 83:3362–3365.

[Lorenz et al., 1993] Lorenz, C. P., Ravenhall, D. G., and Pethick, C. J. (1993). Neutron star crusts. *Physical Review Letters*, 70:379–382.

[Magierski, 2004] Magierski, P. (2004). In-medium ion mass renormalization and lattice vibrations in the neutron star crust. *International Journal of Modern Physics E*, 13(1):371.

[Magierski and Bulgac, 2004a] Magierski, P. and Bulgac, A. (2004a). Nuclear hydrodynamics in the inner crust of neutron stars. *Acta Physica Polonica B*, 35:1203.

[Magierski and Bulgac, 2004b] Magierski, P. and Bulgac, A. (2004b). Nuclear structure and dynamics in the inner crust of neutron stars. *Nuclear Physics A*, 738:143–149.

[Margueron et al., 2003] Margueron, J., Vidaña, I., and Bombaci, I. (2003). Microscopic calculation of the neutrino mean free path inside hot neutron matter. *Physical Review C*, 68:055806.

[Martin and Urban, 2014] Martin, N. and Urban, M. (2014). Collective modes in a superfluid neutron gas within the quasiparticle random-phase approximation. *Physical Review C.*, 90:065805.

[Martin and Urban, 2015] Martin, N. and Urban, M. (2015). Liquid-gas coexistence vs. energy minimization with respect to the density profile in the inhomogeneous inner crust of neutron stars. *Physical Review C.*, 92:015803.

[Martin and Urban, 2016] Martin, N. and Urban, M. (2016). Superfluid hydrodynamics in the inner crust of neutron stars. *ArXiv e-prints*, 1606.01126.

[Maruyama et al., 2005] Maruyama, T., Tatsumi, T., Voskresensky, D. N., Tanigawa, T., and Chiba, S. (2005). Nuclear "pasta" structures and the charge screening effect. *Physical Review C*, 72:015802.

[Matsuo, 2006] Matsuo, M. (2006). Spatial structure of neutron cooper pair in low density uniform matter. *Phys. Rev. C*, 73:044309.

[Menotti et al., 2002] Menotti, C., Pedri, P., and Stringari, S. (2002). Expansion of an interacting fermi gas. *Physical Review Letters*, 89:250402.

[Migdal, 1959] Migdal, A. B. (1959). Superfluidity and the moments of inertia of nuclei. *Nucl. Phys.*, 13:655–674.

[Nambu, 1960] Nambu, Y. (1960). Quasi-particles and gauge invariance in the theory of superconductivity. *Physical Review*, 117:648.

[Napolitani et al., 2007] Napolitani, P., Chomaz, P., Gulminelli, F., and Hasnaoui, K. H. O. (2007). Ising analogue to compact-star matter. *Physics Review Letters*, 98:131102.

[Navarro et al., 1999] Navarro, J., Hernández, E. S., and Vautherin, D. (1999). Neutrino propagation and spin zero sound in hot neutron matter with skyrme interactions. *Physical Review C*, 60:045801.

[Negele and Vautherin, 1973] Negele, J. and Vautherin, D. (1973). Neutron star matter at sub-nuclear densities. *Nuclear Physics A*, 207(2):298 – 320.

[Nelder and Mead, 1965] Nelder, J. A. and Mead, R. (1965). A simplex method for function minimization. *The Computer Journal*, 7(4):308–313.

[Nozières, 1964] Nozières, P. (1964). *Theory of interacting Fermi systems*. Benjamin, New York.

[Oppenheimer and Volkoff, 1939] Oppenheimer, J. R. and Volkoff, G. M. (1939). On massive neutron cores. *Physical Review*, 55:374–381.

[Oyamatsu, 1993] Oyamatsu, K. (1993). Nuclear shapes in the inner crust of a neutron star. *Nuclear Physics A*, 561(3):431 – 452.

[Oyamatsu et al., 1984] Oyamatsu, K., Hashimoto, M.-a., and Yamada, M. (1984). Further study of the nuclear shape in high-density matter. *Progress of Theoretical Physics*, 72(2):373–375.

[Page and Reddy, 2012] Page, D. and Reddy, S. (2012). Thermal and transport properties of the neutron star inner crust. In Bertulani, C. and Piekarewicz, J., editors, *Neutron Star Crust*, chapter 14, pages 281–308. Nova Science Publishers, Hauppauge.

[Page and Reddy, 2013] Page, D. and Reddy, S. (2013). Forecasting neutron star temperatures: Predictability and variability. *Physical Review Letters*, 111:241102.

[Pais et al., 2015] Pais, H., Chiacchiera, S., and Providência, C. (2015). Light clusters, pasta phases, and phase transitions in core-collapse supernova matter. *Physical Review C*, 91:055801.

[Pais et al., 2014] Pais, H., Newton, W. G., and Stone, J. R. (2014). Phase transitions in core-collapse supernova matter at sub-saturation densities. *Physical Review C*, 90:065802.

[Papakonstantinou et al., 2013] Papakonstantinou, P., Margueron, J., Gulminelli, F., and Raduta, A. R. (2013). Densities and energies of nuclei in dilute matter at zero temperature. *Physical Review C*, 88:045805.

[Pastore et al., 2012] Pastore, A., Martini, M., Buridon, V., Davesne, D., Bennaceur, K., and Meyer, J. (2012). Nuclear response for the skyrme effective interaction with zero-range tensor terms. iii. neutron matter and neutrino propagation. *Physical Review C*, 86:044308.

[Pearson et al., 2014] Pearson, J., Chamel, N., Fantina, A., and Goriely, S. (2014). Symmetry energy: nuclear masses and neutron stars. *European Physical Journal A*, 50(2).

[Pearson et al., 2012] Pearson, J. M., Chamel, N., Goriely, S., and Ducoin, C. (2012). Inner crust of neutron stars with mass-fitted skyrme functionals. *Physical Review C*, 85:065803.

[Pethick and Potekhin, 1998] Pethick, C. and Potekhin, A. (1998). Liquid crystals in the mantles of neutron stars. *Physics Letters B*, 427:7–12.

[Pethick et al., 2010] Pethick, C. J., Chamel, N., and Reddy, S. (2010). Superfluid dynamics in neutron star crusts. *Progress of Theoretical Physics Supplement*, 186:9–16.

[Piekarewicz and Sánchez, 2012] Piekarewicz, J. and Sánchez, G. T. (2012). Proton fraction in the inner neutron-star crust. *Physical Review C*, 85:015807.

[Pines and Alpar, 1985] Pines, D. and Alpar, M. A. (1985). Superfluidity in neutron stars. *Nature*, 316:27–32.

[Rajagopal, 1978] Rajagopal, A. K. (1978). Inhomogeneous relativistic electron gas. *Journal of Physics C*, 11.

[Ramanan and Urban, 2013] Ramanan, S. and Urban, M. (2013). Bec-bcs crossover in neutron matter with renormalization-group-based effective interactions. *Physical Review C*, 88:054315.

[Ravenhall et al., 1983] Ravenhall, D. G., Pethick, C. J., and Wilson, J. R. (1983). Structure of matter below nuclear saturation density. *Physical Review Letters*, 50:2066–2069.

[Riles, 2013] Riles, K. (2013). Gravitational waves: Sources, detectors and searches. *Progress in Particle and Nuclear Physics*, 68:1–54.

[Ring and Schuck, 1980] Ring, P. and Schuck, P. (1980). *The Nuclear Many-Body Problem*. Springer, Berlin.

[Rowe, 1970] Rowe, D. J. (1970). *Nuclear Collective Motion. Models and Theory*. Methuen, London.

[Salpeter, 1961] Salpeter, E. (1961). Energy and pressure of a zero-temperature plasma. *Astrophysical Journal*, 134:669.

[Sebille et al., 2011] Sebille, F., de la Mota, V., and Figerou, S. (2011). Probing the microscopic nuclear matter self-organization processes in the neutron star crust. *Physical Review C*, 84:055801.

[Sedrakian, 1996] Sedrakian, A. (1996). Neutron-phonon interaction in neutron stars: phonon spectrum of coulomb lattice. *Astrophysics and Space Science*, 236:267–276.

[Sedrakian and Keller, 2010] Sedrakian, A. and Keller, J. (2010). Response functions of cold neutron matter: Density fluctuations. *Physical Review C*, 81:045806.

[Shapiro and Teukolsky, 2004] Shapiro, S. L. and Teukolsky, S. A. (2004). *Black Holes, White Dwarfs and Neutron Stars: The Physics of Compact Objects*. Wiley-VCH Verlag, Weinheim.

[Sun et al., 2010] Sun, B. Y. S., Toki, H., and Meng, J. (2010). Relativistic description of bcs–bec crossover in nuclear matter. *Phys. Lett. B*, 683(2-3):134–139.

[Tamagaki, 1970] Tamagaki, R. (1970). Superfluid state in neutron star matter. *Progress of Theoretical Physics*, 44:905.

[Tinkham, 1975] Tinkham, M. (1975). *Introduction to Superconductivity*. McGraw-Hill, New York.

[Tolman, 1939] Tolman, R. C. (1939). Static solutions of Einstein's field equations for spheres of fluid. *Physical Review*, 55:364–373.

[Tonini et al., 2006] Tonini, G., Werner, F., and Castin, Y. (2006). Formation of a vortex lattice in a rotating bcs fermi gas. *European Physical Journal D*, 39:283.

[Urban and Oertel, 2015] Urban, M. and Oertel, M. (2015). Collective modes in the superfluid inner crust of neutron stars. *International Journal of Modern Physics E*, 24:1541006.

[Urban and Schuck, 2006] Urban, M. and Schuck, P. (2006). Dynamics of a trapped fermi gas in the bcs phase. *Physical Review A.*, 73:013621.

[Vautherin and Brink, 1972] Vautherin, D. and Brink, D. M. (1972). Hartree-fock calculations with skyrme's interaction. i. spherical nuclei. *Physical Review C*, 5:626–647.

[Watanabe et al., 2003] Watanabe, G., Sato, K., Yasuoka, K., and Ebisuzaki, T. (2003). Structure of cold nuclear matter at subnuclear densities by quantum molecular dynamics. *Physical Review C*, 68:035806.

[Weinberg, 2005] Weinberg, S. (2005). *The Quantum Theory of Fields: Volume 2, Modern Applications*. Quantum Theory of Fields. Cambridge University Press, Cambridge.

[Wigner, 1932] Wigner, E. (1932). On the quantum correction for thermodynamic equilibrium. *Physical Review*, 40:749–759.

[Wlazłowski et al., 2016] Wlazłowski, G., Sekizawa, K., Magierski, P., Bulgac, A., and McNeil Forbes, M. (2016). Vortex pinning and dynamics in the neutron star crust. *ArXiv e-prints*, 1606.04847.

[Yakovlev et al., 2001] Yakovlev, D., Kaminker, A., Gnedin, O., and Haensel, P. (2001). Neutrino emission from neutron stars. *Physics Reports*, 354:1–155.

université PARIS-SACLAY
ÉCOLE DOCTORALE PHENIICS

Title Collective modes and hydrodynamics the inner crust of neutron stars.

Keywords neutron star, crust, collective modes, hydrodynamics, nuclear physics.

Abstract Neutron stars have been extensively studied since Baade and Zwicky have proposed their existence in 1934. Their description is at the interface of numerous domains of physics, e.g., X-ray astrophysics, pulsar signal observation, general relativity and nowadays gravitational waves, solid state physics, and also nuclear physics.

In this thesis we will concentrate on the nuclear physics description, especially of the inner crust. These stars are charaterized by their large mass from one to two solar masses, in a radius of ~ 10 km. Their inner structure can be divded in three major layers: the *outer crust*, the *inner crust* and the *core*. The outer crust consists of nuclei coexisting with an electron gas to ensure charge neutrality. If one goes deeper into the crust, the ratio of neutrons with respect to the total nucleon number increases. Eventually, the excess of neutrons in the nuclei gets so high that they drip out from the nuclei and create a dilute neutron gas. From now on, we will speak of *nuclear clusters* instead of nuclei. This phenomenon defines the limit between the outer crust and the inner crust. This complicated structure and composition is at the origin of many characteristic properties of neutron stars.

Hence, we will construct our work in three major parts. First, we start to account for the neutron gas surrounding the clusters, which we treat as uniform. Here, the neutron gas is assumed to be superfluid, and one can expect a Goldstone mode. This description will be done in the framework of QRPA. Second, we will focus on the study of properties of the clusters contained in the inner crust. Under these conditions we expect to see cystal of spheres, *rods* and *plates* of bound nucleons, that we will describe with the help of the ETF approximation. Third, we will finish by treating the interaction between the clusters and the gas with hydrodynamics. The results will be applied to astrophysics and in particular to glitches.

Titre Modes collectifs et hydrodynamique dans la croûte interne des étoiles à neutrons.

Mots clés étoile à neutrons, croûte, modes collectifs, hydrodynamique, physique nucléaire.

Résumé Les étoiles à neutrons ont été largement étudiées depuis que Baade and Zwicky ont postulé leur existence en 1934. Ces études ont été et sont réalisées à l'interface de différents domaines la physique tels que : l'astrophysique en rayons X, l'observation des pulsars, la relativité générale et plus dernièrement les ondes gravitationnelles, la physique du solide, ainsi que la physique nucléaire.

Dans cette thèse nous nous concentrerons sur la description des étoiles à neutrons dans le cadre de la physique nucléaire et précisément de la croûte interne de l'étoile. Ces étoiles sont caractérisées par une masse importante de l'ordre d'une à deux masses solaires dans un rayon de ~ 10 km. Quant à leur structure interne elle peut être décrite en trois strates : la *croûte externe*, la *croûte interne* et le *cœur*. La croûte externe correspond à un réseau cristallin de noyaux atomiques et un gaz d'électrons relativistes. Vient ensuite la croûte interne, définie lorsque les noyaux de la croûte externe sont si riches en neutrons qu'ils les libèrent dans le milieu pour former un gaz. Ici, nous ne parlons plus de noyaux mais d'*agrégats* car tous les nucléons qui les composent ne sont plus systématiquement liés. Cette structure complexe et sa composition est à l'origine de nombreuses propriétés caractéristiques des étoiles à neutrons.

C'est ainsi que nous construirons notre étude en trois parties. Tout d'abord nous commencerons par traiter le gaz de neutrons entourant les agrégats. Le gaz de neutrons que nous considérons uniforme ici est superfluide et devrait donc présenter un mode de Goldstone. Cette description sera effectuée à l'aide de la QRPA. Puis nous en viendrons à la description des agrégats. Dans ces conditions on s'attend à observer des cristaux de sphères, des *cylindres* et des *plaques* de matière nucléaire, que nous décrirons grâce à l'approximation ETF. Puis nous terminerons par la description de l'interaction entre les agrégats et le gaz au niveau dynamique, et ce dans le cadre de la théorie hydrodynamique. Ces résultats seront appliqués à l'astrophysique et en particuliers aux glitches.